UNIVERSITÀ
DEGLI STUDI
FIRENZE

DOTTORATO DI RICERCA IN FISICA E ASTRONOMIA

CICLO XXXI

COORDINATORE Prof. D'Alessandro Raffaello

CARATTERIZZAZIONE SPETTROSCOPICA DI NANOMATERIALI

Settore Scientifico Disciplinare FIS/03

Dottorando
Dott. Cini Alberto

Cini Alberto

Tutore
Dott. ssa Fittipaldi Maria

Maria Fittipaldi

Coordinatore
Prof. D'Alessandro Raffaello

Raffaello D'Alessandro

Anni 2015/2018

Contents

Introduction

Nanomaterials represent promising objects both for the study of fundamental science and for new interesting applications in many technological fields. The interest in these materials is driven by the fact that approaching nanometer dimensions peculiar and different electrical, optical and magnetic properties with respect to those observed in the bulk phase can be observed, as the emergence of quantum effects. Furthermore, another common feature of nanomaterials is the presence of a very high fraction of their atoms on their surfaces, that can again be responsible for changes in the properties of the material with respect to bulk [1].

The nanomaterials studied in this thesis are principally magnetic. Ideally, starting from a bulk ferromagnet and reducing its volume and therefore the number of magnetic moments included in the material, first the magnetic nanoparticles (MNPs) are encountered and finally the molecular nanomagnets (MNMs) [2]. MNPs are obtained from the bulk by a top-down approach, while MNMs are synthesized by means of a bottom-up approach, starting from the single atoms [3]. Theoretically, the MNPs are still described classically, while the features of MNMs are interpreted using quantum mechanics. In the class of MNMs two objects can be distinguished: single molecule magnets (SMMs) and single chain magnets (SCMs). MNPs are proposed for many technological applications [4, 5, 6], while SMMs have potential applications for high-density information storage, spintronics [7, 8, 9] and quantum computing [10, 11, 12].

Another type of nanomaterial studied and reported in this thesis is a spin crossover (SCO) complex, i.e. a bistable molecule that can switch between two different spin states by means of external stimuli, as temperature, pressure and light irradiation with appropriate wavelength. For this reason SCO molecules have been proposed as sensors [13, 14], as well as for spintronics [7, 15].

In order to characterize these nanomaterials in view of their proposed applications, two different spectroscopic techniques have been used: Mössbauer spectroscopy and electron paramagnetic resonance (EPR) spectroscopy. Mössbauer spectroscopy relies on the resonant absorption and emission of gamma rays by nuclei in a solid and, by evidencing the hyperfine interactions of the probed nucleus, it allows to investigate its structural, chemical, electronic and magnetic properties. EPR is based on the absorption of electromagnetic radiation in the microwave range by a paramagnetic system subjected to an external magnetic field. The structural and electronic properties characterizing the probed atom, as well as information on the dynamical properties involving

it, can be obtained.

This thesis faces some of the open problems regarding some of the cited nanomaterials. To this aim state-of-the-art configurations of the aforementioned spectroscopic techniques were used.

SMMs have been widely characterized in the bulk phase by various techniques, as magnetometry, Mössbauer spectroscopy and EPR. The use of these molecules for the proposed applications relies on the persistence of their properties once they are deposited on a solid surface. However, none of the cited techniques has the proper sensitivity to study a thin layer of SMMs grafted on a solid surface. For this reason we considered the Synchrotron Mössbauer Source (SMS), that, by means of an appropriate filtering of synchrotron light, produces a ^{57}Fe-resonant narrow single line with high intensity and spatial resolution. By taking advantage of SMS, energy-domain Mössbauer spectra of a monolayer of molecular material were realized for the first time. Significant deformations of the magnetic core of the molecules induced by the interaction with the substrate were detected. However these modifications did not alter the overall magnetic structure of the system and therefore its SMM behavior resulted to be retained after deposition.

Thanks to its sensitivity synchrotron Mössbauer spectroscopy based on SMS was used also to study a SCO molecule deposited on a surface. The SCO transition is known to be a collective phenomenon and the evaluation of the effect of the substrate on the SCO efficiency of the molecules is necessary prior to their use for the proposed devices. The analysis of the energy-domain Mössbauer spectra of the investigated samples allowed to reveal a reduction in the SCO efficiency of the molecules with respect to molecules in the bulk phase.

SCMs are proposed for memory storage and quantum information technology. For this last purpose a promising class of SCMs are those that lack an inversion center, because they can show magnetoelectric effects. Their addressing through an electric field rather than with a magnetic one is preferred, since a faster, less energy demanding and more space-confined inspection can be realized. For this reason we implemented a standard EPR spectrometer with the possibility to apply an oscillating electric field on the sample while revealing the EPR absorption. Thanks to this setup signals associated with a magnetoelectric coupling between the single crystal of a molecular helix and the electric field were detected.

MNPs are approaching the size of MNMs, therefore a common (quantum) description for these two systems seems necessary [16]. Moreover, evidences of the quantum behavior of MNPs have already been found [17, 18, 19, 20]. Here we acquired EPR spectra of MNPs in two different configurations, the standard one, with the microwave magnetic field perpendicular to the external magnetic field, and the parallel one, with the microwave magnetic field parallel to the external magnetic field, in order to sense the effect of different selection rules and eventually evidence the quantum nature of the system. Successively the EPR spectra were interpreted by means of an approach based on the giant spin model.

In Chapter 1, the principal features of the nanomaterials studied in this thesis are presented: first the magnetic nanomaterials are introduced, then the SCO complex is

described. In Chapter 2, the theoretical and technical aspects related to the two used investigative tools (Mössbauer and EPR spectroscopy) are reported. In Chapter 3, the study of a monolayer of SMMs deposited on gold by means of synchrotron Mössbauer spectroscopy is presented. Chapter 4 reports the use of synchrotron Mössbauer spectroscopy to investigate a SCO molecule deposited on gold. In Chapter 5, the investigation of the magnetoelectric effects in a molecular helix by means of the implementation in a standard EPR spectrometer of the electric field acting on the sample is reported. In Chapter 6, the study of the quantum nature of MNPs by means of EPR spectroscopy and the simulation of the corresponding spectra is described. Finally, in Chapter 7, the conclusions of these studies are summarized.

Chapter 1

Nanomaterials

The actual interest in nanomaterials is motivated by the fact that, passing to nanometer dimensions, the materials can show peculiar and different properties with respect to those associated to the bulk phase [1]. One the most interesting properties is the emergence of quantum effects. These properties can be at the base of innovative applications. This chapter introduces the principal features of the nanomaterials studied in this thesis. First, the different kinds of magnetic nanomaterials are reported. Finally, a spin crossover complex is described.

1.1 Magnetic nanomaterials

Magnetic materials can be classified by the number of magnetic moments that they contain in their volume, that roughly corresponds to the number of atoms inside the magnetic system [2]. Passing from macroscopic to nanoscopic sizes different behaviors can be recognized, which are responsible for the different properties of the materials. A classification of the nanomaterials studied in this thesis is depicted in Fig. 1.1.

A permanent magnet has a number of magnetic moments in its macroscopic volume of the order of 10^{20} and is characterized by a multi-domain structure, which is responsible for the presence of a hysteresis loop. Magnetic nanoparticles contain less than 10^8 magnetic moments and they can be derived from bulk by a top-down approach; moreover, depending on the material and their dimensions, they can behave like single-domain particles. Finally, molecular nanomagnets are nanometer sized objects, the magnetic properties of which are determined by the single molecule. They are synthesized by means of a bottom-up approach. Two classes of important molecular nanomagnets are single molecule magnets and single chain magnets. Quantum phenomena, as quantum tunnelling of the magnetization between the energy levels, have been reported in single molecule magnets.

The bottom-up approach followed for the synthesis of molecular nanomagnets allows to understand the properties of systems starting from the single molecule to clusters comprising many spin centers. Moreover, it enables to follow the evolution of the

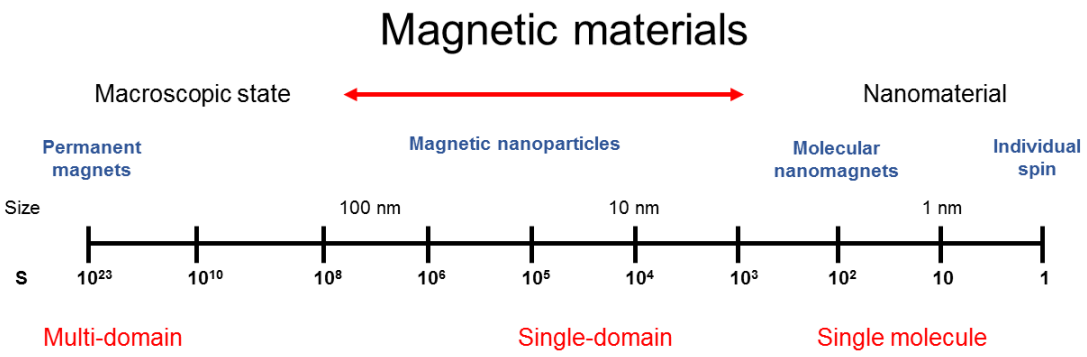

Figure 1.1: Classification of magnetic nanomaterials according to the number of magnetic moments (S), that they contain.

features of the system from nanoscopic to macroscopic dimensions.

One of the fundamental interactions in magnetic materials is the exchange one, which is also a fundamental parameter in the design of molecular nanomagnets.

As an example of how the exchange interaction contributes to the structuring of the energy levels of molecular nanomagnets, a ring system can be considered [16]. It has been shown that the energies of the low lying levels of rings of N ions (N being an even integer) of spin s can be expressed by partitioning the spins in two sets [21, 22, 23, 24] (for the N odd case spin frustration effects can be encountered for antiferromagnetic interactions, which make the treatment more complex). The exchange Hamiltonian, responsible of the isotropic splitting of the $(2s+1)^N$ states, is [16]

$$H_{exc} = \sum_i J \mathbf{s}_i \cdot \mathbf{s}_{i+1} \tag{1.1}$$

For N even the $N/2$ spins which occupy odd sites are coupled together to give an intermediate spin S_1, while the analogous treatment of the even site spins gives S_2. If no next nearest neighbours interaction is present, the S_1 and S_2 states are degenerate. Switching on the exchange interaction (Eq. 1.1) the energies of the $|S_1 S_2 S>$ states are given by [16]

$$E\left(S_1 S_2 S\right) = \frac{J\left(S_1 S_2 S\right)}{2}\left[S\left(S+1\right) - S_1\left(S_1+1\right) - S_2\left(S_2+1\right)\right] \tag{1.2}$$

where $J\left(S_A S_B S\right)$ is an effective coupling constant associated with the true nearest neighbour coupling constant J by the following relation, valid for $S_A = S_B = \left(N/2\right)s$ [16]

$$J\left(S_A S_B S\right) = \left(4/N\right) J \tag{1.3}$$

For ferromagnetic coupling the lowest lying states, which correspond to having all the individual spins parallel, are shown by the graph of Fig. 1.2a, where the energies

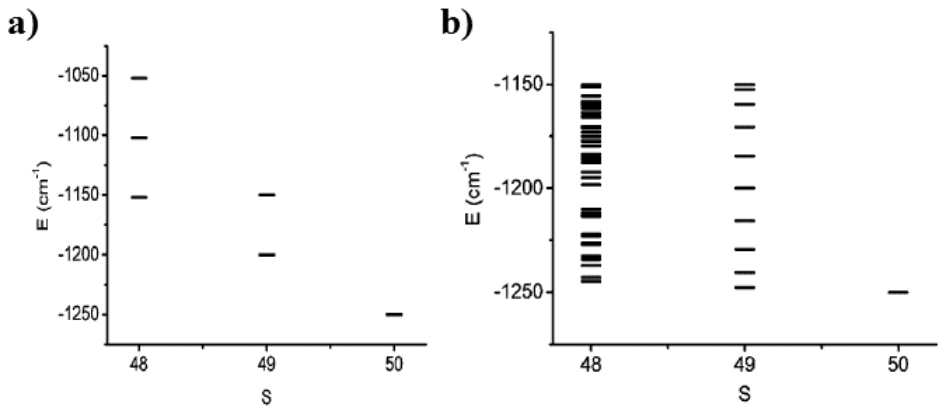

Figure 1.2: Calculated energy levels for a ring of $N = 20$ spins and $s = 5/2$ using Eq. 1.2 and 1.3 (a) and using a full matrix diagonalization, where only states with total $S \geq Ns - 2$ are considered (b). The value of J is 10 cm^{-1}. Image taken from [16].

of the states corresponding to $|(N/2)s\ (N/2)s\ S>$, $|(N/2)s\ (N/2)s-1\ S-1>$ and $|(N/2)s-1\ (N/2)s-1\ S-2>$ for $N = 20$ and $s = 5/2$ are plotted. The energies are calculated using Eq. 1.2 and 1.3 [16].

Alternatively, although the full matrix diagonalization for $N = 20$ is impossible, given the dimension of the Hilbert space corresponding to $6^{20} \times 6^{20}$, the low lying states can be calculated by classifying the functions for their total spin S [16]. For ferromagnetic coupling there is only one function with $S = Ns$ and also the matrices corresponding to $S = Ns - 1$, $S = Ns - 2$, etc. have comparatively small size. The energies calculated with the diagonalization of the Hamiltonian matrix for the $N = 20$ ring for $S = Ns$, $Ns - 1$ and $Ns - 2$ only are shown in Fig. 1.2b. The main difference between the two schemes is that the energies calculated with Eq. 1.2 and 1.3 are more quantized than those obtained by diagonalization, because the simplified scheme does not allow for admixing of states with the same S. In particular, the gap between the ground $S = Ns$ and the first excited $S = Ns - 1$ state goes to zero on increasing N, as expected since the levels must merge in a continuum for large N [16]. This example on the ring system shows how the molecular approach allows to pass from local to collective parameters and therefore understand the properties of complex systems.

Finally, it is worth noting that the key feature that determines the peculiar magnetic behavior of magnetic nanoparticles and molecular nanomagnets is magnetic anisotropy. Magnetic anisotropy is defined as the tendency of the magnetization to align along certain crystallographic axes, that are called easy axes [25]. This translates into a difference in the magnetic properties of the material depending on the different directions. The magnetic anisotropy arises from several contributions [26]: single ion anisotropy, which depends on the geometry of the individual ions; dipolar anisotropy, arising from the interaction between the magnetic moments of the ions; shape anisotropy. For molecular nanomagnets, if the coupling scheme is known, the magnetocrystalline anisotropy

can be calculated by summing each individual single ion contribution weighted for a coefficient which is obtained by projecting the local spin s on the total spin S [16] (the calculation of magnetic anisotropy for a model molecular nanomagnet is reported in Section 2.2.3). On the other hand, since for magnetic nanoparticles the contribution of each individual ion cannot be determined, single ion anisotropy is subdivided in two different classes [26]: magnetocrystalline anisotropy, which refers to the anisotropy of the core of the nanoparticle and is considered equal to the anisotropy of the corresponding bulk material; surface anisotropy, arising from the low symmetry and coordination of the surface ions, which are particularly numerous in ultrasmall magnetic nanoparticles. Moreover, the shape anisotropy originates from the magnetostatic energy, which makes the sample more easily magnetized in the direction of its largest dimension [26]. Finally, it is worth noting that in molecular nanomagnets the shape of the molecule itself plays a role. Through-space dipolar interactions between the magnetic centers of the molecule are known to provide a sizeable contribution to the magnetic anisotropy of the molecules and are generally considered as additive terms to the magnetocrystalline component [3]. Contrary to single ion terms, they do not depend on the first coordination sphere, but rather on the spatial arrangement and therefore on the shape of the molecule [16]. However, the dipolar contribution to the magnetic anisotropy is not unequivocally determined by the shape of the molecule, but it is related to the ferromagnetic or antiferromagnetic nature of the exchange interaction between the spins.

1.1.1 Bulk ferromagnet

A ferromagnet is a material that, thanks to a long range order of the magnetic moments inside it, may exhibit a spontaneous magnetization also in the absence of an applied magnetic field. When a magnetic field is applied, the magnetization can vary between zero and a saturation value.

This behavior of the magnetization is explained by the presence of magnetic domains, that are defined as regions in space within which all the individual magnetic moments are parallel (antiparallel) to each other. The origin of the domains relies on the possibility to minimize the magnetostatic energy of the system. The orientation of the moments inside each domain varies from domain to domain and is responsible for the spontaneous magnetization of the sample. The transition from a domain to the neighboring one occurs through a region where the local magnetic moments are rapidly varying, called domain wall or Bloch wall [25]. The width of the domain walls δ depends on the exchange energy A and the magnetic anisotropy constant K according to the relation [2]

$$\delta = \sqrt{A/K} \tag{1.4}$$

The relation shows that, while A tends to keep the spins ordered and to make the walls as large as possible, K tends to minimize the domain walls. The width and the shape of the domain walls depend on the material. For the most common materials the dimensions of the domain walls are of the order of 10 - 100 nm.

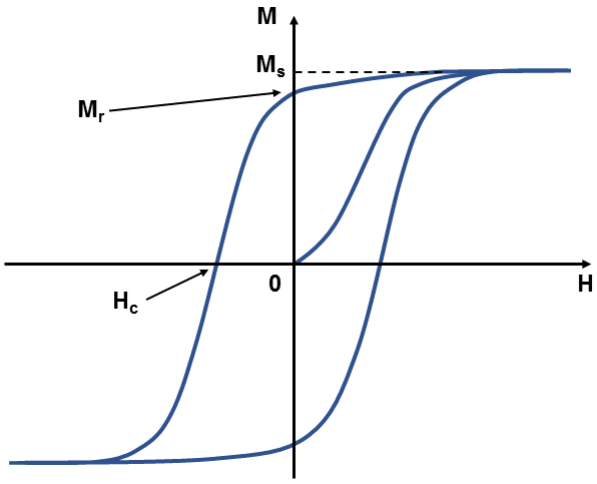

Figure 1.3: Hysteresis loop of a bulk ferromagnet. The saturation magnetization (M_s), the remnant magnetization (M_r) and the coercive field (H_c) are indicated.

The application of an external magnetic field makes all the individual moments parallel to each other and therefore the magnetization reaches its saturation value (M_s). Decreasing the field, the formation of domains is not reversible in such a way that the magnetization at zero field will not be zero, as in the non-magnetized case. The finite value of the magnetization in zero field is called the remnant magnetization (M_r). In order to demagnetize the sample, it is necessary to apply a negative field, which is called the coercive field (H_c). This features result into a hysteresis loop (see Fig. 1.3), meaning that the value of the magnetization of the sample depends on its history. This is the basis of the use of magnets for storing information [3].

1.1.2 Magnetic nanoparticles

The first nanomaterials that are encountered by passing from a bulk magnetic material to nanometer dimensions are magnetic nanoparticles. These objects contain less than 10^8 magnetic moments in their volume and their synthesis usually follows a top-down approach, where the parameters characterizing the nanoparticles are derived and compared with those of the bulk [16]. When the diameter of the nanoparticle is lower than the value of the width of the domain wall δ in the material, the formation of domains is not energetically favored anymore and the particle is said to be single-domain. This means that all the constituent spins move simultaneously and behave as a giant spin.

If the anisotropy of the magnetization is of the Ising type (i.e. the stable orientation of the magnetic moment of the particle is parallel to a given direction z), the energy of the system as a function of the orientation of the magnetic moment is a double well, with the two wells corresponding to magnetization up and magnetization down, respectively (see Fig. 1.4). The barrier for the reorientation of the magnetization is [26]

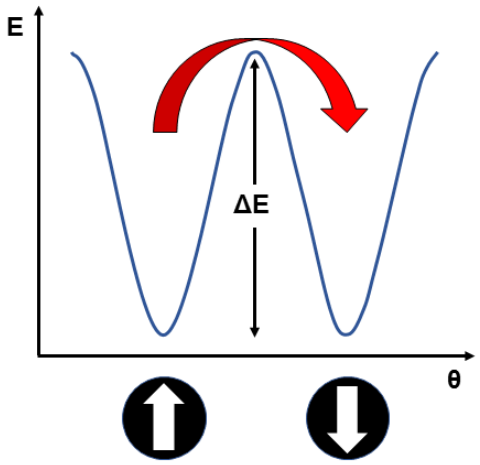

Figure 1.4: Energy of a magnetic nanoparticle as a function of the angle between its magnetization and the z axis.

$$\Delta E = KV \tag{1.5}$$

where K is the anisotropy energy density and V is the volume of the particle.

At low temperature ($\Delta E > k_B T$), the magnetization of the particle is blocked, while at high temperature the magnetization fluctuates as in a paramagnet. However, considering that all the spins respond to the external perturbation, the particle behaves as a superparamagnet. The characteristic time for the reorientation of the magnetization follows an Arrhenius law [3]

$$\tau = \tau_0 exp\,(\Delta E / k_B T) \tag{1.6}$$

where τ_0 is the relaxation time at infinite temperature. Typical values of τ_0 are 10^{-9} - 10^{-11} s [16].

It is worth noting that for a superparamagnet the observation of either static or dynamic magnetic behavior depends on the time scale of the experiment used to investigate it. The so-called blocking temperature is the temperature at which the relaxation time of the magnetization equals the characteristic time of the experimental technique.

Depending on the nature of the material, the size of the particles needed to observe superparamagnetic behavior ranges from 2 - 3 to 20 - 30 nm [3]. The magnetic properties of particles larger than 10 nm (corresponding to more than 10^5 iron ions) are usually interpreted using a top-down approach [26]. On the other hand, for the investigation of particles in the range of 1 - 5 nm, comprising 10 - 10^4 ions, a molecular bottom-up approach may be more useful [26], extrapolating the parameters of the nanoparticles from the values of the individual spin centers. This size range is also particularly promising for observing new properties associated with the coexistence of classical and

quantum behaviors, as the quantum tunneling of the magnetization, i.e. the possibility to invert the magnetization through the quantum tunnel effect [26]. This feature has been already demonstrated in molecular nanomagnets, which are characterized by a bottom-up approach and described by quantum mechanics starting from the single ion. Magnetic nanoparticles and molecular nanomagnets are approaching similar size with a comparable number of metal ions, of the order of 10^2. This observation poses the need for a unified description of the two systems [16].

In order to unequivocally observe quantum phenomena, a collection of identical objects is needed. While the molecular basis of molecular nanomagnets ensures that we are dealing with an ensemble of identical objects, this is more difficult to achieve in magnetic nanoparticles. However significant improvements in the synthesis of the magnetic nanoparticles have been made in recent years [3]. An original procedure for the synthesis of magnetic nanoparticles uses the ferritin protein, which acts as a nanocage. In this way particles with nanometer (< 10 nm) dimensions and containing thousands of iron ions can be synthesized.

It is worth noting that a core-shell model has been proposed in order to interpret the dependence of the magnetic properties of the magnetic nanoparticles on their size [26]. In particular, the structure of the magnetic nanoparticles is suggested to be constituted by a core, where the arrangement of the Fe ions is essentially that of the bulk, and a magnetically disordered external layer, having a constant thickness of 1 nm, independent of the particle size, in which the number and symmetry of the Fe ions is different from that of the core ones. Simulations based on this core-shell model indicate that for example for maghemite nanoparticles having a diameter of 2.5 nm 95 % of the Fe ions belongs to the external shell, while only 17 Fe ions to the core [27]. This observation points again to the need of a common view of magnetic nanoparticles and molecular nanomagnets, suggesting the study of large iron clusters, such as Fe_{19}, a molecular cluster comprising 19 Fe(III) ions bridged by oxo-hydroxide ions, as model systems between the two objects [28].

Beyond being interesting for fundamental science [16, 2], magnetic nanoparticles are proposed for many technological applications [6], as catalysis [29], data storage [4], spintronics [5], magnetic resonance imaging [30, 31], magnetic fluids [32], biotechnology and biomedicine [33, 34] and environmental remediation [35, 36].

1.1.3 Molecular nanomagnets

The term molecular nanomagnet defines a class of molecules containing magnetically interacting metallic ions which are synthesized in a bottom-up approach, i.e. by adding an increasing number of magnetic centers. These molecules are usually arranged in crystalline-ordered structures in which shells of organic ligands provide magnetic separation between adjacent molecules. The crystals are constituted of very weakly interacting molecules, so that the magnetic properties of the system are determined by the single molecule. In molecular nanomagnets the molecules are arranged like rings and clusters to form zero-dimensional (0D) objects, the so-called single molecule magnets,

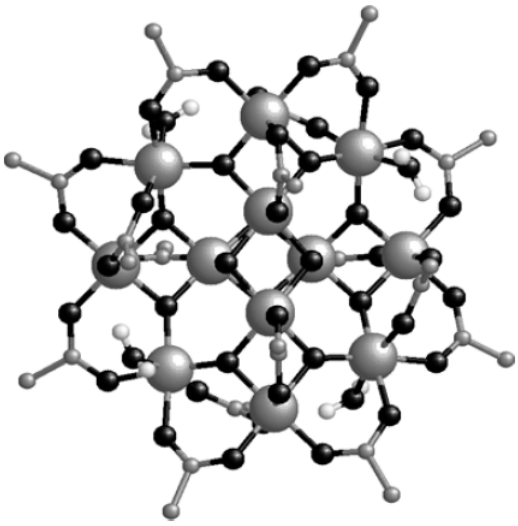

Figure 1.5: Structure of the Mn12ac SMM along the tetragonal axis. The Mn ions are reported as large grey spheres, while O, C and H are reported as small black, grey and white spheres, respectively. Only H atoms of water molecules have been drawn for sake of clarity. Image taken from [3].

and chains, that give rise to one-dimensional (1D) structures, the so-called single chain magnets.

1.1.3.1 Single molecule magnets

Single molecule magnets (SMMs) are molecules that exhibit slow relation of the magnetization at low temperature of purely molecular origin, i.e. implying no long range order. These molecules are model systems to investigate magnetism at the nanoscale, as well as the emergence of quantum effects.

SMMs are polynuclear coordination compounds of paramagnetic metal ions. They consist of an inner magnetic core surrounded by a shell of organic ligands, which often provide an effective shielding between adjacent molecules in the solid state. SMMs come in a variety of shapes and sizes and allow selective substitutions of the ligands to alter the coupling to the environment. Moreover, it is possible to exchange the magnetic ions, thus changing the magnetic properties without modifying the structure or coupling. The first observation of a magnetic hysteresis of molecular origin and coexistence of quantum and classical effects was reported in the Mn12ac SMM, that is a cluster constituted by an external ring of eight Mn(III) ions and an internal tetrahedron of four Mn(IV) ions (see Fig. 1.5) [37].

The slow relaxation of the magnetization that characterizes SMMs comes from a combination of a large spin and an easy-axis magnetic anisotropy. In order to explain

the large spin, the isotropic exchange term in the spin Hamiltonian must be considered. It has the form [3]

$$H_{exc} = -\sum_{i<j} J_{ij} \mathbf{s}_i \cdot \mathbf{s}_j \tag{1.7}$$

where J_{ij} is the exchange constant between two generic metal states i and j having spin s_i and s_j respectively and the sum is over all the pairs of the cluster. If $J_{ij} > 0$, the ferromagnetic coupling between the spins, i.e. a parallel alignment of them, is favored, while for $J_{ij} < 0$ an antiferromagnetic coupling is present. The result of exchange interaction is that the SMM is characterized by a total spin state S, which in general varies from 0 or 1/2, depending on the total number of unpaired electrons being even or odd, respectively, up to the sum of all individual spins [38].

Considering the magnetic anisotropy, in SMMs the significant contribution is represented by magnetocrystalline anisotropy, that is brought in by a combination of spin-orbit coupling with the low-symmetry environment around the metal centers constituting the SMMs [38]. Dipolar contributions are in most cases negligible [38]. In order to take into account the anisotropy, the effective spin Hamiltonian includes a term [3]

$$H_{an} = \mathbf{S} \cdot \mathbf{D} \cdot \mathbf{S} \tag{1.8}$$

where $\mathbf{D}$ is a real, symmetric tensor. If the coordinate axes x, y and z are chosen parallel to the eigenvectors of $\mathbf{D}$, then $\mathbf{D}$ is diagonal and H_{an} can be written [3]

$$H_{an} = D\left[S_z^2 - \frac{1}{3}S\left(S+1\right)\right] + E\left(S_x^2 - S_y^2\right) \tag{1.9}$$

where S_x, S_y and S_z are spin operators, $D = D_{zz} - \frac{1}{2}D_{xx} - \frac{1}{2}D_{yy}$ represents the axial anisotropy and $E = \frac{1}{2}\left(D_{xx} - D_{yy}\right)$ the transverse (or rhombic) one, the value of which is intrinsically limited to $\frac{1}{3}D$.

The effect of magnetic anisotropy on the $(2S+1)$ states of the spin multiplet is that of partially removing their degeneracy even in the absence of an external field. Therefore, this effect is also called zero-field splitting (see Fig. 1.6).

SMMs have a negative D, corresponding to an easy-axis magnetic anisotropy, meaning that the system can be magnetized much more easily when the field is applied along the principal axis z. Moreover, the energy as a function of the angle of the magnetization with respect to z is a double well potential (see Fig. 1.6) with the ground spin states corresponding to the highest spin values $M_S = \pm S$ (M_S is the eigenvalue of S_z). The two wells are separated by an energy barrier that, in case of pure axial anisotropy, amounts to [3]

$$\Delta E = |D| S^2 \tag{1.10}$$

for integer S, while $\Delta E = |D|\left(S^2 - 1/4\right)$ for half-integer S. At low temperature, only the ground spin state is populated and the dynamics of the magnetization is in first approximation well described assuming that the whole molecule behaves like a unique

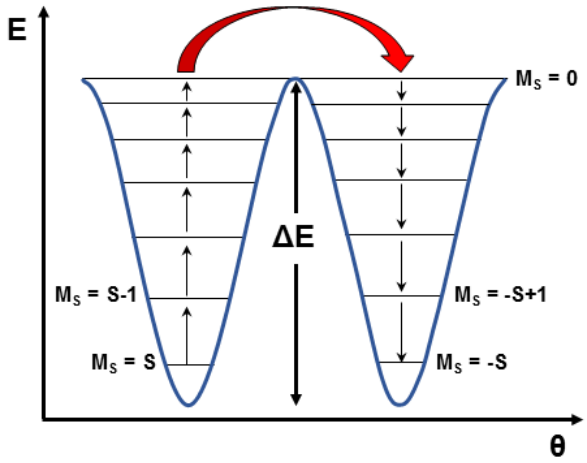

Figure 1.6: Energy of a single molecule magnet as a function of the angle between its magnetization and the z axis.

large spin characterized by its axial and transverse anisotropies (giant spin approximation). As for magnetic nanoparticles, magnetic anisotropy represents a fundamental property. The relation between the parameters accounting for it in the two nanomaterials is [26] $K = -\alpha DS^2$, where $\alpha = N_A\rho/MW$ (N_A is the Avogadro's constant, ρ is the density of the sample and MW is its molecular weight).

The application of an external magnetic field stabilizes one well. For example, if the field is applied parallel to magnetization axis z, levels with $M_S < 0$ are shifted down and levels with $M_S > 0$ are shifted up. Consequently, the population of the first ones is favored. Once the field is removed, the system returns to thermal equilibrium, i.e. an equal population of the two wells, corresponding to zero magnetization. Transitions from one state to the other one are promoted by deformations of the metal coordination environment (rotations and geometrical strains), which can affect the spin degrees of freedom, thanks to spin-orbit coupling [38]. However, at a first level of approximation, these deformations are only able to induce transitions between states with $\Delta M_S = \pm 1$ and $\Delta M_S = \pm 2$. Therefore, to overcome the energy barrier, a multiphonon mechanism is necessary [38]. The relaxation time of the magnetization follows an Arrhenius law analogous to that reported for magnetic nanoparticles (Eq. 1.6): for SMMs ΔE equals the energy barrier between the two wells. In general, the factor τ_0 is longer than that found in magnetic nanoparticles [38]. At low temperatures, the relaxation time is long and the system displays superparamagnetic behavior with the opening of a hysteresis loop.

Thanks to their molecular nature, SMMs exhibit an other mechanism for the reversal of the magnetization that is quantum tunnelling of the magnetization. In the case of pure axial symmetry in fact, the eigenstates of the Hamiltonian defined by Eq. 1.9 are pure $|M_S>$ states and transitions between states of the ground doublet with $M_S = \pm S$

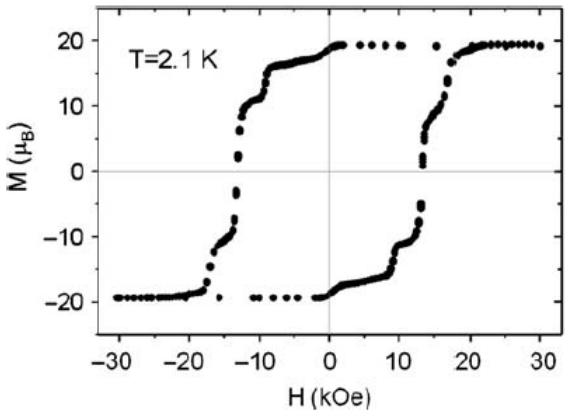

Figure 1.7: Hysteresis loop of a single crystal of the Mn12ac SMM with the applied field parallel to the tetragonal axis. Image taken from [38].

can only occur through a multiphonon process. However, in real systems a transverse anisotropy due to symmetry reduction or a transverse field, either externally applied or of intrinsic origin (dipolar or hyperfine), introduces in Eq. 1.9 terms in S_x and S_y that admix states with different M_S [38] and in particular states on opposite sides of the barrier. This is the origin of quantum tunnelling. The phenomenon is possible with zero applied magnetic field being all the unperturbed levels degenerate in pairs. When a magnetic field is applied, quantum tunnelling gives rise to steps in the hysteresis loop at resonant fields (see Fig. 1.7).

SMMs represent ideal model systems for the study of fundamental science, in particular at the interface between the classical and quantum regimes. Besides quantum tunnelling of the magnetization, they display other quantum effects, as Berry-phase interference [39] and quantum coherence [40]. However they have been proposed also for a variety of technological applications including high-density information storage, spintronics [7, 8, 9] and quantum computing [10, 11, 12].

The potentiality of SMMs for information storage relies on their hysteresis and the possibility for the system to be into two different magnetization states, namely magnetization up and magnetization down. Consequently, these states can be considered as representative of two different bits, namely bit 0 and bit 1. Moreover, thanks to their molecular dimensions SMMs would allow to obtain magnetic memories of extremely high density, about 10^4 times higher than the existing memory devices.

The application of SMMs for quantum computing is based on the possibility to use them as qubits [10]. The principal difference with respect to classical computation is the superposition of quantum states. Consequently, a qubit can be either $|1>$ or $|0>$ or any arbitrary superposition of these two states $|\psi> = \alpha|1> + \beta\ |0>$. SMMs are useful materials, because their energy levels and quantum states are well defined at the molecular level due to the fact that their basic units contain identical clusters of transition metals.

Finally, SMMs have been proposed as building blocks for spintronic devices. Spintronics stands for spin-based electronics and sees the contemporary exploitation of electronic and spin degrees of freedom of the system. In particular, spintronic systems exploit the fact that the electron current is composed of spin-up and spin-down carriers, which carry information encoded in their spin state and interact differently with magnetic materials [8]. Information encoded in spins persists when the device is switched off, can be manipulated without using magnetic fields and can be written using low energies, to cite just a few advantages of this approach [8]. Traditional materials for spintronics are inorganics, such as metals and semiconductors. The advantage due to the use of molecules relies on their small dimensions, which would imply not only the realization of ever-smaller electronic devices, but also the possibility to exploit quantum effects [8].

The actual use of SMMs in the proposed applications assumes that their magnetic properties are unchanged and in particular the magnetic anisotropy persists, when the molecules are deposited on a solid surface.

1.1.3.2 Single chain magnets

Single chain magnets (SCMs) are molecular spin chains displaying slow relaxation of the magnetization at low temperature.

Unlike SMMs, they are one-dimensional (1D) polymeric structures and their behavior relies on a large easy-axis magnetic anisotropy, a strong intrachain magnetic interaction and weak interchain magnetic interactions [41]. Ferromagnetic, ferrimagnetic or canted (non collinear local easy-axes) antiferromagnetic spin organizations are possible. The number of magnetic centers interacting consecutively is typically limited to 10^2 - 10^4 by naturally occurring defects, non-magnetic impurities or lattice dislocations [42]. The degree of spatial correlation is quantified by the correlation length ξ, that is defined as the characteristic length of the spatial decay of two-spin correlations [41]. If ξ is much smaller than the average distance between successive defects, the system can be considered as infinite, otherwise the system behaves like a collection of finite segments.

As for SMMs, the slow relaxation of the magnetization is associated with a sort of superparamagnetic behavior and the magnetization dynamics follows the thermally activated law described by Eq. 1.6. For SCMs however the dynamics is ruled by the Glauber dynamics [43]. In particular, in the approximation of an infinite chain, the relaxation process begins with the reversal of one spin in the chain. An Ising system can only assume two orientations and the energy cost of this initial reversal is $\Delta E = 4JS^2$, being J the magnetic exchange coupling between two neighboring spins [41]. At low temperature, the nucleation of the magnetic excitation can thus be a rather unlikely event and τ becomes very large. Once created, the domain wall can propagate itself along the chain at no energy cost or extinguish itself reversing back the initial spin. Every step in this propagation is constituted of a single spin flip. In real systems the presence of defects or impurities and interchain interactions can offer different and

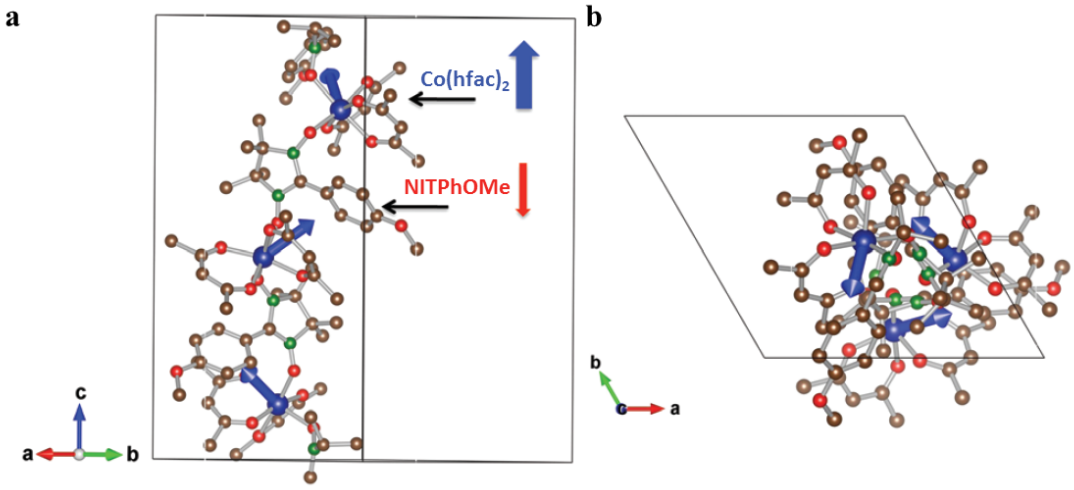

Figure 1.8: Crystal structure of the CoPhOMe single chain magnet: (a) side view; (b) top view. The Co atoms are depicted as large blue spheres, while O, N and C atoms are red, green and brown spheres, respectively. For the sake of clarity, F and H atoms are not shown. The metal-organic complex ($Co(hfac)_2$) and organic radical (NITPhOMe) are highlighted in the side view. The blue vectors depict the direction of the spin of Co atoms. Image taken from [45].

additional mechanisms of relaxation.

The interest in SCMs is driven by the fact that in principle they are able to show a larger barrier (and consequently a higher blocking temperature) than SMMs, because for SCMs its height depends on the strength of the exchange interaction [41]. Therefore this is a useful feature in order to use SCMs for memory storage.

The first 1D system to display slow relaxation of the magnetization was [$Co(hfac)_2$ (NITPhOMe)] (briefly called CoPhOMe) [44], that consists of alternating $Co(hfac)_2$ and radical moieties arranged in 1D arrays with a helical structure arising from the trigonal crystallographic lattice (see Fig. 1.8). The Co(II) ion and the radical are antiferromagnetically coupled and the chain behaves as 1D ferrimagnets, because of the noncompensation of their magnetic moments.

An interesting aspect of CoPhOMe relies on its helical structure and its crystallization in an acentric space group. These features give no symmetry constraints forbidding the development of an electric polarization or the observation of magnetochiral effects in it [45, 46]. Density functional calculations demonstrated the possible variation of a magnetically induced electric polarization in CoPhOMe, underlying a sizable magnetoelectric interaction with appealing perspectives in cross-coupled control of its magnetic and electric properties [45].

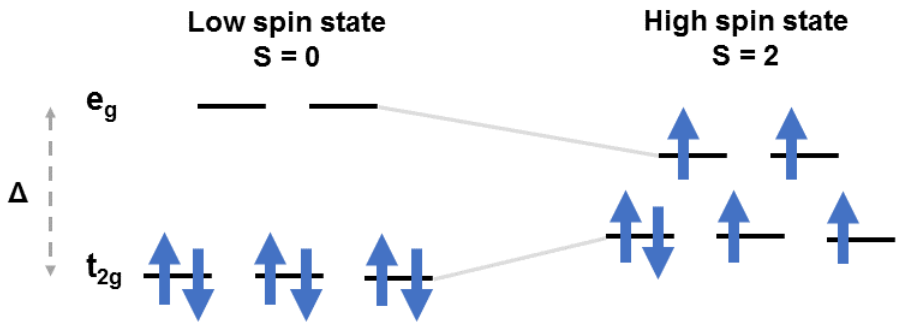

Figure 1.9: Scheme of the electronic energy levels and their occupation in the LS and HS states of an Fe(II)-based SCO complex.

1.2 Spin crossover complexes

Spin crossover (SCO) complexes are bistable systems, that can reversibly switch between two distinct spin states, a low spin (LS) and a high spin (HS), by means of a variety of external stimuli, such as temperature [47, 48], electromagnetic radiation of appropriate wavelength [49, 50, 51], pressure [52] and magnetic field [53].

SCO molecules consist of a d^4 to d^7 transition-metal ion surrounded by organic ligands [54, 55] that provide structural stability and prevent oxidation of the metal center [56]. The competition between the ligand field strength (Δ) and the spin pairing energy (or electron-electron repulsion) (P) is responsible for the bistability of the system (Fig. 1.9) [55]. When $\Delta > P$, the electrons tend to occupy the orbitals of lower energy (t_{2g}) and the metal complex adopts the LS state. If $\Delta < P$, the d electrons can distribute in the upper e_g states according to the Hund's rule and the result is the HS state. For SCO complexes based on Fe(II) (d^6) in a distorted-octahedral coordination environment, the electrons pair up in the t_{2g} level giving rise to a LS state with total spin $S = 0$, while the HS state has $S = 2$, because the electrons occupy the orbitals with the maximum spin multiplicity.

The two spin states have two different potential wells as a function of the Fe-ligand distance, the minima of which are displaced relative to each other, both vertically and horizontally [55] (see Fig. 1.10). The condition for the SCO transition is that the energy difference between the minima of the two states (ΔE^0_{HL}) be of the order of magnitude of the thermal energy: $\Delta E^0_{HL} \sim k_B T$. Consequently, at low T the SCO complex will be in the LS state, while at high T it will be found in the HS state. Moreover, the SCO transition is entropy driven [55].

The SCO transition towards the HS state is accompanied by a change in the molecular structure and magnetism of the system. The redistribution of the charges in the t_{2g} and e_g orbitals determines an increase of the metal-ligand length, that is of the order of 0.2 Å in Fe(II)-based complexes [57]. This translates into a change in the corresponding volume of the molecules of the HS and LS states. The redistribution of the charges in

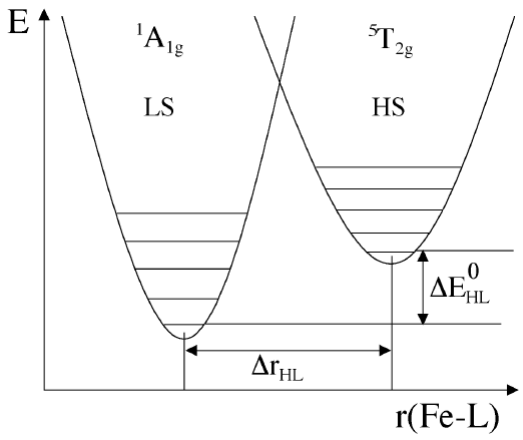

Figure 1.10: Potential wells for the LS and HS states as a function of the Fe-ligand distance. Image taken from [55].

the orbitals affects also the metal-donor atom stretching frequencies, that can be usually found in the low frequency region of Raman spectra (< 600 cm^{-1}) [54, 58]. Finally, the HS to LS ratio influences the paramagnetic properties of the system.

Besides the increase of the temperature, an alternative way to induce the SCO transition is the so-called LIESST effect (Light Induced Excited Spin State Trapping) [59, 60]: light irradiation with appropriate wavelength λ at low temperature promotes the molecules to a metastable HS state with typical lifetimes ranging from minutes to hours and even days [61]. The phenomenon can be understood by looking at the electronic structure of an Fe(II)-based complex [57](see Fig. 1.11). Irradiating the sample with green light ($\lambda = 514$ nm) at a temperature below 50 K stimulates the transition from the LS state ($^1A_1$) to the excited state ($^1T_1$). This state has a lifetime of the order of nanoseconds and, by means of a double intersystem crossing through the intermediate state ($^3T_1$), it can decay fast to the HS state ($^5T_2$). At low temperature, the $^5T_2$ state has a very long lifetime, because the relaxation to $^1A_1$ is forbidden. The system can be converted back to the LS state by raising the temperature above 50 K or by irradiating it with red light ($\lambda = 820$ nm), that is the so-called reverse LIESST. In this case the molecules are promoted to an HS excited state, from which they decay to the $^3T_1$ state and finally to the $^1A_1$ state.

Although the origin of the SCO phenomenon is purely molecular, the macroscopic manifestation in the solid state is the result of the cooperative interaction of the molecules that constitute the material [57]. Cooperativity stems from the change in volume of the SCO molecule. Therefore, it has an elastic origin leading to long-range interactions and intermolecular interactions can strongly affect the SCO phenomenon. The degree of cooperativity associated with the transition, that can be defined as the extent to which the effects of the spin change are propagated throughout the solid, can be inferred by observing the spin transition curve of the system, i.e. the variation of

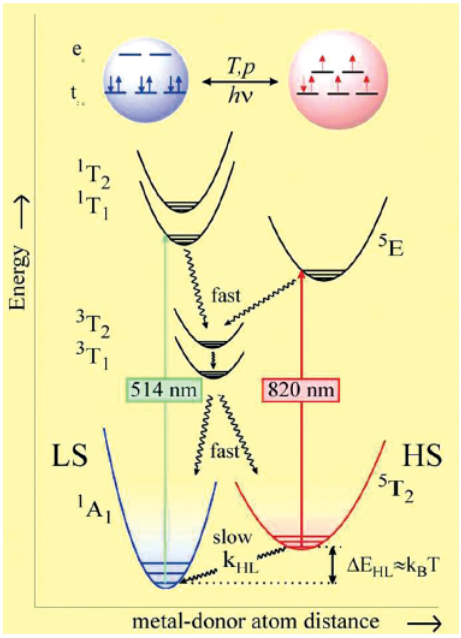

Figure 1.11: Scheme of the electronic structure of an Fe(II)-based complex showing the mechanisms of the LIESST and reverse-LIESST effects. Image taken from [57].

the HS fraction as a function of the temperature [54]. Three examples of spin transition curves are reported in Fig. 1.12. A gradual transition is encountered when cooperative interactions are relatively weak, while an abrupt transition is encountered when a strong cooperativity is present. Finally, when the cooperativity is high, a hysteresis loop appears, conferring bistability to the system and consequently a memory effect.

The possibility to control the spin state of the system via an external input makes SCO complexes promising building blocks for spintronic [7, 15] and high-density memory devices, as well as potential elements for displays and sensors [13, 14]. In view of the development of nanoscale devices, it is of fundamental importance that the molecules retain their SCO features when they are deposited on a solid substrate. Considering that the SCO features depend on the environment surrounding the molecule, the SCO behavior of the molecules can be altered by the interaction with the substrate with respect to molecules in the bulk phase.

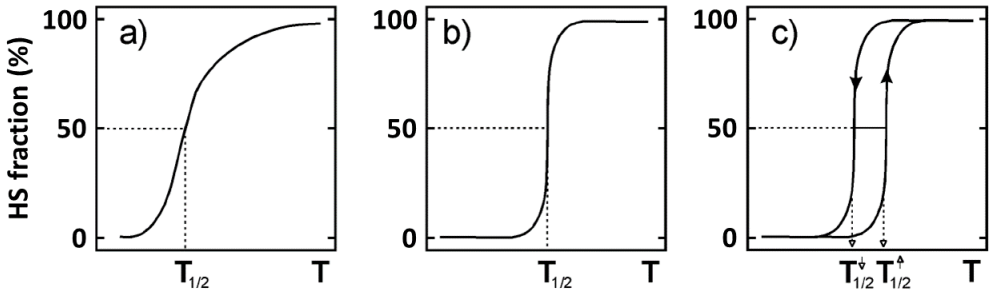

Figure 1.12: Three examples of spin transition curves: gradual transition (a), abrupt transition (b) and transition with hysteresis (c). Image taken from [54].

Chapter 2

Spectroscopic techniques

In this Chapter, an introduction to the spectroscopic techniques used to characterize the nanomaterials studied in this thesis is given. First, Mössbauer spectroscopy is presented, then electron paramagnetic resonance spectroscopy is described.

2.1 Mössbauer spectroscopy

Mössbauer spectroscopy is a spectroscopic technique based on the resonant emission and absorption of gamma rays by nuclei in a solid. It is based on the Mössbauer effect, which has been observed in more than 100 nuclear isotopes. Thanks to its high energy sensitivity, this technique allows the investigation of the hyperfine interactions of the probed nucleus.

In the first Section, the theoretical principles at the base of the Mössbauer effect are presented, while in second Section the main features of a Mössbauer spectrum are introduced. In the third Section, a discussion of the hyperfine interactions that characterize a Mössbauer spectrum is given. Finally, in the last two Sections the technical aspects of a conventional setup for Mössbauer spectroscopy and of the Synchrotron Mössbauer Source are reported.

2.1.1 Mössbauer effect

Mössbauer spectroscopy is based on the Mössbauer effect, which was discovered by Rudolf L. Mössbauer in 1958 [62, 63]. Investigating the resonant absorption of 129 keV gamma rays in ^{191}Ir nucleus, he discovered that the resonant absorption did not follow the classically expected behavior at low temperature, but it increased while reducing the temperature. He considered that this phenomenon was possible only if the source nucleus ^{191}Os and the absorber nucleus ^{191}Ir were rigidly bound in the crystal lattices: this condition allowed to eliminate the energy loss due to the recoil of the emitting nucleus.

Consider in fact a free nucleus of mass M and velocity v_x, which is in an excited state of energy E_e (see Fig. 2.1); suppose that it decays to the ground state (of energy

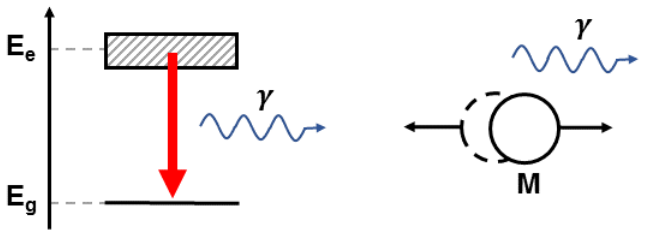

Figure 2.1: Recoil of a free nucleus of mass M after emitting a gamma ray.

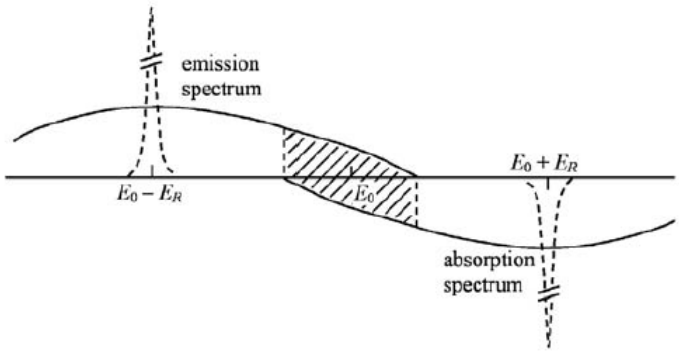

Figure 2.2: Emission and absorption gamma ray spectra when the excited nucleus is at rest (dashed lines) or moves because of thermal motion (solid lines). Image taken from [64].

E_g) by emitting a gamma ray of energy E_γ in the same direction of motion. The process is described by the laws of momentum conservation and energy conservation [64]

$$\begin{cases} Mv_x = \frac{E_\gamma}{c} + M\left(v_x - v_R\right) \\ E_e + \frac{1}{2}Mv_x^2 = E_g + E_\gamma + \frac{1}{2}M\left(v_x - v_R\right)^2 \end{cases} \tag{2.1}$$

where v_R is the recoil velocity of the nucleus after the emission of the photon. From the above equations we can write

$$E_\gamma = (E_e - E_g) - \frac{1}{2}Mv_R^2 + Mv_x v_R = E_0 - E_R + E_D \tag{2.2}$$

where $E_0 = E_e - E_g$ is the energy difference between the excited state and the ground state, $E_R = \frac{1}{2}Mv_R^2 = \frac{E_\gamma^2}{2Mc^2}$ is the recoil energy and $E_D = Mv_x v_R = \frac{v_x}{c}E_\gamma$ is the so-called Doppler energy shift.

In order to have resonant absorption, the emission and absorption spectra of the nuclei must have a non-zero overlapping. Two cases can be distinguished.

In the ideal case that the excited nucleus is at rest ($v_x = 0$), $E_D = 0$ and the energy spectrum of the emitted gamma rays is a sharp peak centered at $E_0 - E_R$ with a full width at half maximum that is approximately equal to the natural width (Γ_n) of the excited energy level (see Fig. 2.2). The gamma rays can be resonantly absorbed by the nuclei in the ground state level, which transit to the excited one, and the energy spectrum of the absorbed gamma rays is identical to the emission spectrum, except for the position of its center, which is $E_0 + E_R$. The energy difference between the emitted and absorbed gamma rays is $2E_R$. Therefore, the necessary condition for the resonant absorption of the photon is

$$\frac{\Gamma_n}{2E_R} > 1 \tag{2.3}$$

that is, the recoil energy must be less than half of the natural width of the excited state. This condition is at the base of the different properties of resonant scattering of photons in an atom or a nucleus. If we consider atoms emitting photons with wavelength in the visible region, as for example the Na atom ($E_\gamma = 2.1$ eV, $\Gamma_n = 4.39 \times 10^{-8}$ eV), the condition is always satisfied: the emission and absorption spectra are almost overlapping. On the contrary, for a nucleus of ^{57}Fe ($E_\gamma = 14.4$ keV, $\Gamma_n = 4.65 \times 10^{-9}$ eV) this does not happen: the recoil energy is about six orders of magnitude higher than that of the Na atom. The reason is that, while the natural widths of a nucleus and an atom are comparable, the former gives a more energetic photon than the latter, usually by three orders of magnitude. Consequently, resonant absorption of gamma rays is usually not observed.

In the usual case $v_x \neq 0$, because of the random thermal motions of free atoms. Their velocities can be described by a Maxwell distribution and this broadens the emission and absorption spectra. This broadening is due to the Doppler effect and the width of the emission spectral line is $\Delta E_D = 4\sqrt{E_R k_B T ln 2}$ (where k_B is the Boltzmann constant) [64]. For ^{57}Fe at $T = 300$ K $\Delta E_D = 2.4 \times 10^{-2}$ eV, which is greater than $2E_R$. Therefore, the emission and absorption spectra partially overlap (see the solid lines of Fig. 2.2) and some effect of resonant absorption can be observed.

The result is that for a nucleus that is free to move the lost energy due to recoil must be compensated in order to observe substantial resonant absorption of gamma rays. For this reason the first experiments (before 1954) were realized by placing the source on a high-speed rotor (in order to compensate the recoil energy loss by means of the Doppler effect) [65] or keeping the source at high temperature (in order to increase the Doppler broadening). However all these experiments involved recoil and encountered low energy counts and poor energy resolution. Mössbauer discovery of the possibility to realize resonant absorption without recoil eliminated the need to compensate for energy loss.

In a crystal lattice in fact an atom is held in its equilibrium position by chemical bonds having a typical energy of ~ 10 eV. For a free ^{191}Ir nucleus $E_R = 4.7 \times 10^{-2}$ eV, that is much smaller than the chemical bond energy. Therefore, one can think that, when the gamma ray is emitted by a nucleus bound in a lattice, the entire crystal lattice (a total of 10^{18} atoms) recoils. Consequently, the recoil energy becomes negligible

($\sim 10^{-20}$ eV), Eq. 2.3 is satisfied and Eq. 2.2 is simplified into $E_\gamma \approx E_0$: the process is a recoilless resonant absorption.

In reality, a nucleus is not rigidly bound to a lattice, but it is free to vibrate about its equilibrium position and photons can exchange energy with the lattice by means of phonons. However, in the approximation of an Einstein solid with one vibrational frequency ω, the lattice can receive or release only integral multiples of energy $\hbar\omega$. Therefore, if $E_R < \hbar\omega$, the lattice cannot absorb the recoil energy and the gamma ray is emitted without recoil (zero-phonon process). The probability of having such a process is known as recoilless fraction or Lamb-Mössbauer factor (f) and can be defined as [64]

$$f = e^{-k^2 < x^2 >} \tag{2.4}$$

where $< x^2 >$ is the mean square displacement of a nucleus along the direction of the wave vector $\overrightarrow{k}$ of the emitted gamma ray. This relation implies that the Mössbauer effect is favored in solids showing transitions with gamma rays of low energies.

From the Debye model of the phonon spectrum of solids, the temperature dependence of f can be derived [64]

$$f\left(T\right) = exp\left\{-\frac{3E_R}{2k_B\theta_D}\left[1 + 4\left(\frac{T}{\theta_D}\right)^2 \int_0^{\theta_D/T} \frac{xdx}{(e^x - 1)}\right]\right\} \tag{2.5}$$

where θ_D is the Debye temperature of the solid, that represents a measure of the strength of the bonds between the Mössbauer atom and the lattice. Eq. 2.5 shows that the recoilless fraction increases with decreasing temperature and with increasing the Debye temperature of the solid.

Together with the indications on f, it is worth noting that the lifetimes of excited nuclear states suitable for Mössbauer spectroscopy range from $\sim 10^{-6}$ s to $\sim 10^{-11}$ s [66]. Lifetimes out of this range would give too narrow or broad lines, implying insufficient overlap between the absorption and emission spectra.

The Mössbauer effect has been observed with nearly 100 nuclear transitions in about 80 nuclides distributed over 43 elements [67]. Nearly 20 elements have proved to be suitable for practical applications. The most extensively studied isotope is ^{57}Fe.

2.1.2 Mössbauer spectrum

A Mössbauer spectrum is a recoilless resonance curve. It is measured by taking advantage of the Doppler effect in order to modulate the energy of the gamma ray within a small range $E_\gamma\left(1 \pm v/c\right)$. For this reason the source is mounted on a velocity transducer that moves with respect to the absorber and the emitted gamma ray energy is therefore modulated. The Mössbauer absorption spectrum records the counts of the gamma rays transmitted through the absorber as a function of the gamma ray energy (see Fig. 2.3). In reality, it is customary to record the spectrum as a function of the transducer velocity.

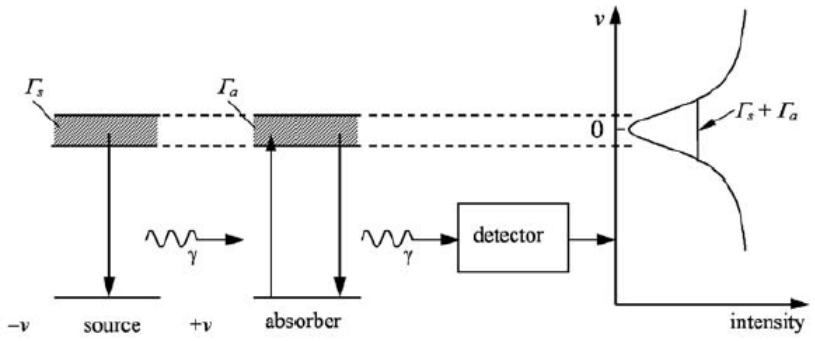

Figure 2.3: Measurement of a Mössbauer spectrum. Image taken from [64].

The absorption lineshape is the convolution of the source lineshape and the absorption cross-section. If they can be approximated with Lorentzian distributions with widths Γ_s and Γ_a respectively, the lineshape of the Mössbauer spectrum is also Lorentzian with width $\Gamma_s + \Gamma_a$; in the approximation of thin samples $\Gamma_s + \Gamma_a \sim 2\Gamma_n$.

The actual shape and intensity of a transmission spectrum depends on the absorber thickness. In particular, the intensity of the detected gamma rays $Y(E)$ is described by the transmission integral function [64]

$$Y(E) = N_b(E)\left\{1 - \int_{-\infty}^{+\infty} L\left(E - \frac{v}{c}E_0\right)\left[1 - e^{-(t_a\sigma(E))}\right]dE\right\} \tag{2.6}$$

where $N_b(E)$ is the spectrum baseline, $L\left(E - \frac{v}{c}E_0\right)$ is the Lorentzian distribution (centered in E_0) of the emitted gamma rays, $\sigma(\omega)$ is the absorption cross-section and t_a is the effective thickness of the sample.

The effective thickness of the sample is defined [64]

$$t_a = n_a f \sigma_0 d \tag{2.7}$$

where n_a is the number of Mössbauer nuclei in the absorber per unit mass, f is the absorber recoilless fraction, σ_0 is the maximum resonance cross-section and d is the thickness of the absorber (in mg/cm^2). The effective thickness is temperature dependent, in the same manner as f.

2.1.3 Hyperfine interactions

Thanks to its high energy resolution, Mössbauer spectroscopy allows to study the microscopic environment surrounding a nucleus, by investigating its hyperfine interactions. The hyperfine interactions are defined as the interactions between the probed nucleus and the electromagnetic fields produced by the surrounding electrons and neighboring atoms or ions. In a Mössbauer spectrum three kinds of interactions can be recognized:

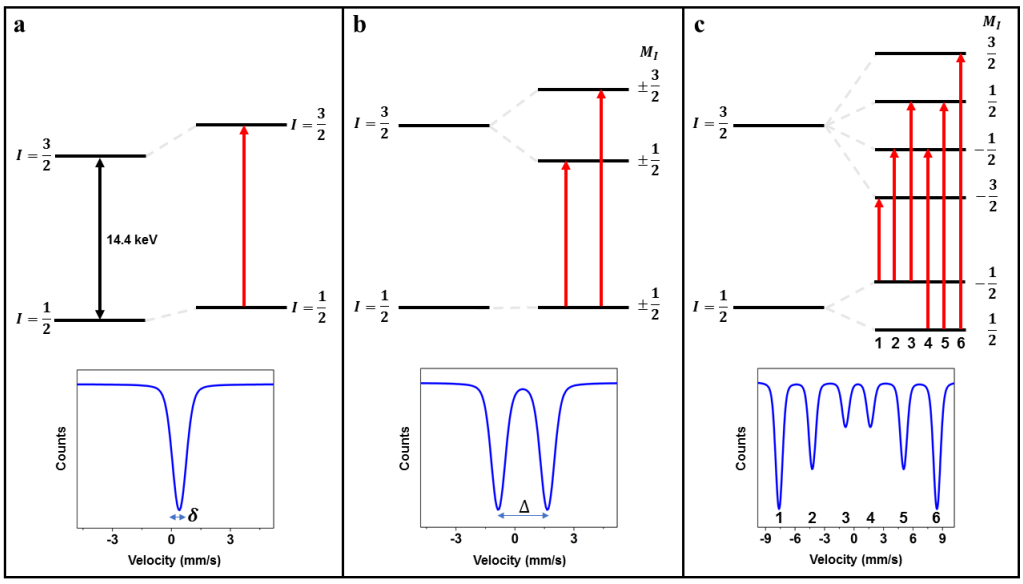

Figure 2.4: Schematic representation of the hyperfine interactions of an ^{57}Fe nucleus. a) Isomer shift (δ); b) Quadrupole splitting (Δ) ($V_{zz} > 0$ is considered); c) Hyperfine magnetic splittings.

the electric monopole and quadrupole interactions, which are responsible for isomer shift and quadrupole splitting of the spectral lines respectively, and the magnetic dipole interaction, which causes magnetic hyperfine splittings.

2.1.3.1 Isomer shift

Isomer shift is a shift of the entire resonance spectrum with respect to the zero value of the velocity axis, that corresponds to the average energy of the photons emitted by the source at rest.

This effect relies on the fact that the nucleus cannot be considered as a point charge, but has a finite volume and a charge distribution inside it. Consequently, from the second order expansion of the Coulomb interaction energy between the nucleus and the electric charges outside it, the monopole interaction energy can be written [64]

$$\delta E = \frac{2\pi}{3} ze^2 |\psi(0)|^2 < r^2 >$$

where ze is the nuclear charge, $< r^2 >$ is the mean-square radius of the nuclear charge distribution and $-e|\psi(0)|^2$ is the s electron charge density at the origin. Therefore, δE represents the energy shift of an energy level with respect to the point charge nucleus. Considering that the fundamental and the excited states have different nuclear radii, the corresponding shifts can be different. Furthermore, the same Mössbauer isotope in the source and in the absorber can be in different chemical environments, i.e. it can sense

different $|\psi(0)|^2$. The result is that the energy levels in the source and absorber have different δE and the peak position of the Mössbauer spectrum is shifted with respect to $v = 0$ mm/s by an amount δ, that is called isomer shift (see Fig. 2.4a). It is defined [64]

$$\delta = \frac{2\pi}{3} z e^2 \left(|\psi_a(0)|^2 - |\psi_s(0)|^2 \right) \left(< r^2 >_e - < r^2 >_g \right) \tag{2.8}$$

It depends on the difference between the s electron charge densities at the nuclei in the absorber and the source and on the difference between the mean squares of the charge radii of the excited and ground states.

A measurement of δ is essentially a measurement of the difference between the s electron charge densities at the nuclei in the absorber and the source. However, these densities do not rely on the occupation of the s electron shells alone, but they depend also on the population of valence orbitals which modifies the s electrons wavefunctions [64]. Consequently, δ relies on the properties of the electronic structure and chemical bonds. Therefore, information on the character of the chemical bond, as well as on the oxidation state, spin state, electronegativity of a ligand and coordination number can be deduced from it [64].

It is worth noting that δ usually has values of few tenths of mm/s corresponding to energy shifts of the order of 10^{-8} eV: only Mössbauer spectroscopy can detect such small energy shifts.

In general, a second contribution to the isomer shift, called second-order Doppler shift, has to be taken into account. The origin of this term is the relativistic shift of the energy of the gamma photon due to the thermal motion of the emitting and absorbing nuclei, which is proportional to the mean square velocity of the Mössbauer nuclei. Assuming that the emitting or absorbing atom is vibrating with mean-square velocity $< v^2 >$, the second-order Doppler shift is given by [64]

$$\delta_{SOD} = -E_\gamma \frac{< v^2 >}{2c^2}$$

where c is the velocity of light.

Considering that for metallic iron at room temperature $< v^2 >$ is of the order of 10^{10} mm^2/s^2, the energy shift associated to δ_{SOD} is of the order of 10^{-9} eV.

Since $< v^2 >$ is proportional to the kinetic energy of the Mössbauer atom, the value of δ_{SOD} decreases with the temperature. The temperature dependence of δ_{SOD} is related to that of the recoilless fraction f. While f depends on the atomic mean-square displacement ($< u^2 >$) and δ_{SOD} on $< v^2 >$, both quantities $< u^2 >$ and $< v^2 >$ can be derived from the Debye model for the energy distribution of phonons in a solid.

A useful relation between δ_{SOD} and f is represented by [64]

$$S_T = \frac{\ln f}{\delta_{SOD}} = \frac{-k^2 < u^2 >}{- < v^2 > /2c}$$

A linear relation between $\ln f$ and δ_{SOD} is predicted by the Debye model and it is experimentally confirmed for ^{57}Fe impurities in six different fcc crystals in a wide range

of temperature from 100 K to 1020 K [68]. Considering that the effective thickness t_a is proportional to f, a linear relation holds also between δ_{SOD} and $\ln t_a$.

2.1.3.2 Quadrupole splitting

Quadrupole splitting is a splitting of otherwise degenerate energy levels, that is due to the existence of a nuclear electric quadrupole moment. From the second order expansion of the Coulomb interaction energy between the nucleus and the electric charges outside it, together with the term responsible for the isomer shift, a second term can be written of the form [64]

$$\Delta E = \frac{1}{6} \sum_{i,j=1}^{3} V_{ij} Q_{ij}$$

where Q_{ij} is the nuclear quadrupole moment tensor and V_{ij} is the electric field gradient (EFG) tensor evaluated at the nucleus. In the case of an axially symmetric nucleus, its symmetry axis (i.e. its quantization axis) can be chosen as the principal axis z' of the nuclear quadrupole moment tensor; in this coordinate system only one independent quantity Q is needed to describe the nuclear quadrupole moment [64]: $eQ = Q_{33}$ or

$$Q = \frac{1}{e} \int \left(3z'^2 - \mathbf{r}'^2\right) \rho_n \left(r'\right) d\tau'$$

where $\rho_n \left(\mathbf{r}'\right)$ is the nuclear charge density in $\mathbf{r}'$ and the integral is calculated on the entire volume of the nucleus. Consequently, if the nucleus has a prolate shape (longer along z'), then $Q > 0$; if the shape is oblate, $Q < 0$. Only nuclei with spin $I > 1/2$ have $Q \neq 0$.

Passing to the EFG tensor, its principal axis is usually chosen such that $|V_{zz}| \geq |V_{xx}| \geq |V_{yy}|$ and consequently two parameters can be used to describe it: V_{zz} and $\eta = \left(V_{xx} - V_{yy}\right) / V_{zz}$, that is called asymmetry parameter.

By evaluating the eigenvalues of the Hamiltonian for quadrupole interaction $H = \frac{1}{2} \sum_{i,j=1}^{3} V_{ij} Q_{ij}$ we have [64]

$$E = \frac{eQV_{zz}}{4I\left(2I-1\right)} \left[3M_I^2 - I\left(I+1\right)\right] \left(1 + \frac{\eta^2}{3}\right)^{\frac{1}{2}}$$

where $M_I = I, I-1, ... -|I|$.

In the case of the ^{57}Fe nucleus the ground state has nuclear spin $I = 1/2$ and then $Q = 0$, while the first excited state (lying 14.4 keV higher in energy) has $I = 3/2$ and therefore this level is split into two sublevels ($M_I = \pm 3/2$ and $M_I = \pm 1/2$) by the quadrupole interaction; since M_I is squared in the formula, the two sublevels are doubly degenerate (see Fig. 2.4b).

The energy difference between the two sublevels is the quadrupole splitting, which is defined [64]

$$\Delta = \frac{eQV_{zz}}{2}\left(1+\frac{\eta^2}{3}\right)^{\frac{1}{2}} \tag{2.9}$$

Since $Q > 0$, the sign of Δ is given by the sign of the V_{zz} component of the EFG; depending on it being positive or negative it determines whether the energy level associated with the $|\pm 3/2>$ state is higher or lower in energy with respect to the $|\pm 1/2>$ state. The intensities of the lines depend on the polar and azimuthal angles of the incident gamma ray in the EFG principal axis system [64] and in general they are different: only in the cases of polycrystalline or powder samples the two lines have the same intensity.

As previously stated, quadrupole splitting is present whether the energy level has a non zero electric quadrupole moment; moreover, it depends on EFG and the electric charges distributed around a Mössbauer nucleus contribute to it only when they have a symmetry lower than cubic. In general, two contributions to the EFG can be recognized [64]: the charges on the neighboring ions or ligands surrounding the Mössbauer nucleus (the so-called lattice contribution) and the charges in partially filled valence orbitals of the Mössbauer nucleus (the so-called valence electron contribution). The quadrupole splitting gives information on the oxidation state, spin state and local symmetry around the Mössbauer nucleus [64].

Finally, it is worth noting that the term quadrupole shift is used in place of quadrupole splitting to indicate the energy shift of the $|\pm 3/2>$ doublet, the value of which is half of that of the quadrupole splitting.

2.1.3.3 Hyperfine magnetic splittings

The hyperfine magnetic splittings are splittings of otherwise degenerate energy levels due to an interaction between the nuclear magnetic dipole moment $\boldsymbol{\mu}$ and a magnetic field $\mathbf{B}$ produced by the electrons or ions surrounding the nucleus. The interaction is described by the Hamiltonian [64]

$$H = -\boldsymbol{\mu}\cdot\mathbf{B} = -g\mu_N\mathbf{I}\cdot\mathbf{B}$$

where g is the nuclear g-factor and μ_N is the nuclear magneton. The energy of the corresponding sublevels is [64]

$$E_M = -gM_IB\mu_N$$

The interaction lifts the degeneracy of the energy level of a nucleus of spin I and splits it into $2I+1$ sublevels. For the ^{57}Fe nucleus the ground state is split into two sublevels and the first excited state into four sublevels, that are equally spaced by $gB\mu_N$; since the ground and excited states have different g-factors, the splitting between the sublevels is different in the two states (see Fig. 2.4c). For the transitions between a sublevel of the ground state and a sublevel of the excited state the selection rules for magnetic dipole transitions hold: $\Delta I = \pm 1$, $\Delta M_I = 0, \pm 1$. The six allowed transitions

give rise to six absorption lines, that constitute the characteristic sextet of ^{57}Fe. The intensity of the lines depends on the polar and azimuthal angles that describe the direction of the incoming gamma ray with respect to the direction of the magnetic field [64]; if the magnetic field vectors at the nuclei are randomly oriented the intensity ratio between the lines is 3:2:1:1:2:3.

In general, the magnetic field at the Mössbauer nucleus is the sum of two terms [64]: a local magnetic field, due to an external magnetic field or a magnetic ordering of the material, and a hyperfine magnetic field due to the own electrons of the Mössbauer atom. This last contribution (usually the majority one) can be further divided into three contributions [64]: the Fermi contact field, that is produced by the s electron spin density at the nucleus; the orbital field, due to the orbital motions of the unpaired electrons around the nucleus; the dipole field at the nucleus, produced by the total spin magnetic moment of the valence electrons.

It is worth noting that in paramagnetic compounds the coupling between the atomic magnetic moments is weak and thermal excitation determines casual fluctuations of the spins (with a characteristic time called relaxation time τ_R). Consequently, the hyperfine field at the nucleus fluctuates rapidly, so that the nucleus cannot feel its instantaneous value, but an average zero value. Therefore, in order to observe the hyperfine field, the condition $\tau_R > \tau_L$ must be realized [64], where τ_L is the Larmor precession period of the nucleus in the magnetic instantaneous field.

The hyperfine splittings give information on the magnitude and orientation of the hyperfine magnetic fields and more generally on the magnetic properties of the material. Without the necessity to introduce an external magnetic field, Mössbauer spectroscopy can be used for example to study the temperature dependence of spontaneous magnetization, to detect phase transitions and determine phase compositions and to study magnetic lattice anisotropy and relaxation phenomena [64].

To conclude this presentation of the hyperfine interactions, it is worth noting that, when both an EFG and a magnetic field are present, the shape of the Mössbauer spectrum depends not only on the relative weights of the corresponding interactions, but also on the relative orientations of the EFG principal axis, the magnetic field and the incident gamma ray.

2.1.4 Conventional Mössbauer setup

A conventional setup for Mössbauer spectroscopy is essentially composed of a radioactive source, a velocity transducer and a gamma ray detector; a scheme of the spectrometer in transmission geometry is reported in Fig. 2.5.

The source is mounted on a transducer, that oscillates between positive and negative velocities, modulating in this way the energy of the emitted gamma rays, according to the Doppler effect $\Delta E = \frac{v}{c} E_\gamma$. The emitted photons are limited by a collimator and traverse the sample. The transmitted photons are revealed by a detector and registered as a function of the velocity.

As previously noted in Section 2.1.2, the Mössbauer spectrum is the convolution

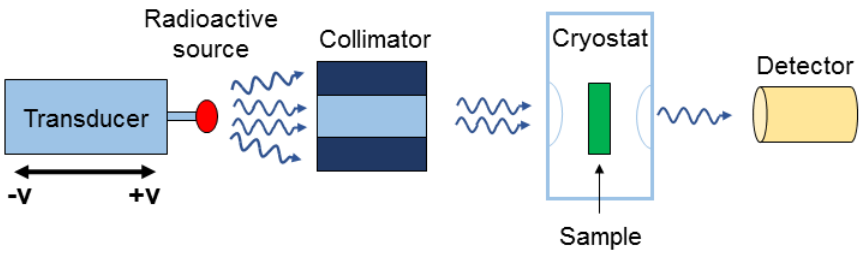

Figure 2.5: Principal components of a conventional Mössbauer setup in transmission geometry.

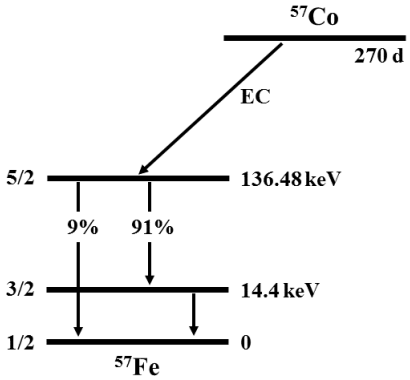

Figure 2.6: The nuclear decay scheme of ^{57}Co.

of the emission spectrum of the source and the absorption spectrum of the sample; in the approximation that both spectra have a Lorentzian distribution with FWHM equal to the natural linewidth of ^{57}Fe ($\Gamma_n = 0.097$ mm/s), the Mössbauer spectrum is still Lorentzian and the FWHM has a minimum value of about 0.194 mm/s. This translates into an energy resolution of the order of 10^{-9} eV. This feature allows Mössbauer spectroscopy to detect the local hyperfine interactions affecting the Mössbauer-active nuclei.

Usually the transducer is at room temperature, while the sample is inside a cryostat in order to study the evolution of the spectra at cryogenic temperatures. With a conventional setup in transmission geometry polycrystalline powder samples can be studied. The sensitivity of the setup is of the order of 10^{16} ^{57}Fe atoms per cm^2 [66].

The kind of radioactive source depends on the Mössbauer nucleus under study, i.e. on the required energy of the gamma rays in order to have resonant absorption.

For the study of the ^{57}Fe nucleus the source is constituted of a radioactive isotope of Co (^{57}Co) in a Rh matrix. The Co atoms are substitutional impurities inside the fcc crystal lattice of Rh; being diluted in the matrix, the Co atoms have the same local

surrounding of pure Rh and consequently the same nuclear energy levels; consequently, they emit gamma rays of the same energy. The nuclear decay scheme of ^{57}Co is reported in Fig. 2.6. ^{57}Co decays by electron capture with a half-life of 270 days into an excited level of iron, that decades to its ground state directly, by emitting a 136 keV gamma ray, or, more probably, by emitting two gamma rays with energies of 122 keV and 14.4 keV, respectively. This last photon is used for the resonant absorption by ^{57}Fe. The use of Rh as host material gives an f value of 0.784 for the source at room temperature [64]. Considering a radioactive source with an activity of 10 mCi at a distance of 10 cm from the absorber, the intensity on it can be estimated to be of the order of 10^4 photons/s. The principal features of a conventional radioactive source used for Mössbauer spectroscopy of the ^{57}Fe nucleus are reported in Table 2.1.

2.1.5 Synchrotron Mössbauer Source

The use of synchrotron radiation for Mössbauer measurements goes back to the mid of the '80s and it is based on the possibility to have a polarized pulsed radiation of high intensity, high collimation and narrow beam [64]. The brilliance of a third generation synchrotron source is about 12 orders of magnitude higher than that of a ^{57}Co source with an activity of 3.7×10^8 Bq [64]. Synchrotron radiation is not monochromatic; however its energy can be adjusted such that it covers an energy interval that is suitable for a majority of Mössbauer transitions. By means of high efficiency monochromators based on electron scattering, a linewidth of meV can be achieved [64].

The pulsed nature of synchrotron radiation favored the development of time-domain Mössbauer spectroscopy [64]. The data obtained by this technique can be considered as the "Fourier transform" of the conventional spectroscopy in the energy-domain. Using a short pulse ($<10^{-10}$ s) of synchrotron radiation it is possible to excite the entire nuclear ensemble and observe its coherent decay at different time intervals; in particular the prompt radiation scattered by the electrons (as a background) and the delayed radiation of nuclear resonant scattering are separated in time. The spectrum revealed as a function of time is characterized by beats and from its analysis information on the hyperfine interactions can be obtained [64]. However, in case of molecular samples (i.e. samples where the isotope under study is present in different coordinations), the resulting spectrum is difficult to interpret, because of the complex scheme of the beats due to the high number of transitions; moreover, the high intensity of synchrotron radiation can cause radiation damage.

Energy-domain Mössbauer spectroscopy of ^{57}Fe based compounds can be realized by taking advantage of the Synchrotron Mössbauer Source (SMS) available at ID18, the nuclear resonance beamline [69] of the "European Synchrotron Radiation Facility" (ESRF). SMS is characterized by the possibility to adequately filter the broad synchrotron radiation into a narrow ^{57}Fe-resonant line and to realize measurements in grazing incidence geometry. A scheme of the principal components of SMS is reported in Fig. 2.7.

The undulator of the line is set to provide synchrotron radiation with an energy of

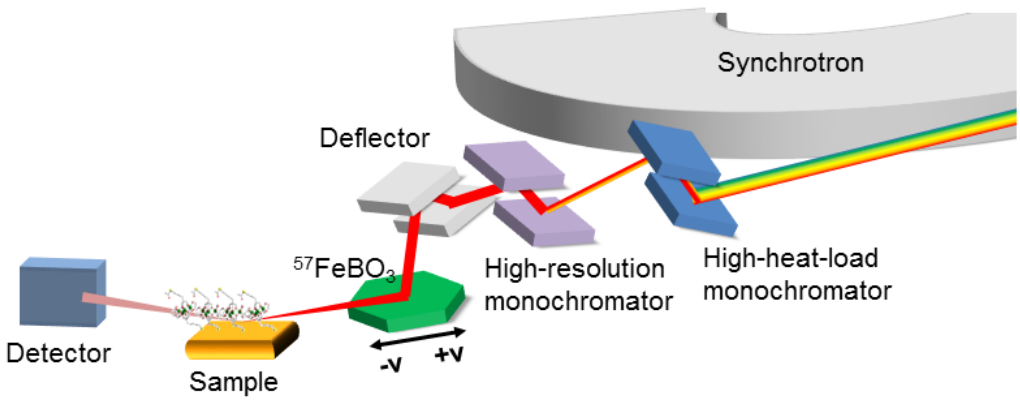

Figure 2.7: Scheme of the principal components of the Synchrotron Mössbauer Source.

about 14.4 keV. The bandwidth of the radiation is reduced in three steps [70]. First, a high-heat-load monochromator reduces the bandwidth of the beam to $\sim$ 2 eV and then a high-resolution monochromator reduces it further to $\sim$ 15 meV. Finally, the bandwidth is further reduced by taking advantage of pure nuclear reflections inside an iron borate ($^{57}FeBO_3$) crystal, which is kept at a temperature in the proximity of its Néel temperature (348.35 K) and in a magnetic field of 10 mT: in these conditions the crystal behaves like a nuclear resonant monochromator. The crystal is a high-quality single crystal enriched in ^{57}Fe up to 95% and is a platelet of linear dimensions $\sim$ 5 mm $\times$ 3 mm and thickness $\sim$ 35 μm. In this crystal all the reflections (NNN) with N odd are forbidden for electronic diffraction, but they are allowed for nuclear diffraction, therefore they are called pure nuclear reflections. Because of the hyperfine magnetic splitting of the ^{57}Fe nuclear levels in the ground and first excited states, the energy spectrum of the reflected radiation consists of many lines. However, if the crystal is heated to its Néel temperature, the energy spectrum of the reflected radiation collapses into a single line [71, 70] with a FWHM of the order of the natural linewidth and it is very sensitive to the values of both the temperature and the magnetic field applied along the crystal. For this reason the crystal is placed in an furnace, optimized to give a homogeneous distribution of temperature. The furnace is mounted on a transducer that oscillates similarly to what happens in a conventional Mössbauer setup.

After the iron borate crystal the radiation has a bandwidth of 10 - 15 neV and an intensity of about 10^4 photons/s [70]. Its energy spectrum can be described by a squared Lorentzian $L^2(E) = \left[\frac{\Gamma/2}{(E-E_0)^2+(\Gamma/2)^2}\right]^2$ [70], where E_0 is the resonance energy and Γ is its bandwidth. Contrarily to a conventional radioactive source, the radiation is fully recoilless and linearly polarized (with the electric field vector lying in the vertical to the plane of the laboratory); moreover, the beam can be focused to spot sizes with micrometer lateral dimensions ($\sim$ 10 μm $\times$ 5 μm) [70].

Finally, the synchrotron radiation interacts with the sample and the scattered ra-

	^{57}Co (10 mCi)	SMS
Physical principle	Radioactive decay	Pure nuclear reflections
Energy	14.4 keV	
Lineshape	Lorentzian	Squared Lorentzian
FWHM	$\sim$ 0.1 mm/s	$\sim$ 0.3 mm/s [a]
Recoilless factor (f)	$\sim$ 0.784 at 300 K [b]	$\sim$1
Intensity on the sample	$\sim 10^4$ photons/s	$\sim 10^4$ photons/s [a]
Focal spot	$\sim$ 1 cm $\times$ 1 cm	$\sim$ 10 μm $\times$ 5 μm [a]
Geometry	Transmission [c]	Grazing incidence
Polarization	Unpolarized [c]	Polarized

Table 2.1: Comparison between the principal features of a conventional radioactive source used for Mössbauer spectroscopy of the ^{57}Fe nucleus and the Synchrotron Mössbauer Source.
[a] The exact values depend on technical specifications of the beamline during the measurements, in particular the optimization of the relative positions of the optics and monochromators and the current temperature of the iron borate crystal. A compromise between spectral resolution and intensity must be chosen.
[b] The exact value depends on the geometrical specifications of the setup and varies with the age of the source. It must be evaluated at each measurement. Moreover, the value must be corrected (i.e. decreased) for spurious counts.
[c] Different geometries are possible at the expense of intensity.

diation is collected by an avalanche photodiode. The measurements can be realized in grazing incidence geometry, as well as in transmission geometry.

The principal features of SMS are reported in Table 2.1 and compared with those of a conventional radioactive source used for energy-domain Mössbauer spectroscopy. The bandwidth of the radiation and its intensity are comparable between the two sources. However, the radiation coming from the SMS can be greatly focused and the measurements can be easily realized in grazing incidence geometry. These features allow to enhance the sensitivity of Mössbauer spectroscopy with respect to that achieved in a standard Mössbauer setup based on a radioactive source, enabling to study thin layers of molecular materials, otherwise impossible to study with a conventional setup.

2.2 Electron paramagnetic resonance

Electron paramagnetic resonance (EPR) is a spectroscopic technique based on the absorption of electromagnetic radiation, usually in the microwave range, by a paramagnetic system subjected to an external magnetic field. Thanks to its selectivity, EPR spectroscopy allows to identify and characterize the electronic structure of the paramagnetic center in the sample and to obtain information on the surrounding environment and the dynamical processes involving it.

In the first Section, the principles at the base of the technique are presented, while in the second Section the main features of an EPR spectrum are reviewed. The third Section gives an overview of the interactions that are revealed by an EPR spectrum. In the fourth Section, the technical aspects of a standard EPR spectrometer are described, while in the fifth Section a discussion on the investigation of electric field effects by means of EPR spectroscopy is reported.

2.2.1 Principles of the technique

EPR is based on the electron Zeeman interaction, i.e. the interaction between the electron magnetic moment and an external magnetic field.

The main features of EPR can be understood by considering a weakly bound electron with spin $\mathbf{S}$ that is subjected to a magnetic field $\mathbf{B}$ directed along the z axis, coinciding with the electron quantization axis. The electron has a magnetic moment [72]

$$\boldsymbol{\mu} = -g_e \mu_B \mathbf{S} \tag{2.10}$$

where g_e is the g-factor (~ 2.0023 for the free electron) and μ_B is the Bohr magneton. The energy associated with the interaction with the magnetic field is [72]

$$E = -\boldsymbol{\mu} \cdot \mathbf{B}$$

Considering that the electron spin can be in two different states, i.e. it can have two different spin projections along z ($M_S = \pm\frac{1}{2}$), two energy levels are possible: $E = \pm\frac{1}{2} g_e \mu_B B$ (see Fig. 2.8). The splitting between the two spin levels, that are degenerate in absence of an external magnetic field, depends linearly on B and in particular equals $\Delta E = g_e \mu_B B$. Therefore, it is possible to induce transitions between the two energy levels by means of electromagnetic radiation of energy $h\nu$ such that [72]

$$h\nu = g_e \mu_B B \tag{2.11}$$

where ν is the frequency of the radiation. Eq. 2.11 is the resonance condition at the base of EPR spectroscopy. In an EPR spectrometer the frequency of the radiation is fixed and the resonance condition is found by varying slowly the intensity of the magnetic field. For X-band measurements that employ microwave radiation with $\nu = 9.5$ GHz, the resonance field is of the order of 0.3 T.

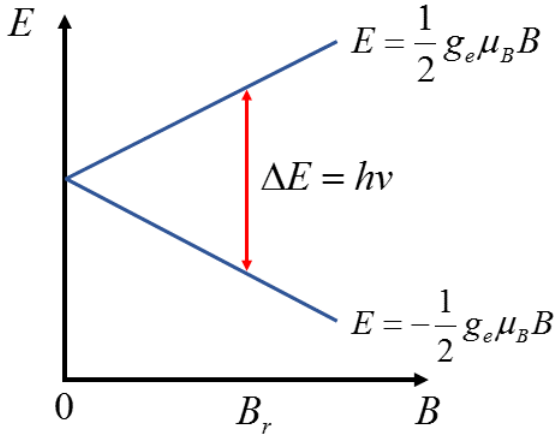

Figure 2.8: Scheme of the energy levels of a weakly interacting electron subjected to an external magnetic field. The transition between the levels is induced by a resonance field B_r.

The selection rules for the allowed transitions depend on the experimental configuration, i.e. on the relative orientation of the microwave magnetic field $\mathbf{B}_1$ with respect to the external magnetic field $\mathbf{B}$. The transition probability between the initial state $|M_S M_I>$ (M_I is the projection of the nuclear spin) and the final state $|M_S^{'} M_I^{'}>$ is in fact proportional to [72]

$$< M_S^{'} M_I^{'} | \hat{H}_1 | M_S M_I > \tag{2.12}$$

where $\hat{H}_1 = -\hat{\boldsymbol{\mu}} \cdot \mathbf{B}_1$ is the spin Hamiltonian operator representing the effect of an applied field $\mathbf{B}_1$ on the system to which a total magnetic-dipole operator $\hat{\boldsymbol{\mu}}$ is associated.

In the standard configuration $\mathbf{B}_1$ is perpendicular to $\mathbf{B}$ (that is considered to be directed along the z axis); if for example $\mathbf{B}_1$ is parallel to the x axis, the general matrix element given by Eq. 2.12 reduces to the evaluation of

$$g_e \mu_B B_1 < M_S^{'} M_I^{'} | \hat{S}_x | M_S M_I >= g_e \mu_B B_1 < M_S^{'} | \hat{S}_x | M_S >< M_I^{'} | M_I > \tag{2.13}$$

where $\hat{S}_x$ is the projection of the spin operator along x. The matrix element of $\hat{S}_x$ is different from zero only if $M_S^{'} = M_S \pm 1$ and $M_I^{'} = M_I$. Therefore, the selection rules associated with $\mathbf{B}_1 \perp \mathbf{B}$ are

$$\Delta M_S = \pm 1 \qquad \text{and} \qquad \Delta M_I = 0$$

In the parallel configuration ($\mathbf{B}_1 \parallel \mathbf{B}$) the matrix element given by Eq. 2.12 must be evaluated by taking into account the $\hat{S}_z$ operator

$$g_e \mu_B B_1 < M_S^{'} | \hat{S}_z | M_S >< M_I^{'} | M_I >= g_e \mu_B B_1 M_S < M_S^{'} | M_S >< M_I^{'} | M_I > \tag{2.14}$$

This matrix element is different from zero only if $M_S^{'} = M_S$ and $M_I^{'} = M_I$. Therefore, in this case the selection rules are

$$\Delta M_S = 0 \qquad \text{and} \qquad \Delta M_I = 0$$

implying that no absorption is expected in this configuration. However, in real systems, depending on the Hamiltonian describing them, the quantization axis may not coincide with the z axis, implying that M_S is not a good quantum number anymore. The eigenfunctions of the system are then combinations of different M_S states and consequently the $\hat{S}_z$ operator may promote transitions. Therefore, transitions that are forbidden in the standard configuration can give appreciable EPR lines with $\mathbf{B}_1 \parallel \mathbf{B}$ [72, 19, 17].

EPR spectroscopy is applicable to systems in a paramagnetic state, i.e. a state having net angular momentum. Typical systems that can be studied are free radicals in the solid, liquid or gaseous phase, transitions ions, various 'point' defects in solids and systems with more than one unpaired electron, such as triplet-state systems, biradicals and multiradicals [72]. Moreover, EPR spectroscopy can be applied to the study of ferromagnets, single molecule magnets and single chain magnets.

2.2.2 EPR spectrum

In a real experiment an ensemble of spins has to be considered. If $B = 0$, half of the spins will be in the energy level corresponding to $S_z = \frac{1}{2}$ and half of them in that one corresponding to $S_z = -\frac{1}{2}$. If $B \neq 0$, the spins will redistribute on the two energy levels according to a Boltzmann distribution law. The ratio between the number of spins in the two states is [73]

$$\frac{N_{1/2}}{N_{-1/2}} = e^{-\left(\frac{g_e|\mu_B|B}{k_B T}\right)} \tag{2.15}$$

where k_B is the Boltzmann constant and T is the absolute temperature of the lattice.

At room temperature and for magnetic fields of the order of 0.3 T, Eq. 2.15 can be approximated with [73]

$$\frac{N_{1/2}}{N_{-1/2}} = 1 - \frac{g_e|\mu_B|B}{k_B T} \tag{2.16}$$

Eq. 2.16 shows that at $T = 300$ K and $B = 0.3$ T there is an excess of spins in the low energy state over those in the high energy state of the order of 1/1000. This small excess allows the microwave absorption by the low energy state to overcome the emission from the high energy one and therefore it makes possible the observation of an EPR absorption signal.

It is worth noting that the interaction of the spin system with the lattice is needed to restore the thermal equilibrium, i.e. the excess spins in the low energy level [73]. If the spin system were not coupled with the lattice, the microwave field acting continuously

on the system would eventually equalize the populations in the two energy levels. This condition is called saturation and implies that no EPR signal can be detected. The interaction between the spin system and the lattice is described by a characteristic time called spin-lattice relaxation time T_1.

In real macroscopic systems it is convenient to consider the total magnetization $\mathbf{M}$, that is a vector resulting from the sum of all the magnetic moments of the individual electron spins. The relaxation of $\mathbf{M}$ is associated to two different mechanisms [73]: the spin-lattice and the spin-spin interactions. The first interaction tends to restore the value of the z component of $\mathbf{M}$ to its equilibrium value whenever it deviates from it, while the second interaction tends to make the x and y components of $\mathbf{M}$ zero. Moreover, the spin-lattice relaxation takes into account a dissipation of energy within the lattice as phonons, while the second interaction is based on an energy exchange between the spins. The two interactions are described by two different relaxation times, T_1 and T_2, respectively. The evolution of the magnetization in a magnetic field $\mathbf{B}$ as a function of time is described by the Bloch equations, for which steady-state solutions can be found [72].

The EPR signal is proportional to the component of the magnetization measured perpendicular to B_1 [72]

$$M_y = \chi_0 \frac{\omega_0 T_2 B_1}{1 + (\omega - \omega_0)^2 T_2^2} \tag{2.17}$$

where χ_0 is the static magnetic susceptibility, ω is the frequency of the microwave field B_1 and ω_0 is the resonance frequency.

Eq. 2.17 shows that the EPR signal is a Lorentzian function with FWHM $= 2/T_2$. However, the investigated samples consist of differently oriented species or species having different interactions with their surrounding. Consequently, the EPR line is the superposition of many lines and its width can be much broader than that expected from T_2. In particular, the spectral lines can be homogeneously or inhomogeneously broadened [72]. When the spins see the same net magnetic field and have the same spin Hamiltonian parameters, a homogeneous broadening is encountered and the lineshape is Lorentzian. On the contrary a inhomogeneous broadening is encountered when the spins are not subjected to the same value of the magnetic field. In this case the EPR signal has a Gaussian shape.

2.2.3 Interactions revealed

An EPR experiment records the response of a paramagnetic sample in an external magnetic field to the microwave irradiation. Therefore, in order to interpret the spectrum, all the relevant interactions taking place between the paramagnet and the external field, as well as the internal one, have to be considered. For a given unpaired electron, the symmetry properties of the surrounding, as well as the interaction with other electrons and with magnetic nuclei, are responsible for the peculiar features of the spectrum. Each interaction can be represented using a different term in the spin Hamiltonian [74].

The Zeeman interaction between an electronic system described by a spin $\mathbf{S}$ and an external magnetic field $\mathbf{B}$ is represented by [74]

$$H_{Ze} = \mu_B \mathbf{B} \cdot \mathbf{g} \cdot \mathbf{S} \tag{2.18}$$

where $\mathbf{g}$ is a second rank tensor that can be diagonalized in the principal axis system. If the system has cubic symmetry, $\mathbf{g}$ is isotropic: $g_{xx} = g_{yy} = g_{zz} = g$. If the system has uniaxial symmetry, $\mathbf{g}$ is anisotropic and in particular

$$\mathbf{g} = \begin{pmatrix} g_\perp & 0 & 0 \\ 0 & g_\perp & 0 \\ 0 & 0 & g_\parallel \end{pmatrix}$$

The g-factor of the system, which defines the resonance condition, is then given by $g = \sqrt{g_\perp^2 \sin^2\theta + g_\parallel^2 \cos^2\theta}$, where θ is the angle between $\mathbf{B}$ and the symmetry axis. If the system has rhombic symmetry, $\mathbf{g}$ is anisotropic and $g_{xx} \neq g_{yy} \neq g_{zz}$.

It is worth noting that in general the value of the g-factor is different from the value associated with the free electron (g_e). The reason relies on spin-orbit coupling that, for a molecule having a ground state with zero orbital angular momentum, admixes it with certain excited states and causes a small amount of orbital angular momentum to appear in the actual ground state. The result is a local magnetic field that adds vectorially to the external one and consequently changes the value of the g-factor with respect to that of the free electron [72]. The g-tensor gives information on the chemical environment experienced by the unpaired electron, its symmetry and electronic structure.

The Zeeman interaction between a nucleus with nuclear spin $\mathbf{I}_N$ and the external magnetic field is described by a Hamiltonian having an expression similar to Eq. 2.18 [74]

$$H_{Zn} = \mu_N \mathbf{B} \cdot g_N \mathbf{I}_N$$

where μ_N is the nuclear Bohr magneton. Since $\mu_N = \left(\frac{1}{1836}\right)\mu_B$, this term is usually neglected when considering the complete spin Hamiltonian of the system in continuous wave EPR.

When the system has more than one unpaired electron, the mutual interaction between them is considered by a spin Hamiltonian term [74]

$$H_{ZFS} = \mathbf{S} \cdot \mathbf{D} \cdot \mathbf{S}$$

where $\mathbf{D}$ is a symmetric traceless second rank tensor, called zero field splitting. This term is different from zero only when $S > 1/2$ and in symmetries lower than the cubic one. Its effect is the splitting of the energy levels in absence of an external magnetic field, as already noted in the description of single molecule magnets (Section 1.1.3.1). If the coordinate axes x, y and z are chosen parallel to the eigenvectors of $\mathbf{D}$, then $\mathbf{D}$ is diagonal and, by defining $D = D_{zz} - \frac{1}{2}(D_{xx} + D_{yy})$ and $E = \frac{1}{2}(D_{xx} - D_{yy})$ with $0 \leq |\frac{E}{D}| \leq \frac{1}{3}$, H_{ZFS} can be rewritten as [3]

$$H_{ZFS} = D\left[S_z^2 - \frac{1}{3}S\left(S+1\right)\right] + E\left(S_x^2 - S_y^2\right)$$

This expression is simplified depending on the symmetry of the system. The axial anisotropy (D) is zero in cubic symmetry, while the transverse (or rhombic) one (E) is zero in axial symmetry.

The interaction between an unpaired electron and the surrounding nuclei is called hyperfine interaction and is described by [74]

$$H_{Hyp} = \sum_i \mathbf{S} \cdot \mathbf{A}_i \cdot \mathbf{I}_{Ni}$$

where $\mathbf{A}_i$ is the symmetric hyperfine matrix of the i-th nucleus and the sum is over all the interacting nuclei.

In general, all the cited terms can contribute to the complete spin Hamiltonian of the system. However, its exact form depends on the properties of the paramagnetic center. Moreover, if the paramagnetic centers in the sample can interact, the spin Hamiltonian of the whole system has to include dipolar and exchange interactions terms between the corresponding spins [72].

It is instructive to see how the anisotropy of the g-factor and the zero field splitting term have a common origin, that is the spin-orbit interaction. This can be shown by means of an exact derivation of the H_{Ze} and H_{ZFS} terms. This derivation holds in the hypothesis that the crystal field energy exceeds the spin-orbit coupling energy, that is tipically true for ions of the first transition series. Therefore the energy levels of these systems are determined by the crystal field, while the spin-orbit interaction can be treated as a weak perturbation. Moreover, to a first approximation the total electronic orbital ($\mathbf{L}$) and spin ($\mathbf{S}$) angular momenta can be considered separately. The first thing to note is that, when dealing with electrons in a molecule, the total magnetic moment is the sum of the contributions from the spin and orbital angular momenta. Therefore Eq. 2.10 becomes [72]

$$\boldsymbol{\mu} = -\mu_B\left(\mathbf{L} + g_e\mathbf{S}\right)$$

where $\mathbf{L}$ is the total electronic orbital angular momentum of the considered atom or ion in the ground state configuration. Consequently, the system can be described by an Hamiltonian [72]

$$H = \mu_B\mathbf{B} \cdot (\mathbf{L} + g_e\mathbf{S}) + \lambda\mathbf{L} \cdot \mathbf{S} \tag{2.19}$$

that is the sum of an electronic Zeeman term and a spin-orbit interaction term (λ is the spin-orbit coupling constant).

Assuming an orbitally non degenerate ground state $|GM_S>$, the second-order correction to each element in the Hamiltonian matrix is given by [72]

$$(H)_{M_S,M_S'} = -\sum_{n\neq G} \frac{|< GM_S|\,(\mu_B \mathbf{B} + \lambda \mathbf{S})\cdot \mathbf{L} + g_e \mu_B \mathbf{B}\cdot \mathbf{S}|nM_S' >|^2}{U_n^0 - U_G^0} \tag{2.20}$$

where the sum runs over all orbital states and the superscripts 0 indicate the zeroth-order energies. By defining a matrix [72]

$$\boldsymbol{\Lambda} = -\sum_{n\neq G} \frac{< G|\mathbf{L}|n >< n|\mathbf{L}|G >}{U_n^0 - U_G^0}$$

Eq. 2.20 can be written as [72]

$$(H)_{M_S,M_S'} =< M_S|\mu_B^2 \mathbf{B}\cdot\boldsymbol{\Lambda}\cdot\mathbf{B} + 2\lambda\mu_B \mathbf{B}\cdot\boldsymbol{\Lambda}\cdot\mathbf{S} + \lambda^2 \mathbf{S}\cdot\boldsymbol{\Lambda}\cdot\mathbf{S}|M_S' > \tag{2.21}$$

The first term in Eq. 2.21 represents a constant contribution to the energy of all spin states and can be discarded. The second and third terms in Eq. 2.21 constitute an Hamiltonian that operates only on spin variables and, combining them with the operator $g_e\mu_B\mathbf{B}\cdot\mathbf{S}$ of Eq. 2.19, the Hamiltonian of the system can be written as [72]

$$H = \mu_B \mathbf{B}\cdot(g_e\mathbf{I} + 2\lambda\boldsymbol{\Lambda})\cdot\mathbf{S} + \lambda^2\mathbf{S}\cdot\boldsymbol{\Lambda}\cdot\mathbf{S} = \mu_B\mathbf{B}\cdot\mathbf{g}\cdot\mathbf{S} + \mathbf{S}\cdot\mathbf{D}\cdot\mathbf{S}$$

where is $\mathbf{I}$ the identity matrix. It is straightforward that

$$\mathbf{g} = g_e\mathbf{I} + 2\lambda\boldsymbol{\Lambda} \tag{2.22}$$

and

$$\mathbf{D} = \lambda^2\boldsymbol{\Lambda} \tag{2.23}$$

Therefore, Eq. 2.22 shows that the anisotropy of the g-factor is due to the spin-orbit interaction and the value of the anisotropy is higher the higher is the spin-orbit coupling and the smaller is the energy difference between the excited and ground states. Moreover, also the zero field splitting tensor depends on the spin-orbit coupling constant. Both $\mathbf{g}$ and $\mathbf{D}$ reflect the effect of the magnetic anisotropy of the material. However, while the anisotropy associated to $\mathbf{g}$ says how a material responds to an external magnetic field and perhaps the feasibility to magnetize it in a direction rather than in an other one, the anisotropy associated to $\mathbf{D}$ expresses an intrinsic property of the material, i.e. the preferential direction for the magnetization.

It can be useful to calculate the value of the zero field splitting parameter for the molecular cluster constituted by a ring of N ions having spin $s = 5/2$ (already presented in Section 1.1). For this purpose the giant spin $S = Ns$ (and the corresponding giant spin Hamiltonian) is assumed as a proper way in order to describe the magnetic properties of the system when there is a ferromagnetic coupling between the spins [16].

Moreover, assuming that the local anisotropies be axial and can be parametrized by an axial parameter D_i defined as [16]

$$H = D_i \left[s_z^2 - \frac{1}{3} s\left(s+1\right) \right]$$

with all local axes parallel to each other, the axial parameter within the $S = Ns$ state is given by [16]

$$D = \sum_i d_i D_i \tag{2.24}$$

where d_i is obtained by projecting the local spin s on the total spin S [75]. Consequently, for the $S = Ns$ state Eq. 2.24 becomes [16]

$$D = \frac{2s-1}{2Ns-1} D_i = \frac{2s-1}{2S-1} D_i \tag{2.25}$$

Therefore, Eq. 2.25 shows that the magnetic anisotropy barrier to be overcome for the reorientation of the magnetization of the cluster, that is given by $-DS^2$ (see Eq. 1.10), increases only linearly with S [76]. The same trend is encountered in magnetic nanoparticles: the energy barrier for the reorientation of the magnetization is KV (see Eq. 1.5), therefore it is proportional to the volume and thus in first approximation to the giant magnetic moment of the nanoparticle. This example shows the principal difference in the approaches used to describe molecular nanomagnets and magnetic nanoparticles: while the anisotropy energy density K refers to the bulk system, D_i relies on the single ion constituting the molecular cluster [16]. Therefore, the ability of the bottom-up approach to describe the structural as well as the magnetic parameters of the cluster is evidenced.

The equations developed for the ring system allow to calculate the EPR spectra of the ground state $S = Ns$. In the strong field limit, i.e. if the resonance field for the free electron (B_0) is much larger than the zero field splitting, the resonance field for the $M_S = -Ns$ to $M_S^{'} = -Ns + 1$ is given by [16]

$$B_{-Ns} = \frac{\left(3\cos^2\theta - 1\right)\left(2s-1\right) D_i}{2 g_e \mu_B} + B_0 \tag{2.26}$$

where θ is the angle between the direction of the applied magnetic field and the anisotropy axis. Eq. 2.26 shows that the resonance at the lowest and highest field is independent of N, implying that the spread of the spectrum is independent of the number of coupled spins. This result applies to any ferromagnetic cluster, provided the local anisotropy axes are parallel to each other [16]. Furthermore, with increasing N the resulting EPR spectra tend to lose the fine structure, merging into a continuum of indistinguishable transitions, as expected when passing from a nanoscopic to a macroscopic material. This effect is shown by the calculated intensity of the parallel transitions ($\theta = 0$) at infinite temperature for different values of N [16], that is reported in Fig. 2.9.

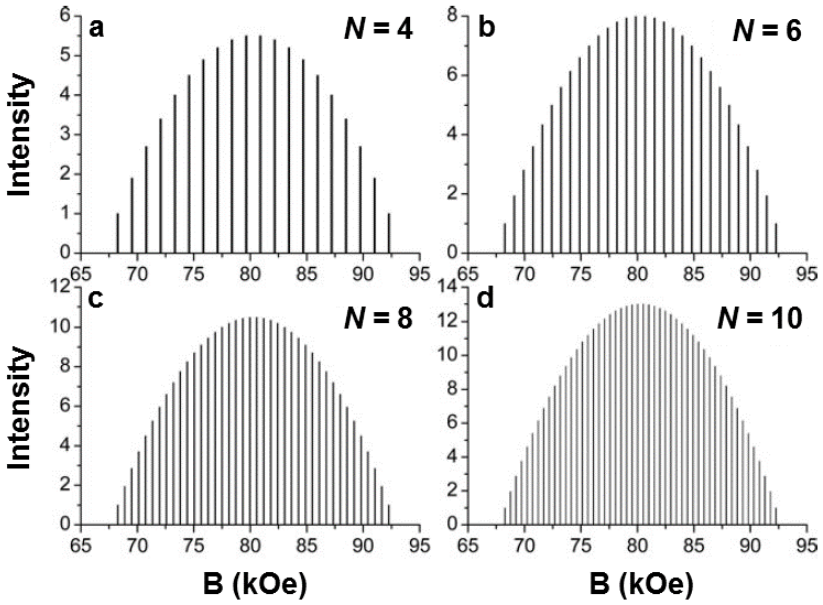

Figure 2.9: Calculated intensity of the parallel EPR transitions at infinite temperature for an increasing number (N) of ferromagnetically coupled $s = 5/2$ spins. The value of D_i is 0.28 cm^{-1}. Image taken from [16].

Finally, from Eq. 2.26 the resonance field for the generic $M_S \rightarrow M_S + 1$ transition can be written as [16]

$$B_{M_S} = \frac{(3\cos^2\theta - 1)\,(2M_S + 1)\,D}{2g_e\mu_B} \tag{2.27}$$

This formula applies to the interpretation of the EPR spectra of single molecule magnets and magnetic nanoparticles in the strong field limit. However, it is worth noting that, despite this condition be respected, the observation of the fine structure of the spectra may be hidden when dealing with powder spectra, where all possible orientations of the anisotropy axis are present. On the contrary single crystal EPR spectra allow a more direct extrapolation of the parameters characterizing the spectrum and investigation of their angular dependence.

2.2.4 EPR spectrometer

The main components of an EPR spectrometer are the source, the resonator, the magnet and the detector (Fig. 2.10). The source and the detector are usually hold in the same system, called microwave bridge.

The source is an oscillator, usually a solid-state device, that produces microwave radiation with fixed frequency and defined power. The most used microwave frequency

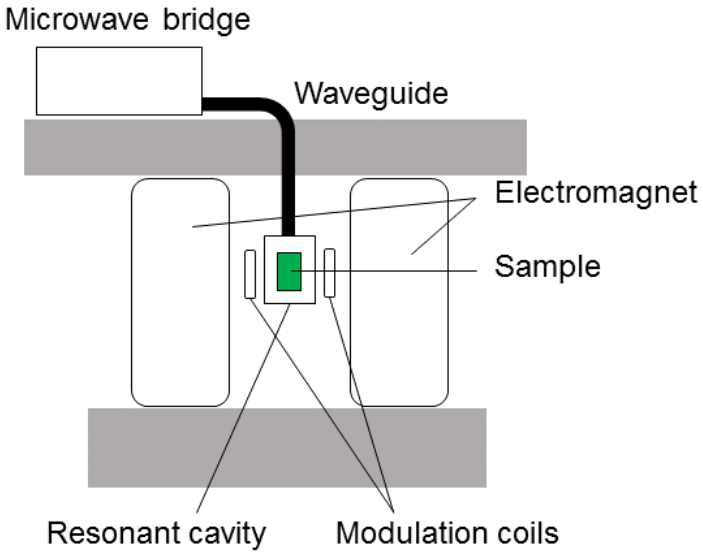

Figure 2.10: Scheme of an EPR spectrometer. The microwave bridge holds the microwave source and the detector.

in EPR experiments is $\nu = 9.5$ GHz, the so-called X-band; this frequency corresponds to a wavelength of about 32 mm. Other common bands are Q-band ($\nu = 36$ GHz) and W-band ($\nu = 95$ GHz). Moreover, the microwave power incident on the sample can be continuous (cw) or pulsed.

By means of a waveguide the microwaves reach the resonator, that is a resonant cavity hosting the sample under study. The cavity is designed so that standing waves are formed inside it. These waves are characterized by the fact that the maxima of the corresponding electric field E_1 and magnetic field B_1 occur in different places. The sample is placed at a maximum of B_1 (corresponding to a minimum of E_1). A small hole, called iris, in the cavity wall allows the coupling of the microwaves into and out of the cavity: the adjustment of the iris allows an optimal impedance matching. In the condition of critical coupling no microwave is reflected by the cavity and all the energy is stored inside it. At resonance, an EPR transition is induced and part of the energy is absorbed by the sample. Consequently, the condition of critical coupling is lost and part of the microwaves are reflected from the cavity and revealed by a detector, therefore giving the EPR signal.

The resonance condition is obtained by varying the intensity of an external magnetic field. The field sweep is determined by the frequency of the microwaves and the properties of the sample. For X-band measurements intensities of the order of few T are needed, that are usually produced by an electromagnet. The stability and uniformity of the field over the sample volume is a fundamental property to resolve narrow EPR lines and obtain the correct lineshape.

In order to improve the signal to noise ratio of the measurements, the phase-sensitive

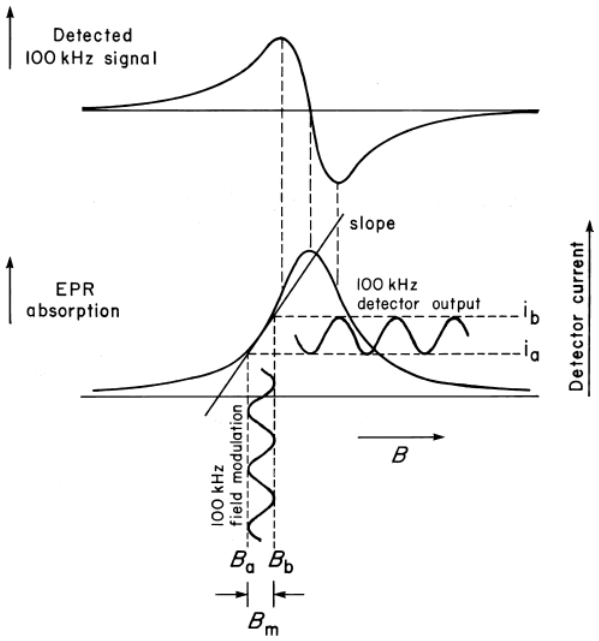

Figure 2.11: Schematic representation of the effect of field modulation on the EPR absorption signal. Image taken from [72].

detection technique is used. This technique is based on field modulation: a small-amplitude sinusoidal magnetic field is superimposed on the external magnetic field. This oscillating field (usually at a frequency of 100 kHz) is achieved by means of small Helmholtz coils placed on each side of the cavity. The effect of field modulation is that the resonance condition, obtained when the main magnetic field is at resonance, is modulated and consequently the detected signal is also modulated. For this reason the EPR signal is the derivative of the absorption signal [72] (see Fig. 2.11).

In a typical X-band EPR spectrometer a minimum number of 10^{10} spins/G can be revealed [77]. Considering a sample volume and density of 0.4 mm^3 and 10^{20} atoms/mm^3, respectively, the minimum fraction of paramagnetic species that can be revealed is of the order of 10^{-10} for an EPR linewidth of 1 G.

The use of frequencies and fields higher than those used in X-band brings various advantages [78, 79, 80]: increased resolution, increased sensitivity (for example, in W-band a minimum number of 10^7 spins/G can be revealed [77]), simplification of the spectra and of their assignment, observation of the spectra in EPR "silent" species and determination of the sign of the zero field splitting (ZFS) anisotropy. The use of high frequencies is particularly useful for the study of molecular nanomagnets, where large spin and ZFS are often observed. For example, the nature of the ground $S = 10$ state of the first discovered SMM (Mn12ac) was detected and its ZFS parameters measured for the first time by high field EPR with frequency up to 525 GHz and magnetic field

of the order of 25 T [81, 82, 83].

Finally, it is worth citing pulsed EPR spectroscopy. With this technique the sample is irradiated by microwave pulses instead of a continuous irradiation. Different pulse sequences can be used depending on the nature and magnitude of the interaction to be studied [84]. The application of pulsed EPR to molecular nanomagnets is useful in view of their application for quantum computing [40, 85, 86]. Important information on the excited level structure, as well as the knowledge of the decoherence time of large molecular clusters at low temperature can be investigated [16].

2.2.5 EPR under an electric field

The investigation of electric fields effects by means of EPR spectroscopy dates back to the '60s, when it was used to study the symmetry of transition metal centers in insulators or organic materials, as proteins and enzymes [87]. An applied electric field in fact may induce linear shifts in the paramagnetic resonance line spectrum when paramagnetic ions occupy sites which lack inversion symmetry [88, 89]. This effect was first observed for transition metal impurities in silicon by taking the spectrum with and without a dc field of 10 kV/cm applied to the sample [90]. However, the electric-field-induced shifts are small and in general high field intensities ($>$ 100 kV/cm) were needed to observe them [91]. Moreover, for samples not obtainable as single crystal, the electric-field-induced lineshifts had to be detected on an overall linewidth of several hundreds Gauss [92]. The problem of measuring the shifts for an inhomogeneously broadened line were overcome by using a method based on the observation of electron spin echoes in pulsed EPR [93, 91]. The electric field was applied in the form of a voltage step occurring during the cycle of events, which characterize an electron - spin echo process [93].

More recently the application of an electric field during pulsed EPR was used to study the manipulation of spin states by means of electric fields [94, 95]. This achievement is a necessary step towards quantum information processing. EPR is in fact the standard technique to manipulate spins via a magnetic field. However, tipically quantum manipulation has to be performed on very short temporal and spatial timescales, of the order of 1 ns and 1 nm, respectively [96]. In order to achieve the temporal resolution, the oscillating magnetic field should be of the order of 10^{-2} T, which is difficult to achieve [96]. Also the spatial resolution, required for addressing a single molecule, is prohibitively small [96]. For this reason manipulating the spins via an electric field would be preferable, because strong fields can be applied to small regions more easily, thus allowing for fast switching and spatially confined spin control. Considering that the electric field does not couple directly to the electronic spin, only systems where an indirect coupling is possible can be investigated.

Finally, an other method to detect small shifts in EPR spectra induced by an electric field relies on continuous EPR spectroscopy using electric field modulation and lock-in detection. Few examples of application of this method exists. This technique was applied to investigate the electric field effect on the non-Kramers ion Pr^{3+} in $LaMgN_2$ [97]. It was also used to study the magnetoelectric coupling in single crystal Cu_2OSeO_3

[98]: the modulation by electric field leads to a modulation of the internal magnetic field in the sample and therefore a change in the features of the EPR spectra with respect to those acquired without the electric field, evidencing the presence of the magnetoelectric effect.

Chapter 3

Mössbauer spectroscopy of a monolayer of single molecule magnets

The use of single molecule magnets (SMMs) as cornerstone elements in spintronics and quantum computing applications demands that magnetic bistability is retained when molecules are interfaced with solid conducting surfaces. Synchrotron Mössbauer spectroscopy was employed to investigate a monolayer of the tetrairon(III) (Fe_4) SMM chemically grafted on a gold substrate. At low temperature and zero magnetic field, the magnetic pattern of the Fe_4 molecule was observed, indicating slow spin fluctuations compared to the Mössbauer timescale. Significant structural deformations of the magnetic core, induced by the interaction with the substrate, as predicted by *ab initio* molecular dynamics calculations, were also observed. However, the effects of the modifications occurring at the individual iron sites partially compensate each other, so that slow magnetic relaxation is retained on the surface. Interestingly, these deformations escaped detection by conventional synchrotron-based techniques, like X-ray magnetic circular dichroism, thus highlighting the power of synchrotron Mössbauer spectroscopy for the investigation of hybrid interfaces.

This study has been published:
"Synchrotron Mössbauer spectroscopy on a monolayer of single molecule magnets unveils the effects of molecule-surface interactions"
A. Cini, M. Mannini, F. Totti, M. Fittipaldi, G. Spina, A. Chumakov, R. Rüffer, A. Cornia and R. Sessoli, *Nat. Commun.* **9**(1), 480 (2018)
DOI: 10.1038/s41467-018-02840-w

3.1 Introduction

Single molecule magnets (SMMs) are a very appealing class of nanomagnetic objects with potential application for spintronics [7, 8, 9] and quantum computing [10, 11, 12]. As explained in Section 1.1.3.1, their properties depend on the combination of a large molecular spin and an easy-axis magnetic anisotropy, which results in a double well energy potential, that opposes to the reversal of the magnetization [3].

Organization of these molecules on surfaces was the focus of considerable effort as a prerequisite to single molecule addressing [99, 100, 101]. In such studies, it was demonstrated that magnetic bistability persists and can even be enhanced on a surface [102, 103]. Especially efficient in boosting the memory effect of both molecules [104] and individual atoms [105] is deposition on thin insulating layers (e.g., MgO) rather than directly on the metal surface. Despite these remarkable results, the factors controlling magnetic bistability on surfaces remain still unclear. This is in part due to the limited number of experimental techniques that are sensitive enough to detect the magnetic properties of a monolayer (or less) of magnetic molecules. Most investigations rely on the use of X-ray absorption and magnetic circular dichroism (XMCD) [106] with synchrotron radiation, which has exceptional surface sensitivity and selectivity to the magnetism of the probed elements. In silico methods can also be of considerable aid in predicting the fine evolution of geometrical and magnetic structure of SMMs on a surface [107].

In such a framework, Mössbauer spectroscopy, beyond having an outstanding sensitivity to the coordination environment of the probed atom, is able to investigate the spin dynamics over timescales (1 - 1000 ns) much shorter than those accessible by XMCD. The technique was previously adopted to study the relaxation behavior of many SMM materials containing ^{57}Fe as Mössbauer active nucleus [108, 109]. However, the standard use of radioactive sources limits the application domain of Mössbauer spectroscopy to bulk samples [66]. This limitation was overcome by the use of time-domain nuclear resonant scattering of synchrotron radiation at grazing angle: an example was the study of monolayers of metallic ^{57}Fe grown on W(100) or embedded in layered systems [110, 111, 112]. However, with this technique complex spectra are expected for samples containing inequivalent iron sites and characterized by several electronic levels. Moreover, the radiation intensity customarily used in time-domain spectroscopy may damage molecular or biological compounds.

These limitations were overcome by taking advantage of the Synchrotron Mössbauer Source (SMS), that allows to obtain energy-domain spectra. Synchrotron Mössbauer spectroscopy was used to probe the magnetism of a monolayer of Fe_4 SMMs tethered to a polycrystalline gold substrate, providing an unprecedentedly detailed picture of molecule-surface interaction effects on structural, electronic and magnetic properties of the adsorbed SMMs.

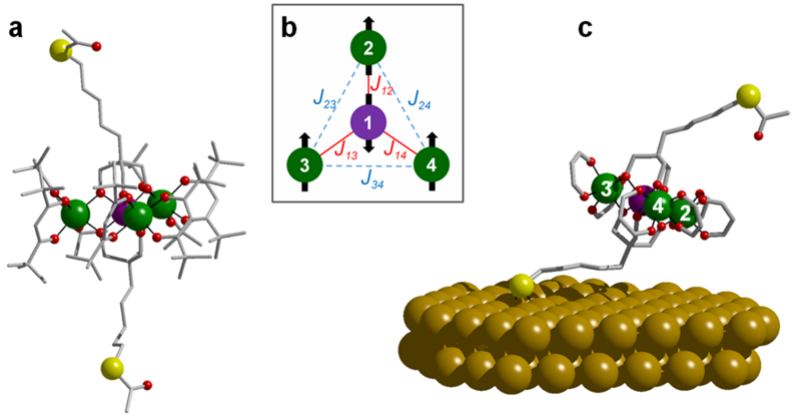

Figure 3.1: a) Structure of the Fe_4 SMM in the crystalline phase (color code: Fe atoms in green and violet, O in red, S in yellow, C as pale gray sticks, H atoms omitted for clarity); b) Scheme of the magnetic core, where the dominating antiferromagnetic interactions (in red) lead to an $S = 5$ ground state; c) View of the structure of the Fe_4 SMM tethered to Au(111) through the deprotected thioacetyl termination, as obtained by *ab initio* molecular dynamics calculations [113] (H atoms and tert-butyl groups on dpm– ligands have been omitted for clarity).

3.2 Tetrairon(III)

The object of this study was a monolayer of tetrairon(III) (Fe_4) SMMs tethered to a polycrystalline gold substrate.

The Fe_4 molecule is constituted by four Fe(III) ions that occupy the center and the vertexes of an approximately equilateral triangle (see Fig. 3.1). Thanks to an antiferromagnetic coupling between the spin of the central ion and the spins of the peripheral ones (each Fe(III) has a spin $s = 5/2$), the ground state of the molecule has a total spin $S = 5$. The first excited states are two $S = 4$ manifolds, which lie about 60 K higher in energy and are degenerate in case of perfect three-fold symmetry. The molecule shows a moderate easy-axis magnetic anisotropy, directed perpendicular to the plane of the four Fe(III) ions, that is responsible for the double well energy potential characterizing the SMMs. From Eq. 1.10 its height, that corresponds to the energetic barrier for the reversal of the magnetization, can be calculated to be about 15 K.

Fe_4 has a propeller-like molecular structure that is sufficiently robust to withstand chemisorption on surfaces, processing by thermal sublimation [114] and the construction of single-molecule devices [115]. Indeed, Fe_4 complexes were the first SMMs to show magnetic hysteresis when deposited as a monolayer on a gold surface [102, 114]. These results were obtained by means of X-ray absorption spectroscopy (XAS) and X-ray magnetic circular dichroism (XMCD) synchrotron-based techniques. Mössbauer spectroscopy, having the ability to investigate spin dynamics with timescales much shorter

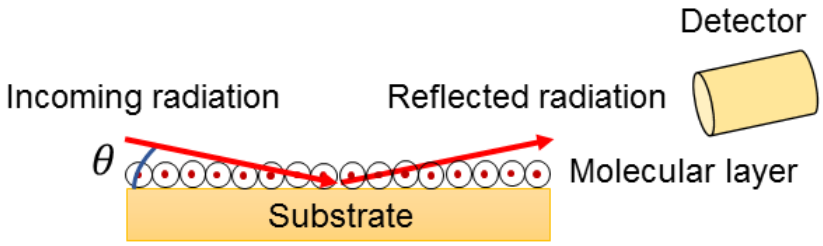

Figure 3.2: Schematic representation of the grazing incidence geometry used in the Mössbauer measurements.

with respect to those accessible by XMCD and the possibility to address the properties of the single Fe(III) ions, can study more deeply the properties of the deposited molecules.

For this reason a Au-supported self-assembled monolayer of the same Fe_4 derivative previously employed in XMCD investigations [116] was studied. Its complete formula is $[Fe_4(L)_2(dpm)_6]$, where Hdpm is dipivaloylmethane and H_3L is 7-(acetylthio)-2,2-bis(hydroxymethyl)heptan-1-ol, a thioacetyl-functionalized tripodal ligand that promotes chemisorption on gold substrates. The compound was characterized elsewhere [116] and was here prepared as a 95 % ^{57}Fe-enriched sample. A monolayer deposit was obtained by chemisorption using a wet chemistry protocol that guarantees the formation of a dense monolayer with no physisorbed material [117]. As a bulk-phase reference, a dropcast sample of the same compound, with an inhomogeneous thickness of about (100 ± 50) nm, was prepared.

The static and dynamic magnetic parameters of Fe_4 molecules in the bulk phase have been determined by magnetometry, high field EPR [118] and standard Mössbauer spectroscopy [108, 109].

3.3 Mössbauer measurements

Energy-domain Mössbauer spectra of both monolayer and dropcast Fe_4 samples were acquired by taking advantage of the Synchrotron Mössbauer Source (SMS). As previously stated in section 2.1.5, the synchrotron light coming out from the monochromators is filtered into an ^{57}Fe-resonant narrow single line. Moreover, the radiation generated by the SMS can be focused to spot sizes of micrometric lateral dimensions and working in grazing incidence geometry is possible. These features allow to achieve the necessary sensitivity to investigate ultra-thin films.

Mössbauer spectra were recorded by collecting the scattered radiation resulting from the reflection on the sample surface at a grazing incidence (see Fig. 3.2). Due to the structure of our samples (low-Z film on a high-Z substrate, Z being the atomic number), the grazing incidence reflection occurs from the surface of the substrate and the molecular layer produces absorption lines. In the case of small grazing angles, the

spectra can be treated as those obtained in a standard setup in transmission geometry, provided that the effective thickness of the samples is multiplied by a factor $2/\sin\theta$, where θ is the grazing angle between the surface of the sample and the direction of the incoming radiation. After measuring the reflectivity of the samples as a function of θ, an incidence angle $\theta \sim 0.1°$ was chosen for both samples. This experimental condition provided a 1100-fold amplification factor, enabling to increase by two orders of magnitude the sensitivity of synchrotron Mössbauer spectroscopy with respect to that achieved with traditional Mössbauer spectroscopy based on a radioactive source.

Mössbauer spectra of the dropcast and monolayer samples were recorded in the temperature ranges 2.2 - 40 K and 2.2 - 11 K, respectively, and are reported in Fig. 3.3.

At the lowest explored temperature, the spectrum of the dropcast sample exhibits a six-line pattern, as expected for a ^{57}Fe-containing sample experiencing slow spin fluctuations compared to the Mössbauer timescale. However, the lines towards the extremes of the spectrum are further split, indicating that inequivalent iron sites are present in the structure; this is in line with previous reports on standard Mössbauer characterization of unfunctionalized Fe_4 clusters in the bulk phase [109]. With increasing temperature, distortions of the spectrum become evident. Increased thermal fluctuations and the population of excited spin levels cause a progressive collapse of the spectrum into a single central structure at 40 K.

The monolayer's spectra are qualitatively similar, though about two orders of magnitude less intense, in agreement with the reduced number of $^{57}Fe_4$ molecules probed by the radiation.

3.4 Fitting of the spectra

The fitting of Mössbauer spectra required the determination of the absorption cross-section of the samples. In general, the total cross-section is the superposition of a number of contributions equal to the number of inequivalent Fe sites; however, symmetry considerations can reduce the number of distinct contributions and consequently change their relative intensities.

Each contribution was evaluated as described in earlier studies of Mössbauer bulk-phase experiments [108, 109]. In particular, the hyperfine Hamiltonians acting on the inequivalent iron nuclear sites are characterized by different static components (i.e., magnetic fields, electric quadrupole tensors and isomer shifts), but share the same dynamical parameters, which reflect the interaction of the molecular total spin states with the thermal bath. When the molecular spin undergoes transitions between its states, the spins at the individual iron ions change their z-components simultaneously; consequently, the iron nuclei are subjected to stochastic changes in the hyperfine field magnitude, though the ratios between the hyperfine fields at the different iron sites remain unchanged.

In order to take into account the dependence of the Mössbauer spectra on the sample effective thickness, the resulting total cross-section of the sample was inserted into

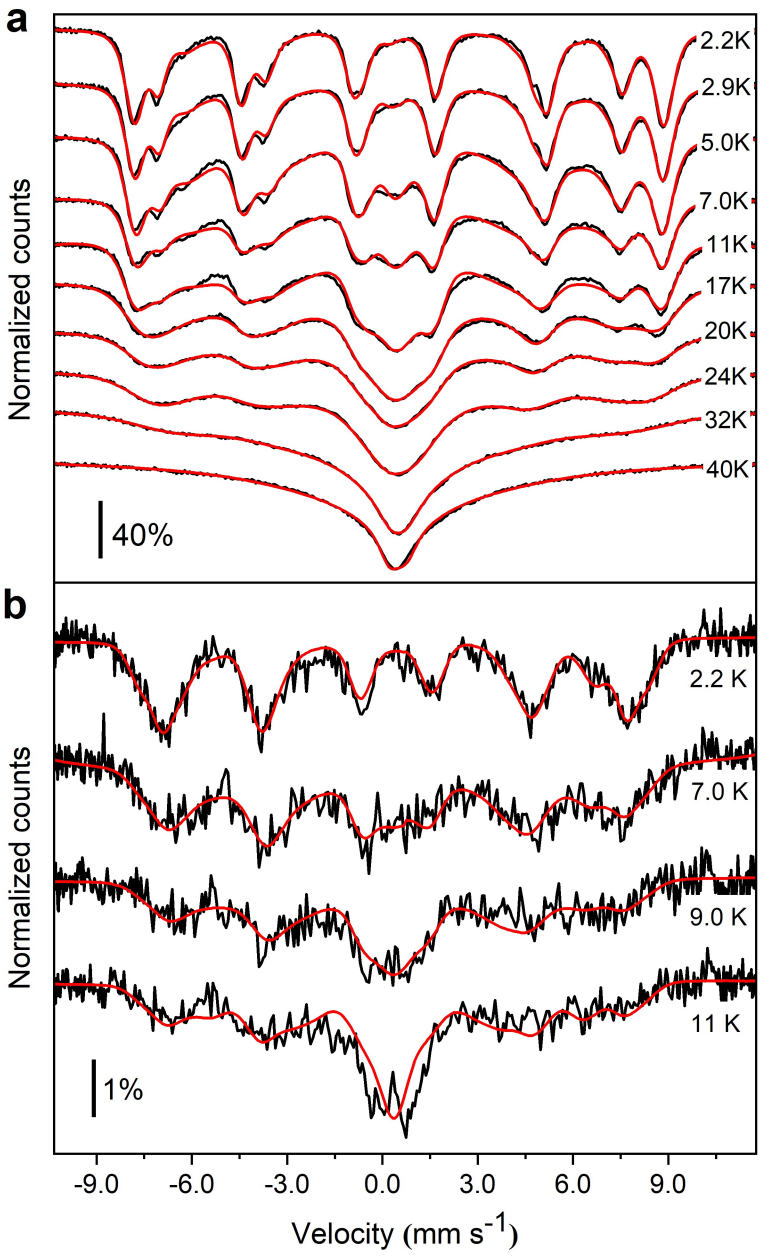

Figure 3.3: Mössbauer spectra (black lines) of the Fe_4 dropcast (a) and monolayer (b) samples for various temperatures. Red lines are the best fit curves. The velocity axis values are relative to the α-Fe standard.

the transmission integral function (Eq. 2.6). For the source lineshape the squared Lorentzian distribution of the SMS [70] was considered. Finally, the effective thickness of the sample was obtained by multiplying the sample effective thickness in a conventional Mössbauer setup by the factor $2/\sin\theta$, where θ is the grazing angle between the surface of the sample and the direction of the incoming radiation. The correctness of the procedure was checked by evaluating the number of iron ions per cm^2 in the dropcast sample. Considering the mean superficial density of the molecule [114], a sample thickness of the order of ~ 100 nm was calculated in agreement with the nominal thickness of the dropcast sample. It is worth noting that, because the sensed Mössbauer thickness is the result of the multiplication by the above-mentioned factor, only synchrotron light at grazing incidence could succeed in detecting Mössbauer spectra not only of the monolayer, but also of such a thin dropcast sample.

The fitting procedure enabled to evaluate the hyperfine interactions for each iron site (the isomer shift with respect to α-Fe, the quadrupole shift and the hyperfine magnetic fields), magnetic anisotropy and magnetic exchange interactions governing the transition rates between different spin sublevels of the system, as well as sample-specific parameters, like thickness and texture. The latter is a parameter quantifying a possible macroscopic orientation of the molecules on the surface. In particular, the possibility to sense a texture, which has a signature in the relative intensities of the lines, is based on the orientation of the quantization axis of the molecule with respect to the gamma-ray polarization.

3.4.1 Dropcast sample

Given that the Fe_4 molecule has a ground spin state $S = 5$, each iron atom is expected to contribute to the spectra with six hyperfine-split lines per $|\pm M_S>$ doublet ($M_S = 1, 2, ...5$) plus two quadrupole-split lines arising from the $|M_S = 0>$ state, thus yielding $4\,(6 \times 5 + 2) = 128$ lines. Some of these transitions may coincide because of the molecular symmetry. In particular, while the central ion (Fe1) experiences a quite distinct coordination environment, the other iron atoms reside in approximately the same coordination environment. Despite this idealized three-fold symmetry, Fe_4 derivatives in the solid state often possess a binary symmetry axis lying along two iron atoms. Therefore, for a quantitative analysis of the dropcast sample spectra we considered that the Mössbauer absorption cross-section is given by the superposition of the contributions coming from three inequivalent iron ions, with intensity ratio 1:1:2.

The agreement between the experimental and calculated data is reasonably good in the whole temperature range (see Fig. 3.3a). In Fig. 3.4a, the cross-section contributions of each Fe(III) site to the spectrum taken at 2.2 K are shown, with best fit parameters reported in Table 3.1. As expected, the Mössbauer parameters associated to three out of the four Fe(III) ions are very similar to each other and their contributions overlap extensively, in agreement with an almost ideal three-fold symmetry of the cluster. The contribution with a significantly different quadrupole interaction and a smaller hyperfine field can be thus safely assigned to the central Fe(III) ion on the

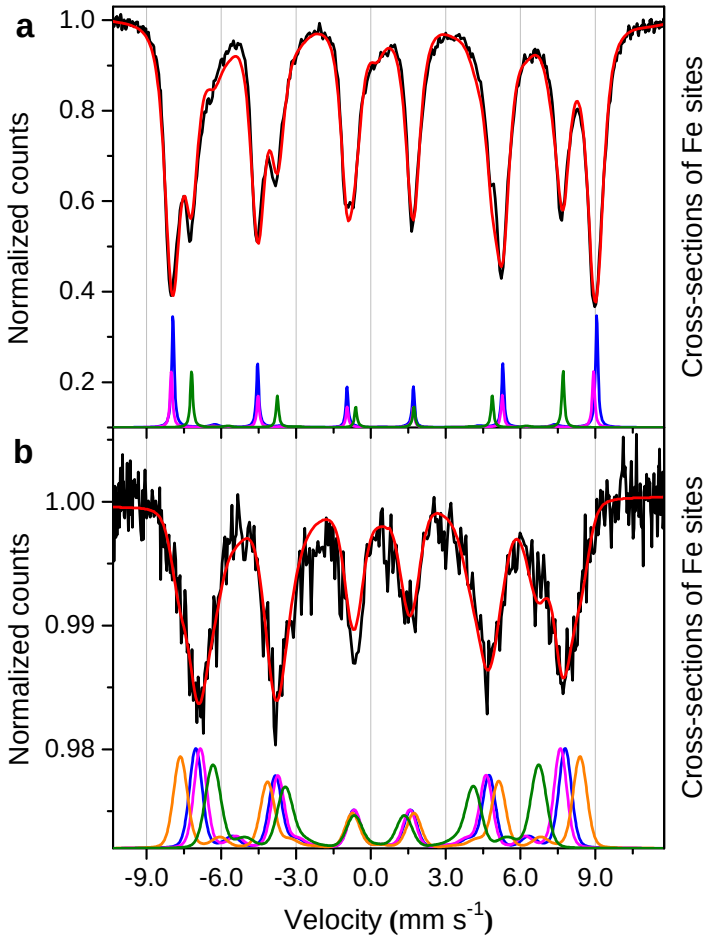

Figure 3.4: a) Mössbauer spectrum at 2.2 K of the dropcast sample (black line) and best fit curve (red line); the cross-sections of the three inequivalent Fe(III) sites expected in a twofold-symmetric molecule are shown in green, magenta and blue and were calculated with the parameters listed in Table 3.1 (columns from left to right, respectively). b) Mössbauer spectrum at 2.2 K of the monolayer sample (black line) and best fit curve (red line); the cross-sections of the four inequivalent Fe(III) sites (green, orange and blue/magenta) were calculated with the parameters listed in Table 3.1 (columns from left to right, respectively).

Sample	Parameter	Fe1	Fe2	Fe3	Fe4
Dropcast	δ (mms^{-1})	0.409(2)	0.418(4)	0.467(2)	0.467(2)
	$\Delta/2$ (mms^{-1})	$-0.149(2)$	0.045(4)	0.094(2)	0.094(2)
	B_{hf}^{fit} (T)	46.39(1)	52.72(2)	52.92(2)	52.92(2)
	B_{hf}^{Fermi} (T)	45.83	51.94	51.94	51.94
	B_{hf}^{AIMD} (T)	46.90	52.34	54.49	53.32
Monolayer	δ (mms^{-1})	0.27(5)	0.43(4)	0.42(6)	0.42(6)
	$\Delta/2$ (mms^{-1})	$-0.07(4)$	$-0.06(2)$	$-0.03(2)$	$-0.03(2)$
	σ (mms^{-1})	0.28(6)	0.25(5)	0.2(1)	0.2(1)
	B_{hf}^{fit} (T)	40.7(4)	49.9(3)	45.6(9)	45.6(9)
	$B_{hf}^{AIMD(W1)}$ (T)	43.68	52.11	52.22	53.04
	$B_{hf}^{AIMD(W3)}$ (T)	45.09	52.50	51.73	49.04

Table 3.1: Mössbauer parameters of the Fe(III) ions extracted from the fit of the spectra at $T = 2.2$ K: δ (isomer shift with respect to α-Fe), $\Delta/2$ (electric quadrupole shift), B_{hf} (hyperfine magnetic field) and σ (standard deviation of the Gaussian broadening). For the dropcast sample the Fermi contact field (B_{hf}^{Fermi}) calculated from the so-called $22 < s_z^i >$ rule is reported. For both samples the hyperfine magnetic field extracted from AIMD calculations (B_{hf}^{AIMD}) is reported; for the monolayer sample geometries resulting from two different AIMD trajectories, i.e., walker 1 (W1) and walker 3 (W3), were considered.

basis of its different coordination environment.

In general, the hyperfine field values are proportional to the number of unpaired $3d$ electrons for each iron ion (i = 1 - 4) and thus to the spin projection along the local direction of the quantization axis. However, exchange interactions introduce spin fluctuations at frequencies higher than the top limit of the Mössbauer time window, so that the measured hyperfine fields are proportional to the time average of the spin projections $< s_z^i >$. The latter are affected by both magnetic exchange interactions and magnetic anisotropies, as most simply described by the spin Hamiltonian:

$$H = \sum_{i,j=1,4}^{i<j} J_{ij}\mathbf{s}_i \cdot \mathbf{s}_j + \sum_{i,j=1,4}^{i<j} \mathbf{s}_i \cdot \overline{d_{ij}} \cdot \mathbf{s}_j + \sum_{i=1,4} \mathbf{s}_i \cdot \overline{D_i} \cdot \mathbf{s}_i \tag{3.1}$$

The first term represents the isotropic exchange interaction, the second one contains the anisotropic part of intramolecular interactions, which are mainly of dipolar origin in assemblies of high spin $3d^5$ ions, while the third one takes into account single ion magnetic anisotropy. Nearest-neighbour antiferromagnetic exchange interactions between the central (i = 1) and peripheral (i = 2, 3 and 4) ions provide the leading term responsible for the ground $S = 5$ molecular state. This state features a ferrimagnetic-like arrangement of the spins, with the central and peripheral spins pointing to opposite directions. Because of magnetic anisotropy, the total spin vector in the ground state lies preferably collinear to the idealized three-fold molecular axis and the $S = 5$ multiplet is thus split approximately according to the giant-spin Hamiltonian [3]

$$H_{S=5} = D\left[S_z^2 - \frac{1}{3}S\left(S+1\right)\right] + E\left(S_x^2 - S_y^2\right) \tag{3.2}$$

where $D < 0$ and E are the second-order axial and transverse magnetic anisotropy parameters, respectively.

Assuming threefold symmetry, i.e. $E = 0$, from the exchange integrals between the Fe(III) ions the spin projection values within the ground $M_S = \pm 5$ doublet were calculated to be $< s_z^1 >= \mp 2.0833$ and $< s_z^2 >=< s_z^3 >=< s_z^4 >= \pm 2.3611$ (in $\hbar$ units). These values can be used to evaluate the Fermi contact field, i.e. the contribution to the hyperfine magnetic field produced by the s electron spin density at the nucleus (see Section 2.1.3.3), that can be expressed by means of the so-called $22 < s_z^i >$ rule [119]. The calculated values are reported in Table 3.1. These values do not differ much from the values of the hyperfine fields extracted from the fit of the spectra, meaning that the Fermi contact field represents the main contribution.

Moreover, below 40 K, the thermal evolution of the spectra likely reflects the contribution of excited states within the $S = 5$ manifold as determined by two main, and somehow distinguishable, mechanisms. Indeed, on increasing temperature, the thermal population of states with $M_S < 5$ increases the number of thermally accessible transitions with a corresponding change in the overall intensity of the lines. On the contrary, the increased transition rate between different states causes changes in shape and shifts the lines towards the center of the spectrum. These statements are clarified

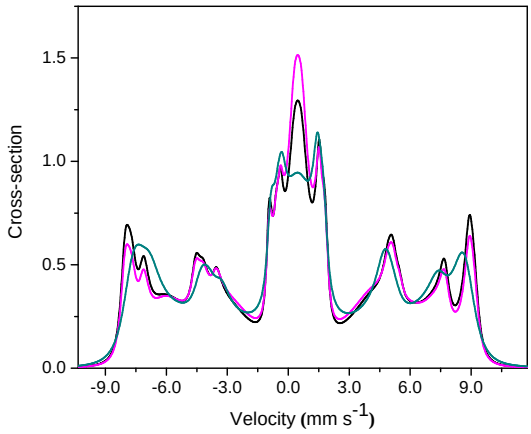

Figure 3.5: Comparison between the total absorption cross-section obtained by fitting the spectrum of the dropcast sample at 11 K (the transition rate extracted from the fit is 3 MHz) (black line), the cross-section simulated for T = 15 K (or a 27 % reduced $|D|$ value) while leaving the other parameters unchanged (magenta line) and the cross-section simulated at T = 11 K for a higher transition rate (10 MHz), expected to occur at 15 K (cyan line).

by means of simulations of the total absorption cross-section of the system following the two mechanisms. In Fig. 3.5, the absorption cross-section obtained from the fit of the 11 K dropcast spectrum is compared with the cross-section simulated for T = 15 K (or correspondingly a 27 % reduced $|D|$ value) while leaving the other parameters unchanged and with the cross-section simulated at T = 11 K for a higher transition rate (in particular, that expected at 15 K). It is evident that, while an increased temperature changes the intensity of the lines, an increased transition rate between different states causes changes in lineshapes and shifts the lines towards the centre of the spectrum. Inspection of Fig. 3.4a shows that the thermal evolution of the spectra is dominated by the population of excited spin states below 11 K and by the increased transition rates above 11 K. Finally, the parameters describing the anisotropy of the system were extracted from the fit of the spectra. The best fit values, D = -0.605(7) K and E = 0.003(1) K, well agree with those resulting from magnetic data for the bulk crystalline phase [116].

The transition rates among the spin states of the $S = 5$ manifold are determined both by the E term, promoting the tunnelling between the two potential wells, and by the interaction of the molecular spin with the thermal bath. In order to take this last interaction into account, a spin-bath interaction term H_{sb} has to be included in Eq. 3.2:

$$H_{sb} = F_b Q_S \left(S_x, S_y, S_z\right) \tag{3.3}$$

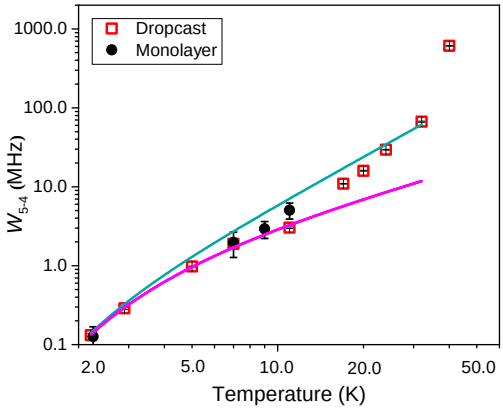

Figure 3.6: Transition rate W_{5-4} between the states $M_S = \pm 5$ and $M_S = \pm 4$ extracted from the fits of the Mössbauer spectra of the dropcast sample (red squares) and of the monolayer sample (black dots) as a function of temperature. The magenta line represents the fit of the data for the dropcast sample at $T \leq 11$ K assuming a direct process as in Eq. 3.4, while the cyan line corresponds to the more general function reported in Eq. 3.5.

where Q_S and F_b are two operators acting on the molecular spin and lattice states, respectively. Considering that the matrix elements of Q_S between two given spin states do not depend on temperature, the thermal dependence of the matrix elements of H_{sb} is linked only to the thermal dependence of the matrix elements of F_b and thus to the physical features of the thermal bath and to the specific interaction scheme [108]. In particular, the parameters determining the thermal dependence of the spectra are proportional to the Fourier transform of the correlation function of F_b evaluated at the transition frequencies. This quantity can be evaluated at zero frequency in the usual approximation where the linewidth of bath states is larger than the energy separation between the electronic spin states.

In the approximation introduced above, the spin dynamics depends on the transition rates between the electronic spin states of the molecule. In order to analyse the spin dynamics as a function of temperature, the transition rate W_{5-4} between $M_S = \pm 5$ and $M_S = \pm 4$ states was chosen as a fit parameter. All other transition rates between two generic i and j states were derived according to the relations $W_{j-i} = W_{5-4} \frac{|<i|Q_S|j>|^2}{|<5|Q_S|4>|^2}$ and $W_{i-j} = W_{j-i} \exp\left(\left(E_i - E_j\right)/k_B T\right)$.

Fig. 3.6 reports the temperature dependence of W_{5-4}, together with a fit of the data up to 11 K with a function of the form

$$W_{5-4} = \frac{A}{\exp\left(B/k_B T\right) - 1} \tag{3.4}$$

which is representative of a direct process, i.e. a direct transfer of energy from the spin system to the lattice phonon bath. This analysis of low temperature transition rates yields $B = 6.8(4)$ K and $A = 2.8(3) \times 10^6$ Hz.

For temperatures above 11 K, the increase of W_{5-4} is more rapid than predicted by Eq. 3.4 suggesting two-phonons processes. These can be taken into account using the expression

$$W_{5-4} = \frac{A \exp\left(B/k_B T\right)}{\left(\exp\left(B/k_B T\right) - 1\right)^2} \tag{3.5}$$

that describes a Raman process due to optical modes. Equation 3.5 coincides with Eq. 3.4 for $T \ll B$, while for $T > B$ it gives a T^2 dependence [66]. The fit, shown in Fig. 3.6, was performed keeping the B parameter fixed at the value extracted from low temperature data. Equation 3.5 is qualitatively in agreement with the experimental data in a wide range of temperatures, suggesting that the spin dynamics is related to an optical mode with an energy of about 7 K (or, equivalently, a frequency of about 0.1 THz). A rapid increase of the transition rate is observed at the highest investigated temperature (40 K) where other total spins states start to be significantly populated.

3.4.2 Monolayer sample

The analysis of the spectra was performed following the same strategy used for the dropcast sample. From the fitting of the spectrum taken at the lowest temperature, a surface density of about 3 ^{57}Fe ions per nm^2 was estimated. This value agrees, within the experimental uncertainty of the technique, with the one evaluated by a Scanning Tunneling Microscope study of Fe_4 molecules evaporated on a gold single crystal (~ 2 ^{57}Fe ions per nm^2) [114]. Therefore, our study represents the first successful investigation of a monolayer of molecules by means of Mössbauer spectroscopy: the SMS allows to increase by about two orders of magnitude the sensitivity of the technique with respect to that achieved with a conventional setup based on a radioactive source.

The best fit calculated curves are shown in Fig. 3.3b for each sampled temperature. The individual Fe(III) cross-section contributions to the spectrum taken at 2.2 K are shown in Fig. 3.4b, with best fit parameters reported in Table 3.1. In order to comply with a possible reduction of symmetry of the cluster, four non-equivalent Fe sites were considered in the fitting procedure. However, two contributions are identical within error (blue and magenta lines in Fig. 3.4b) and only three non-equivalent Fe sites are thus reported in Table 3.1. The parameters in Table 3.1 were kept fixed in the analysis of the spectra acquired at higher temperatures, while the transition rate W_{5-4} and the D parameter were let free to vary.

The texture value extracted from each spectrum revealed no preferential orientation of the molecules on the substrate. This statement is confirmed by a simulation of the same sample, where, as texture parameter, the anisotropy axes of the SMM molecules were assumed to lie at about 35° from the substrate normal, as previously detected by

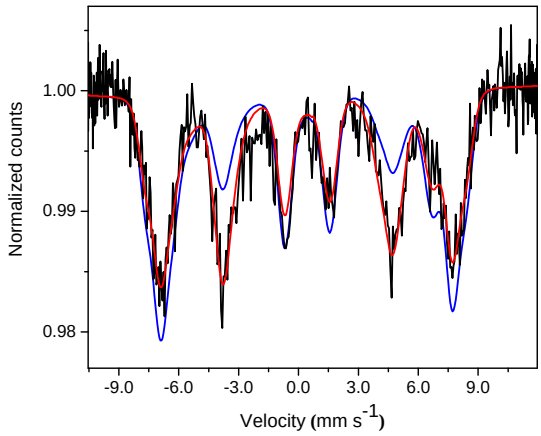

Figure 3.7: Mössbauer spectrum of the monolayer sample at 2.2 K (black line) and corresponding fit assuming a random orientation of molecules on the substrate (red line). The blue line is a simulation of the same system imposing a preferential orientation of the molecules.

X-ray absorption experiments of the same molecule on Au(111) [116]. Such a preferential orientation determines a redistribution of line intensities and yields an asymmetrical pattern that does not correspond to the experimental data (see Fig. 3.7). Therefore, this simulation confirms that the Mössbauer spectra of the monolayer sample are correctly fitted considering a random orientation of the molecules. This discrepancy with the previous observation is however not unexpected, since a reconstructed, atomically flat Au(111) surface, known to promote the preferential orientation detected by X-ray natural linear dichroism [116], could not be used for the Mössbauer experiments.

As a distinctive feature of the monolayer's spectra, all the lines of each sextet are characterized by approximately the same linewidth, although larger than that found in the dropcast sample. Two mechanisms can be responsible for the observed line broadening. Faster transition rates between spin levels broaden the lines, but, at the same time, promote a collapse towards the center of the spectrum, which is not experimentally observed in the 2.2 K spectrum. Moreover, in order to reproduce the temperature dependence of the spectra an unphysical decrease of transition rates upon increasing temperature would be required. An alternative source of broadening is the presence of an inhomogeneous distribution of electric parameters (quadrupole shift and/or isomer shift). A significant distribution in hyperfine fields can be safely ruled out as it would affect the external lines approximately six times more than the internal ones. This factor is due to the energy difference between the Zeeman split excited and fundamental nuclear states [120].

The presence of inhomogeneous broadening in the electric parameters was thus taken into account by assuming Gaussian lines with standard deviation of the order of 0.2 -

0.3 mms^{-1}, as estimated from the lowest temperature spectrum, which is less affected by spin dynamics. If the observed broadening is ascribed to a distribution of the ligand contributions to the quadrupole interaction, the ligand donor atoms must undergo displacements of the order of 0.04 Å from their average positions. These deformations were undetected by previous XMCD studies. Furthermore, all the magnetic hyperfine field values are significantly smaller than those found in the dropcast sample.

As a final point, the spin dynamics of the grafted Fe_4 molecules was addressed by investigating the temperature evolution of the spectra. Despite the much worse signal-to-noise ratio, it is evident that, on increasing the temperature, the external lines lose intensity faster than in the dropcast sample. This suggests that the $|D|$ value is reduced upon grafting, as directly confirmed by fitting the Mössbauer spectrum recorded at the lowest temperature (D = -0.49(6) K, with the E/D ratio held fixed at the value found in the dropcast sample to avoid overparametrization in the fitting of poorly resolved spectra). At the same time the transition rate W_{5-4} extracted from the fit of the spectra is comparable with that found for the dropcast sample (see Fig. 3.6). Thus, Mössbauer data of the monolayer sample indicate that the deposition on a surface does not significantly modify the spin dynamics, as suggested by previous XMCD evidences [116].

3.5 Ab initio calculations

The results coming from the fit of the Mössbauer spectra were compared with *ab initio* molecular dynamics (AIMD) calculations recently performed on the same molecule grafted on the Au(111) surface [113]. AIMD provides in fact a proper sampling of the accessible space of configurations at finite temperature. The generated trajectory is expected to visit the accessible structures according to their statistical probability under selected thermodynamic conditions. In this respect, the molecular dynamics simulation samples the free energy surface underlying the dynamics of the system of interest and reproduces its characteristic thermal fluctuations. Eight optimized geometries were considered. Both dynamical information and steady state structures which could statistically well describe the molecular geometry once the SMM is grafted on Au(111) were obtained, as well as the molecular magnetic properties of the grafted molecule.

The picture emerging from the AIMD investigation was that van der Waals interactions between the gold substrate and the aliphatic tether of the tripodal ligand cause significant distortions of the magnetic core. Such interactions induce several accessible energy minima in the potential energy surface of the system. The predicted scenario closely matches that emerging from the Mössbauer spectra of the monolayer sample. Remarkably, the standard deviation of Fe-O bond lengths, estimated over eight different AIMD trajectories or walkers, has the order of magnitude (10^{-2} Å) required to account for the observed line broadening through a distribution of quadrupole shifts.

A pronounced variation of Fe-O bond lengths among the different walkers is observed for the central site (Fe1) and for the Fe atom closer to the aliphatic chain tethered to

the gold substrate, namely Fe3 in Fig. 3.1c. Moreover, AIMD calculations showed that both single ion magnetic anisotropies and exchange interactions are affected by the grafting process. However, these modifications partially compensate each other so that the molecule retains an $S = 5$ ground state and an easy-axis magnetic anisotropy.

Focusing now on the hyperfine field experienced by the ^{57}Fe nuclei, the process of chemical grafting on the gold surface can affect both the individual $< s_z^i >$ values, by altering intramolecular exchange interactions in Eq. 3.1 and the extent of electron delocalization on the nuclei. For the eight investigated AIMD trajectories [113] the local z components in the $M_S = \pm 5$ doublet are on average smaller in absolute value than in the bulk phase. The difference is more clearly visible on the central site Fe1 (2.087 vs. 2.137 $\hbar$) than on peripheral sites (2.361 vs. 2.378 $\hbar$). Furthermore, Fe3 shows the largest spread of $< s_z^i >$ values (± 5 %) over the eight walkers. In order to assign the observed hyperfine fields to specific Fe(III) ions, we assumed that the hyperfine field is an increasing function of $| < s_z^i > |$ averaged over the eight walkers. A linear trend was obtained, the slope of which is similar to that of the bulk sample, further indicating that Fe_4 complexes retain their magnetic features on surface. However, all values seem to be shifted on average by 6 T towards smaller fields.

In order to shed some light on this aspect, further *ab initio* calculations of the isotropic hyperfine magnetic fields were performed. We considered the optimized geometry in the crystalline phase and two of the geometries obtained by AIMD trajectories after extrapolating the Fe_4 complex from the underlying gold surface. The computed hyperfine magnetic fields, reported in Table 3.1, are dominated by the Fermi contact term. The time-demanding relativistic spin-orbit coupling contributions were not computed, as they are expected to be negligible for high spin Fe(III). In agreement with Mössbauer spectra, the lowest hyperfine magnetic field is computed for the central iron in both bulk-phase and on-surface molecules, primarily as a consequence of the different $< s_z^i >$. The hyperfine fields are on average reduced upon grafting. The strongest reduction (-2.5 T) is calculated for the central iron atom, but it is much smaller than that found experimentally.

The above described *ab initio* calculations only include surface-induced structural deformations, but neglect electronic effects of the metal surface. Their inclusion is not possible with the same accuracy, therefore the local spin densities were computed by pseudo-potential Gaussian Plane Waves (GPW-DFT) calculations by considering both the Fe_4 molecule and 314 gold atoms of the underlying slab.

In order to avoid spurious effect due to the use of pseudopotentials, these spin densities were compared to the ones obtained, at the same level of calculation, on molecules with the same geometry, but removing the gold slab, also referred to as extrapolated geometry. The results, averaged over the eight investigated AIMD trajectories, indicate that a small, but sizable reduction of the spin density occurs due to a purely electronic effect of the gold substrate, thereby hinting to a decreased polarization of core s orbitals of iron ions. The expected reduction of hyperfine fields, reported in Table 3.1, is of the order of 2 T for Fe1 and significantly smaller for the remaining ions. Though a similar investigation considering all-electron basis is not affordable, the observed reduction

of hyperfine magnetic fields on the surface can be ascribed to both geometrical and electronic perturbations induced by the grafting process.

3.6 Conclusions

Synchrotron Mössbauer spectroscopy applied to a monolayer of molecules has provided unprecedented insights in the process of chemical absorption of a complex molecule on a surface. This has been achieved thanks to the largely increased sensitivity, without significant loss in spectral resolution, that characterizes the SMS as compared with a conventional Mössbauer setup.

The resulting scenario is that significant deformations of the magnetic core are induced by the interaction with the substrate, even in the relatively well-protected and rigid Fe_4 structure. These deformations emerge clearly from state-of-the-art AIMD modelling, but are undetectable by conventional synchrotron based magneto-optical techniques, such as XMCD, as well as by more local probes, like scanning probe techniques. In the latter case, in fact, the tip of the microscope mechanically induces deformation, thus altering the molecular structure [121].

However, the modifications induced by the grafting on the substrate do not alter the overall magnetic structure of the system; therefore, the spin state and the anisotropy of the system, and consequently the SMM behavior, are retained after deposition. This makes the Fe_4 class of molecules particularly well suited for organization on surface and insertion in single molecule devices. In this sense, synchrotron Mössbauer spectroscopy based on SMS proves to be a powerful technique that could be employed in the investigation of other types of molecules assembled in monolayer architectures in view of the rational design of hybrid interfaces [122] and single molecule spintronic devices.

Author contributions: A.Co., M.M. and R.S. planned the investigation. A.Co. synthesized the material while molecular films were prepared by M.M. A.Ci., A.Co. and M.M. performed the experiments with the assistance of A.Ch. and R.R. Mössbauer data were analysed by A.Ci., M.F. and G.S. with the support of A.Co. and R.S.; F.T. performed the ab initio studies. All authors contributed to the discussion and to the drafting of the manuscript.

Chapter 4

Mössbauer spectroscopy of a spin crossover complex deposited on gold

A spin crossover (SCO) complex deposited on a gold substrate was investigated by means of synchrotron Mössbauer spectroscopy. Samples having different thicknesses of deposited molecules were studied. The SCO transition was induced both thermally and via LIESST effect. A reduction of the SCO efficiency is encountered with respect to molecules in the bulk phase. The value of the SCO efficiency is comparable between the two used external stimuli.

Manuscript in preparation

4.1 Introduction

Spin crossover (SCO) molecules are bistable systems that can reversibly switch between two distinct spin states, a low spin (LS) and a high spin (HS) state, by means of a variety of external stimuli, such as an increasing of temperature [47, 48] or the absorption of electromagnetic radiation of appropriate wavelength (LIESST effect) [49, 50, 51]. The possibility to change the spin state of the system via an external input makes SCO complexes promising building blocks for spintronic [7, 15] and high-density memory devices, as well as potential elements for displays and sensors [13, 14]. However, the SCO transition is a cooperative phenomenon [57] and its features depend on the environment surrounding the molecule. In literature (a list of publications on Fe(II)-based SCO molecules is reported in Appendix A) studies of different kinds of molecules deposited down to a single molecule layer on different substrates show a reduction of the SCO efficiency with respect to molecules in the bulk phase. Therefore, in view of the proposed applications the SCO efficiency of the molecules has to be verified once they are deposited on a surface.

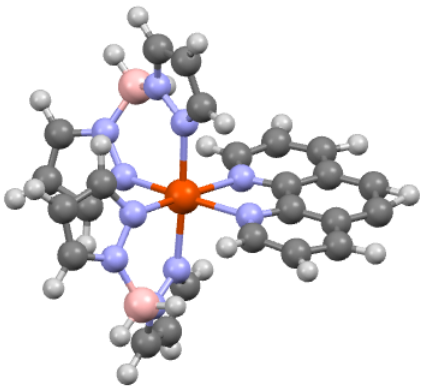

Figure 4.1: Structure of the SCO complex **1** (color code: Fe atom in orange, N in blue, B in pink, C in dark gray and H in light gray).

Mössbauer spectroscopy is a powerful technique to investigate Fe(II)-based SCO complexes, being able to readily evaluate the LS and HS percentages present in the collected spectra at each temperature, in the hypotheses that the increase of the metal-ligand length following the SCO transition does not change significantly the temperature dependences of the f factor for HS and LS states and that the lifetimes of the spin states be outside of the Mössbauer time window. Moreover, Mössbauer spectroscopy can deeply characterize the electronic structure of each spin state and eventually the modifications induced by the interaction with the substrate. However, as noticed in Section 2.1.4, the sensitivity of a standard setup based on a radioactive source is suitable to study only molecules in the bulk phase. This limitation was overcome by means of synchrotron Mössbauer spectroscopy based on SMS, that allows to collect energy-domain spectra of thin films of molecules adhered on a substrate, as evidenced by our study on the Fe_4 SMM deposited on gold reported in Chapter 3.

Here synchrotron Mössbauer spectroscopy was used to study the SCO transition of a Fe(II)-based SCO complex deposited on gold. The SCO transition was induced both thermally and via LIESST effect.

4.2 Spin crossover complex

The object of this study was the SCO complex $[Fe(H_2B(pz)_2)_2(phen)]$ (pz = pyrazolyl, phen = 1,10-phenantroline), here after called **1**. Its structure is shown in Fig. 4.1. Each Fe(II) ion is surrounded by six nitrogen atoms belonging to two $H_2B(pz)_2^-$ ligands and one phen group.

As a Fe(II)-based SCO complex, **1** can switch between a LS with a total spin $S = 0$ and a HS with $S = 2$. Magnetic susceptibility measurements on powder samples of **1** show an abrupt spin transition at a transition temperature of the order of 160 K with a small hysteresis loop of about 4 K [123, 58]. Mössbauer measurements on powder samples of **1** show that at 250 K about 90 % of the molecules are in the HS state, while at 80 K there are no molecules in the LS state [123]. Therefore the SCO transition is complete in the bulk phase. The LIESST effect is expected for an irradiation with electromagnetic radiation with wavelength of about 990 nm.

Molecules of **1** were enriched in 97 % ^{57}Fe and deposited on a gold substrate by thermal sublimation in high vacuum. Two samples were realized, with a thickness of 50 nm and 5 nm, respectively. A thicker sample (with thickness of the order of 100 nm) was obtained by drop casting a 0.5 mM solution in CH_2Cl_2 of **1** on the same substrate.

4.3 Mössbauer measurements

Energy-domain Mössbauer spectra were realized by taking advantage of the Synchrotron Mössbauer Source (SMS). As shown by our study on Fe_4, the features of the synchrotron light coming from the iron borate crystal together with the possibility to realize the measurements in grazing incidence geometry allow to achieve the necessary sensitivity to study thin films. Concerning our samples of **1**, after measuring their reflectivity as a function of θ, incidence angles comprised between 0.1° and 0.2° were chosen for the three investigated samples.

The SCO transition was induced both thermally and via LIESST effect. This second study required the design of a new version of the sample holders, that were optimized in order to accommodate the LEDs used for the illumination. In particular, two LEDs were aligned along the sample, perpendicular to the x-ray beam. The LEDs guaranteed a uniform illumination of the samples. InGaAsP LEDs with 1050 nm nominal wavelength, decreasing to 990 nm at low temperature, were used.

In Fig. 4.2, the Mössbauer spectra of the dropcast sample recorded at high and low temperature are reported. At 278 K, the spectrum is essentially a doublet with a quadrupole splitting of approximately 2 mm/s, that is characteristic of a HS state of **1** in the bulk phase [123, 58]. However, the spectrum is not symmetric, pointing to the presence of a minor LS contribution. At 3.0 K, the doublet is broadened and a third line appears at about 0.7 mm/s, which can be ascribed to a quadrupole split-line of the LS state. However, contrarily to **1** in the bulk phase, the HS contribution at low temperature is not negligible.

In Fig. 4.3, the Mössbauer spectra of the sublimated samples recorded as a function of the temperature are reported. For the 50 nm thick sample, the spectrum realized at 240 K qualitatively resembles that of the dropcast sample at high temperature, except for the decreased intensity of the spectral lines due to the lower number of ^{57}Fe nuclei present in the sublimated sample. By lowering the temperature, two features can be noted: an overall broadening of the absorption lines and the increase in weight of a third

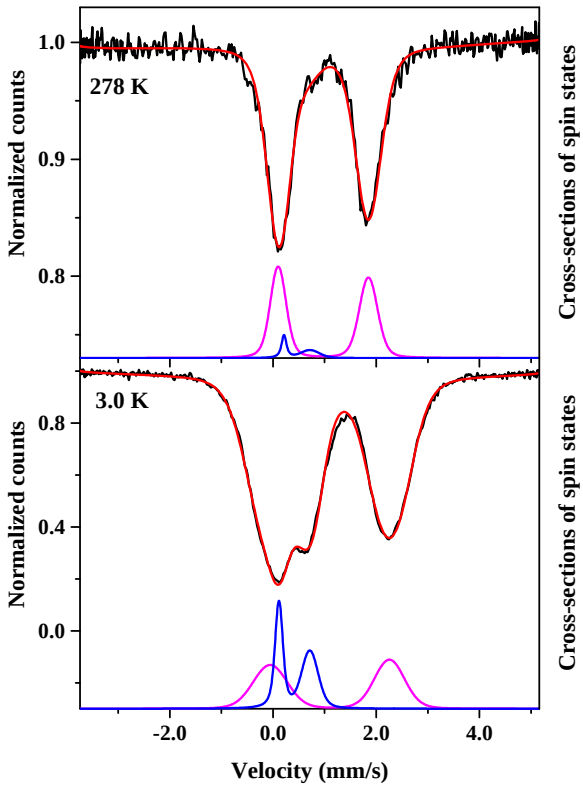

Figure 4.2: Mössbauer spectra at 278 K and 3.0 K of the dropcast sample (black lines) and corresponding best fit curves (red lines). The absorption cross-sections associated to the HS state (magenta line) and the LS state (blue line) are shown. The velocity axis values are relative to the α-Fe standard.

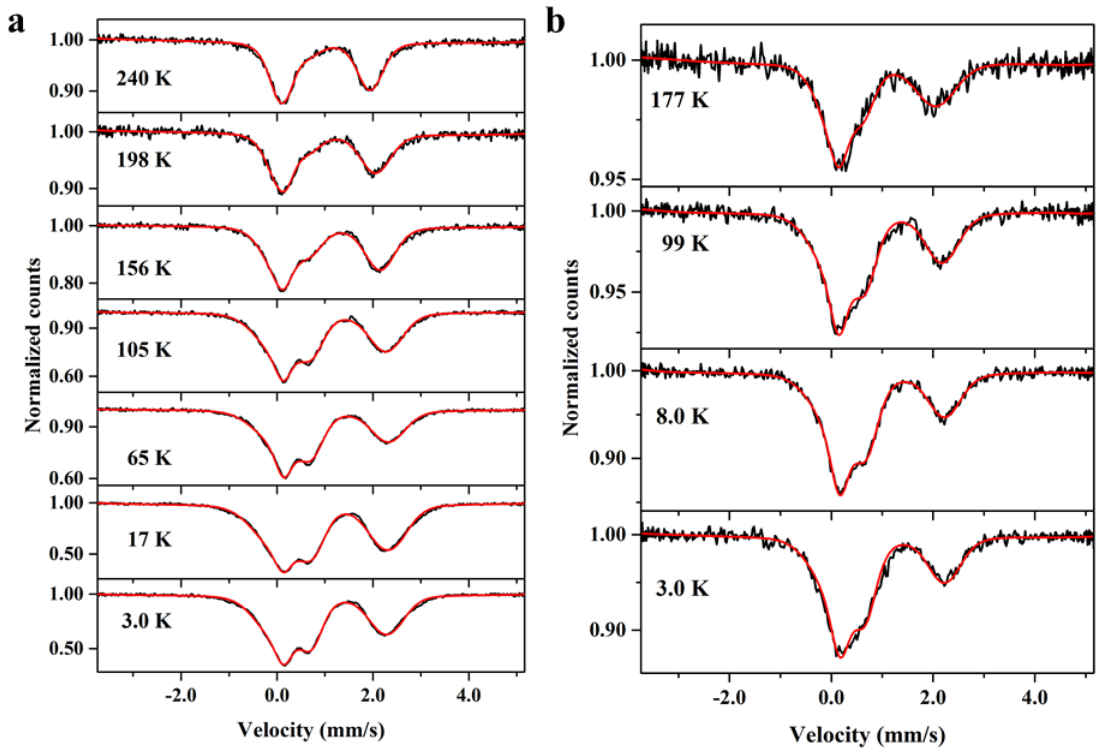

Figure 4.3: Mössbauer spectra as a function of temperature (black lines) and corresponding best fit curves (red lines) of the sublimated 50 nm thick sample (a) and the 5 nm thick sample (b). The velocity axis values are relative to the α-Fe standard.

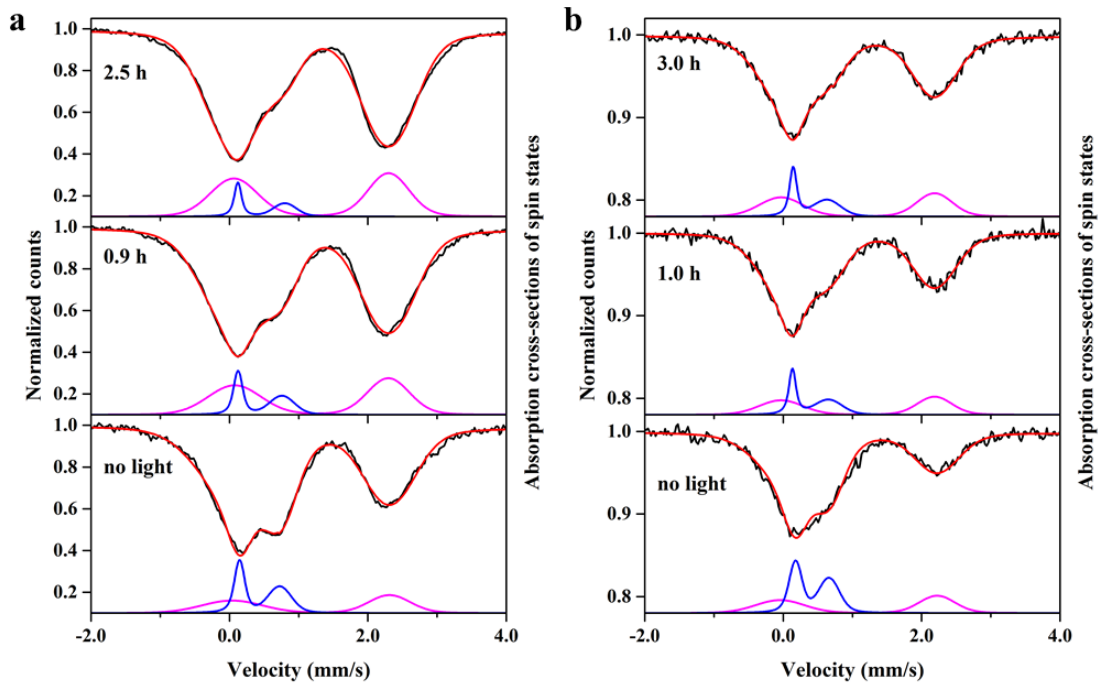

Figure 4.4: Mössbauer spectra realized at low temperature for different irradiation times (LIESST effect) (black lines) and corresponding best fit curves (red lines) of the sublimated 50 nm thick sample (a) and the 5 nm thick sample (b). The absorption cross-sections associated to the HS state (magenta line) and the LS state (blue line) are shown. The velocity axis values are relative to the α-Fe standard. The velocity range is restricted to better evidence the relevant part of the spectra.

line at about 0.7 mm/s, due to a line of the LS doublet, in parallel to what happens in the dropcast sample. Therefore, an increasing LS contribution is superimposed on the broad HS line. At 3.0 K, a significant contribution from the HS state is still present, pointing to an incomplete spin conversion. Finally, the thermal dependence of the recoilless fraction parameter f determines an important increase in the overall intensity of the spectra upon decreasing the temperature.

In the Mössbauer spectra of the 5 nm thick sample (Fig. 4.3b), a worse signal-to-noise ratio is evident, compatible with the reduced number of ^{57}Fe nuclei present in this sample. Nevertheless, the thermal dependence of the spectra is observable. The strong asymmetry of the high temperature spectrum points to a significant contribution of the LS component in all the investigated temperature range.

In order to further characterize the effect of the substrate on the SCO transition of the **1** molecules, LIESST measurements were realized, irradiating the sublimated samples at low temperature (6.0 K and 3.0 K for the 50 nm thick and the 5 nm thick sample, respectively) in cw mode with 990 nm wavelength radiation. The Mössbauer

spectra measured after different irradiation times (up to about 3 hours) are shown in Fig. 4.4 (for the 50 nm thick sample three representative irradiation times are reported, while all the spectra are reported in Appendix A). For both samples the temporal evolution of the shape of the spectra suggests that a certain amount of molecules is converted from the LS state to the HS state by the irradiation. It must be noted that the spectra of the 5 nm thick sample result less noisy than the spectra acquired as a function of the temperature, because LIESST effect is realized at 3.0 K.

4.4 Fitting of the spectra

The quantitative assessment of the spin conversion in each sample required the evaluation of the Mössbauer absorption cross-section of the samples. At each temperature, each spectrum was considered as resulting from the contribution of a HS and a LS site. These sites were characterized by different electric hyperfine parameters (isomer shift and quadrupole splitting), as well as sample-specific parameters, as thickness and texture (a parameter describing the possibility of a preferential orientation of the molecules on the substrate). Moreover, an appropriate fitting of the spectra required to introduce a distribution of quadrupole splitting values (Δ), which was assumed as Gaussian with a standard deviation σ. In addition, a correlation between the quadrupole splitting and the isomer shift (δ) was considered, defined by the equation

$$\delta - \delta_0 = \frac{\alpha\,(\Delta - \Delta_0)}{2} \tag{4.1}$$

where α is the correlation coefficient and δ_0 and Δ_0 are the mean values of δ and Δ, respectively. Consequently, two different distributions were associated with the hyperfine parameters δ and Δ with the corresponding standard deviations calculated as $|\alpha\sigma|$ and 2σ, respectively. The result of this procedure is that the lines of each spin doublet are differently broadened, according to Gaussian functions characterized by standard deviations defined as $|\alpha \pm 1|\sigma$. Therefore, the correlation between the quadrupole splitting and the isomer shift given by Eq. 4.1 resulted into different linewidths of each line of the quadrupole doublet.

In order to take into account the dependence of the Mössbauer spectra on the sample effective thickness, the resulting total cross-section of the sample was inserted into the transmission integral function (Eq. 2.6). For its evaluation, the same considerations on the source lineshape and effective thickness of the sample were applied as in the study of Fe_4 (see Section 3.4). The correctness of the fitting procedure was checked by finding a scaling factor of about ten between the values of the thicknesses of the two sublimated samples.

4.4.1 Thermal spin crossover

In Fig. 4.2, the best fit curves of the Mössbauer spectra and the absorption cross-section contributions of the HS and LS states are shown for the dropcast sample, while best

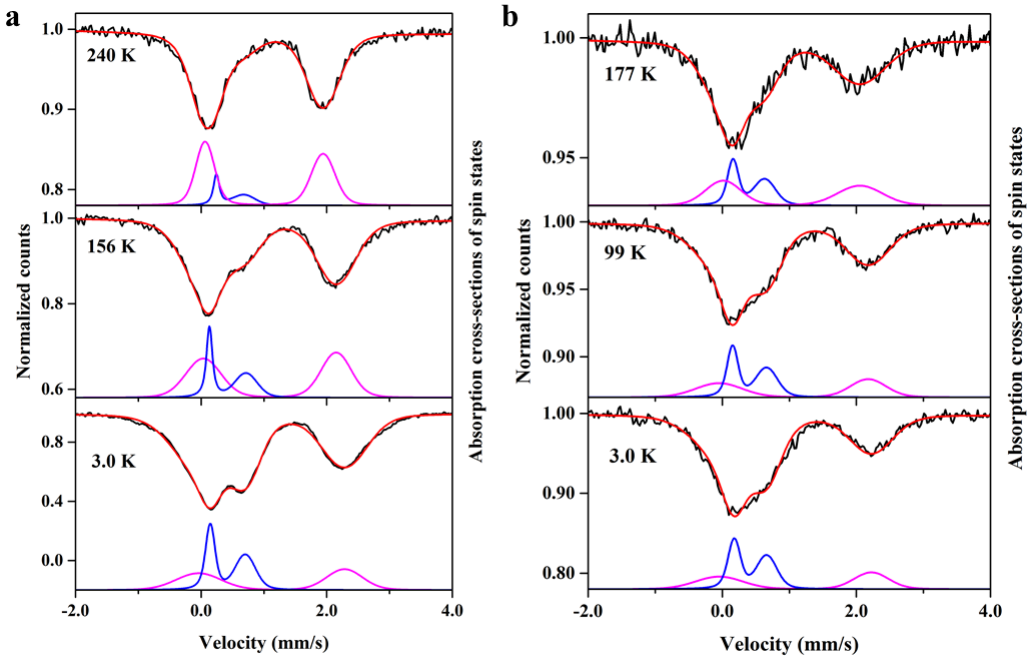

Figure 4.5: Mössbauer spectra (black lines) and corresponding best fit curves (red lines) for three selected temperatures of the sublimated 50 nm thick sample (a) and the 5 nm thick sample (b). The absorption cross-sections associated to the HS state (magenta line) and the LS state (blue line) are shown. The velocity range is restricted to better evidence the relevant part of the spectra.

fit parameters are reported in Table 4.1. As qualitatively observed from the inspection of the spectra, a combination of HS and LS states is present both at high and low temperature. The values of the corresponding hyperfine parameters change with the temperature and are in agreement with those reported for the same molecule in the bulk phase [123, 58]. Moreover, at high temperature, the shape of the cross-section due to the HS state is made up of an approximately symmetric doublet (low value of α) and it broadens passing from 278 K to 3.0 K (σ increases). On the contrary, the LS contribution is clearly asymmetric and constituted of a narrow line with practically natural linewidth and another one that is about ten times broader.

As for the dropcast, also for the sublimated samples a good agreement between measured and calculated spectra is found in all the thermal range (the HS and LS contributions used in the fitting procedure at representative temperatures are reported in Fig. 4.5). Best fit parameters extracted from the fit of the spectra acquired at the highest temperature and 3.0 K are reported in Table 4.1, while the temperature behavior of the hyperfine parameters associated to the HS and LS sites is reported in Fig. 4.6. The values of isomer shift and quadrupole splitting for the HS and LS states are in line with those extracted from the fit of the dropcast spectra. Also the shape

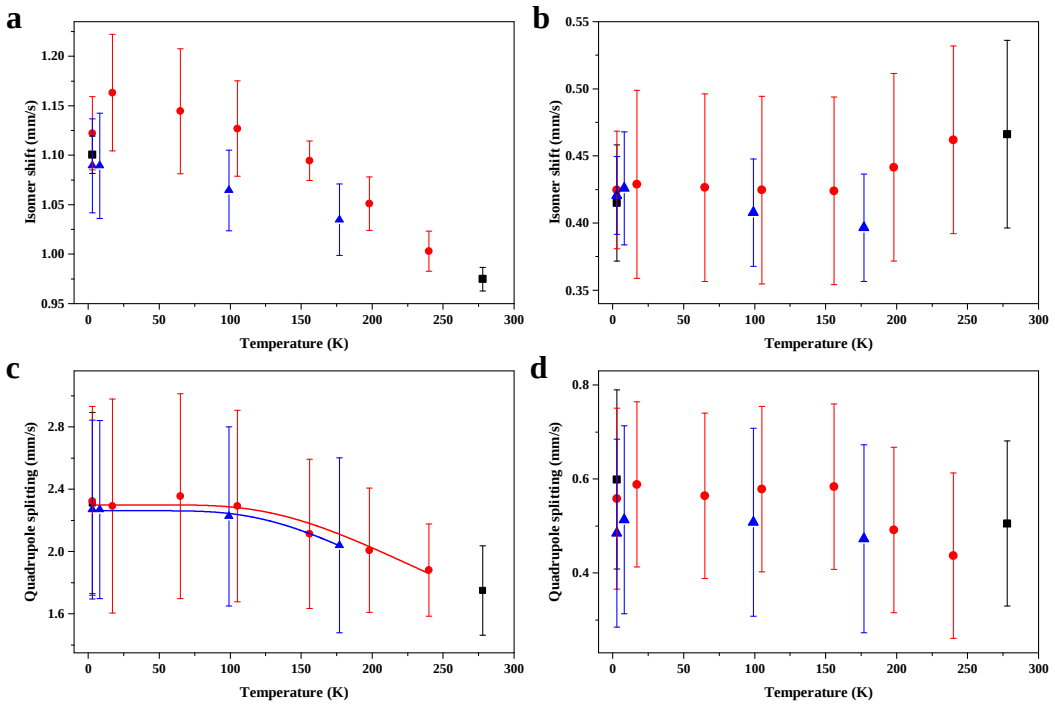

Figure 4.6: Temperature behavior of the hyperfine parameters extracted from the fit of the Mössbauer spectra of the 50 nm thick sample (red dots), the 5 nm thick sample (blue triangles) and the dropcast sample (black squares). Isomer shift with respect to α-Fe (a) and quadrupole splitting (c) of the HS state. Isomer shift with respect to α-Fe (b) and quadrupole splitting (d) of the LS state. In each panel the bar represents the distribution of the values around the mean value. In panel c, the fits of the data relative to the sublimated samples with the function of Eq. 4.2 are shown.

Sample	T(K)	Site	δ_0(mm/s)	Δ_0(mm/s)	σ(mm/s)	α	%HS
Dropcast	278	HS	0.975(8)	1.75(2)	0.14(1)	0.08(7)	91(4)
		LS	0.47(8)	0.5(2)	0.088	0.79	
	3.0	HS	1.101(1)	2.311(2)	0.291(2)	-0.065(5)	59.8(5)
		LS	0.41	0.6	0.095	0.45	
50 nm	240	HS	1.003(4)	1.880(8)	0.148(6)	0.14	84(3)
		LS	0.46(2)	0.44(3)	0.088	0.79	
	3.0	HS	1.122	2.324(5)	0.303(3)	-0.122(9)	50.2(6)
		LS	0.425(2)	0.558(3)	0.096(3)	0.45(6)	
5 nm	177	HS	1.03(2)	2.04(5)	0.28(3)	0.1(1)	60(8)
		LS	0.40(3)	0.47(4)	0.10(3)	0.4(3)	
	3.0	HS	1.09(1)	2.27(3)	0.29(2)	-0.17(5)	45(3)
		LS	0.421(8)	0.485(9)	0.10(1)	0.29(8)	

Table 4.1: Mössbauer parameters of the HS and LS states extracted from the fit of the spectra measured at the highest and lowest temperature of each sample: isomer shift with respect to α-Fe (δ_0), quadrupole splitting (Δ_0), standard deviation (σ) of the Gaussian broadening describing the distribution of values of Δ_0 and correlation coefficient (α) between the quadrupole splitting and the isomer shift. The calculated HS fraction (%HS) is also reported. Parameters with no error were kept fixed in the fitting procedure.

of the cross-sections is similar between the three samples: the spin states have similar values of σ and α.

The thermal behavior of the hyperfine parameters of the HS and LS states reveals fine details of the electronic structure of the molecule in the different samples and therefore indirectly of its interaction with the substrate.

The values of the hyperfine parameters of the HS state increase upon lowering the temperature (see panels a and c of Fig. 4.6). In particular, the isomer shift exhibits the usual temperature dependence due to the second order Doppler effect, showing a linear dependence on the logarithm of the total effective thickness (see Section 2.1.3.1). A linear fit of δ as a function of $\ln t_a$ gives a slope of 0.036(7) mm/s and of 0.047(2) mm/s for the 50 nm and 5 nm thick samples, respectively (the fits are reported in Appendix A). While the linear trend is in a qualitative agreement with the theoretical model, a comparison between the theoretical value of the slopes and the value extracted from the fit is not possible, because the slope value depends on the actual dispersion of phonon mode and on the ratio between the f-coefficient of the HS and LS states.

Passing to the quadrupole splitting of the HS state, its temperature dependence can be fitted by the relation [64]

$$\Delta_0 = A\frac{1-\exp\left(-D/T\right)}{1+2\exp\left(-D/T\right)} \tag{4.2}$$

where D is the splitting within the fundamental t_{2g} states of the Fe(II) ion due to

axial distortion, A is related to the energy level splitting in the crystalline field and T is the temperature. The fits of the quadrupole splitting of the HS state with Eq. 4.2 are shown in panel c of Fig. 4.6 and give $A = 2.30(3)$ mm/s and $D = 627(21)$ K (corresponding to $5.4(2) \times 10^{-2}$ eV) and $A = 2.26(1)$ mm/s and $D = 591(15)$ K (corresponding to $5.1(1) \times 10^{-2}$ eV) for the 50 and 5 nm thick samples, respectively. The good match of the D values between the two samples suggests that very similar crystal fields affect the Fe(II) ion in both cases.

The hyperfine parameters of the LS state remain practically constant upon decreasing the temperature (see panels b and d of Fig. 4.6). This is expected for the quadrupole splitting, while, concerning the isomer shift, a mechanism compensating the second order Doppler effect should be present. Consequently, the LS electronic state should change with temperature.

It is instructive to translate the obtained broadenings of the quadrupole splitting into the heterogeneity in the Fe-ligand distances by the dependence of ligand contribution to the EFG on these distances. At 3.0 K, for the HS state, variations of 0.04 Å in the Fe-ligands distances can be estimated for the three samples. For the LS state, variations of 0.01 Å are found in all the thermal range for the three samples. The obtained distributions in the Fe-ligands distances are about one order of magnitude lower than the changes in the Fe-ligands distances associated with the transition between HS and LS states. The detection of such inhomogeneities shows the potentialities of Mössbauer spectroscopy in revealing fine structural details.

Passing to the effective thickness of the samples, considering that t_a is proportional to f, the relation reported for the thermal dependence of f within the Debye model (Eq. 2.5) holds also for t_a. By fitting with Eq. 2.5 the total effective thickness of the samples (the fits are reported in Appendix A), a Debye temperature of 106(8) K and 129(5) K was found for the 50 and 5 nm samples, respectively. These values have the same order of magnitude and are in line with the values reported for **1** molecules in the bulk phase [123, 58]. The similarity of the Debye temperatures and of the slopes of δ vs $\ln t_a$ indicates that the vibrational properties of the molecules are similar in both sublimated samples irrespective of their thickness and therefore not influenced by the substrate. Moreover, no preferential orientation of the molecules in the sublimated samples was evident from the data analysis.

Considering the absorption cross-section of the HS and LS sites, a strong asymmetry is found for the LS state, due to a high correlation between the isomer shift and quadrupole splitting distributions. Similar considerations hold also for the HS state, although the asymmetry is less pronounced. It is also relevant to note that such correlations are similar for both sublimated samples, irrespective of their thickness and are absent in the bulk [123, 58]. This is further confirmed by the fit of the Mössbauer spectra realized at high and low temperature with a standard setup on the powder sample of **1**. The same fitting procedure based on the evaluation of the transmission integral function was used. However, no correlation between δ and Δ was found. The absorption cross-sections of the HS and LS sites result to be symmetric and narrower than those extracted from the fit of the sublimated samples; moreover, they are within

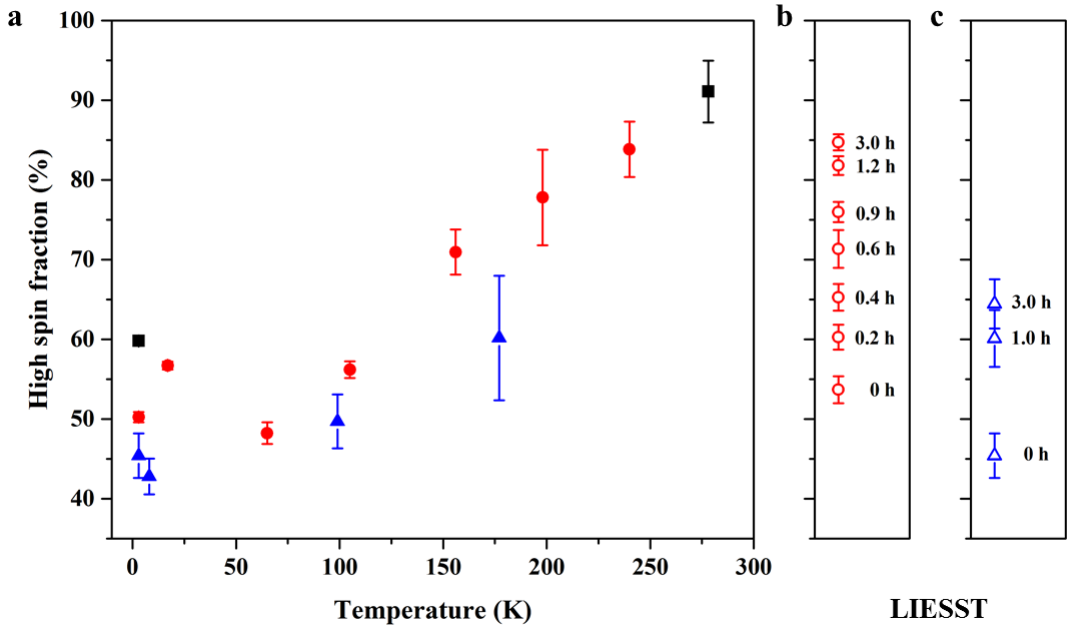

Figure 4.7: HS fraction evaluated from the fit of the Mössbauer spectra. a) %HS as a function of the temperature of the 50 nm thick sublimated sample (red dots), the 5 nm thick sample (blue triangles) and the dropcast sample (black squares). b) %HS after LIEEST of the 50 nm thick sublimated sample for different irradiation times at 6.0 K. c) %HS after LIEEST of the 5 nm thick sublimated sample for different irradiation times at 3.0 K.

the corresponding ones of the sublimated samples. Therefore, the correlation found in the spectra of the sublimated samples is induced by the interaction of the molecules with the surface and indicates a heterogeneity of the crystal field that allows a partial delocalization of electron density on the e_g levels, which ultimately modifies the switching properties. The similarity of the calculated correlation between the 5 nm and 50 nm thick samples indicates that the modifications induced by the substrate propagate up to relevant distances from it. This seems also in line with a minimal thickness, that has been observed, above which the spin switching properties seem to be retained [124], and may be related to the cooperative character of these systems.

Finally, for each sample at each temperature the high spin fraction (%HS) was calculated from the HS and LS absorption cross-sections extracted from the fit of the spectra. The calculated %HS for the three samples is reported in Fig. 4.7.

For the dropcast sample, at high temperature, a minor contribution of the LS state is present, in agreement with measurements realized on microcrystalline powder of **1** [123, 58]. However, at 3.0 K there is still a very high contribution ($\sim$ 60 %) of the HS state. This feature represents a significant difference in the behavior of the molecules

Sample	Time (h)	Site	δ_0(mm/s)	Δ_0(mm/s)	σ(mm/s)	α	%HS
50 nm	0	HS	1.176(7)	2.27(1)	0.351(9)	-0.20(2)	54(2)
		LS	0.436(6)	0.581(7)	0.100(7)	0.5(1)	
	2.5	HS	1.182(2)	2.236(3)	0.298(2)	-0.074(5)	85(1)
		LS	0.462(4)	0.680(9)	0.09(2)	0.7(4)	
5 nm	0	HS	1.03(1)	2.27(3)	0.29(2)	-0.17(5)	45(3)
		LS	0.397(8)	0.485(9)	0.10(1)	0.29(8)	
	3.0	HS	1.079(8)	2.22(2)	0.26(1)	-0.11(3)	64(3)
		LS	0.39(1)	0.49(2)	0.10(1)	0.7(2)	

Table 4.2: Mössbauer parameters of the HS and LS states extracted from the fit of the spectra measured at low temperature before the irradiation (0 h) and at the end of the irradiation. The calculated HS fraction (%HS) is also reported.

deposited on substrate by drop casting with respect to those in the bulk phase, for which a complete conversion from high to low temperature is observed.

For the 50 nm thick sublimated sample, the %HS at 240 K and 3.0 K amounts to 84(3) % and 50.2(6) %, respectively. However, considering the trend of the data with the temperature, these values result comparable with those found for the dropcast sample. Therefore, the efficiency of the thermal SCO transition results to be about 30 % in these samples.

For the 5 nm thick sample, the %HS is 45(3) % at 3.0 K, therefore lower than that observed for the other two samples. At high temperatures, the characterization of the 5 nm thick sample is more difficult due to the decrease of the signal-to-noise ratio of the spectra, which results in the increased uncertainty of the extracted parameters. However, we can observe that in the temperature range between 3.0 K and 177 K about 15 % of the molecules undergo a SCO transition.

The reduced efficiency of the SCO transition in all the investigated samples with respect to molecules in the bulk phase can be ascribed to an effect of the interaction between the molecules and the substrate. This is confirmed by the gradual behavior of the spin transition curve of the 50 nm thick sample, that, as noticed in Section 1.2, may indicate a low degree of cooperativity between the molecules deposited on gold.

4.4.2 LIESST effect

In Fig. 4.4, the best fit curves of the Mössbauer spectra and the absorption cross-sections of the HS and LS sites of the sublimated samples at representative irradiation times are reported. Best fit parameters extracted from the fit of the spectra realized before and at the end of the irradiation are reported in Table 4.2, while the temperature behavior of the hyperfine parameters associated to the HS site is reported in Fig. 4.8.

Interestingly, the broadening of the distribution of the hyperfine parameters of the HS state decreases with the irradiation time, indicating that the irradiation is more selective in populating the excited spin state with respect to the thermal excitation. As

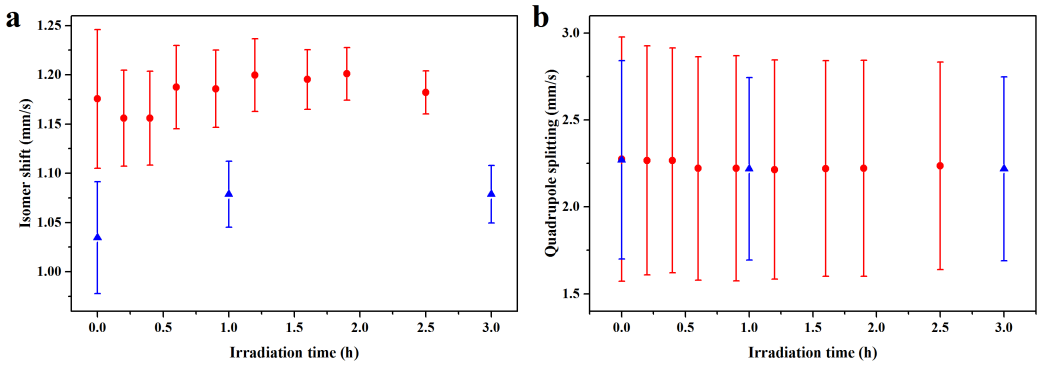

Figure 4.8: Hyperfine parameters of the HS site extracted from the fit of the Mössbauer spectra of the 50 nm thick sample (red dots) and the 5 nm thick sample (blue triangles) as a function of the irradiation time. In each panel the bar represents the distribution of the values around the mean value.

a consequence, the mean values of the hyperfine parameters after 2.5 hours of irradiation show slight changes. This observation is in line with what previously reported for the SCO behavior of **1** on a highly oriented pyrolytic graphite surface [56], analyzed by means of X-ray absorption spectroscopy (XAS): the Fe $L_{2,3}$ x-ray absorption spectra at room temperature and after LIESST at 6 K are quite similar and the differences between the HS spectra were ascribed to the different population of HS states closely spaced in energy. Moreover, this agrees with the observation that irradiation of a single crystal of **1** with 633 nm wavelength radiation at 30 K produces a HS polymorph that is different from the thermally induced one [125].

Finally, the fits confirm the qualitative assessment resulting from a direct inspection of the spectra that for both samples the irradiation with 990 nm wavelength radiation at low temperature promotes a conversion of the molecules from the LS state to the HS one. The %HS calculated from the HS and LS absorption cross-sections extracted from the fit of the spectra is reported in panels b and c of Fig. 4.7 for both sublimated spectra. The increase of the HS component is quick in the first hour of irradiation, while a saturation behavior is recorded for longer irradiation times. From an exponential fit of the data (see Fig. 4.9), characteristic times of 0.74(9) h and 0.71(2) h were found for the 50 nm and 5 nm thick samples, respectively. Moreover, after 2.5 hours of irradiation, the SCO efficiency associated with the LIESST effect in the 50 nm thick sample is about 30 %, comparable with the value due to the thermal excitation. Similar considerations hold for the 5 nm thick sample: after 3.0 hours of irradiation the SCO efficiency amounts to about 20 %. This value is comparable within the error with the thermally induced one.

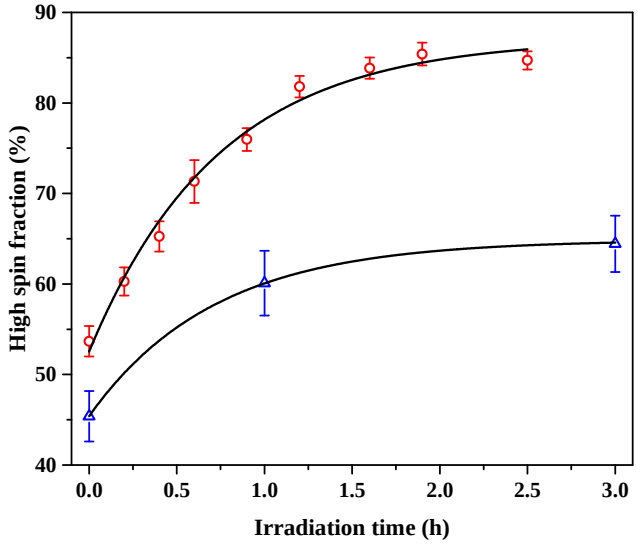

Figure 4.9: HS fraction as a function of the irradiation time evaluated from the fit of the Mössbauer spectra of the 50 nm thick sample (red dots) and the 5 nm thick sample (blue triangles). The black lines represent the fits with an exponential function.

4.5 Conclusions

In conclusion, the SCO efficiency of **1** molecules deposited on a gold substrate was investigated by means of synchrotron Mössbauer spectroscopy.

The SCO transition was studied both by varying the temperature and irradiating the samples at low temperature with radiation of suitable wavelength to induce the LIESST effect. Both measurements show that, once deposited on the gold substrate, the thickness of **1** molecules modifies the efficiency of the SCO mechanism. The SCO efficiency between 278 K and 3.0 K for the thick dropcast sample and the 50 nm thick sublimated one amounts to about 30 %. Because of the worse signal-to-noise ratio, the Mössbauer data of the 5 nm thick sublimated sample are limited to the 177 - 3.0 K range in which a 20 % of spin conversion is achieved. Moreover, for both sublimated samples LIESST measurements show that values of the SCO efficiency comparable to the thermally induced ones can be achieved after about 3.0 hours of irradiation.

Finally, the high resolution and sensitivity of Mössbauer spectroscopy allowed to reveal a correlation between the distributions of the hyperfine parameters of the Fe(II) ions. This translates into distributions of the crystal field of the deposited molecules that correlate with a decreased spin conversion, when submitted to external stimuli, with respect to molecules in the bulk phase. This consideration may indicate the way to follow for the chemical design of the SCO molecules: the Fe-ligand distances have to

be retained when molecules are deposited on surfaces.

Author contributions: Matteo Mannini and Patrick Rosa planned the investigation. Lorenzo Poggini synthesized the material and prepared the samples. Alberto Cini, Lorenzo Poggini, Patrick Rosa and Matteo Mannini performed the experiments with the assistance of Aleksandr Chumakov and Rudolf Rüffer. Mössbauer data were analysed by Alberto Cini, Maria Fittipaldi and Gabriele Spina. Alberto Cini, Maria Fittipaldi and Gabriele Spina wrote the manuscript with contributions from all authors.

Chapter 5

Electric field modulation of magnetic exchange in molecular helices

The detection of a pure spin magnetoelectric effect in molecular helices by means of EPR spectroscopy with an electric field modulation is reported. This study was realized by means of an implementation in the EPR spectrometer of the possibility to apply an electric field on the sample while revealing the EPR absorption. Signals associated with a magnetoelectric coupling between the single crystal and the electric field were detected. This effect is compared with that predicted by *ab initio* calculations.

Manuscript in publication:
"Electric field modulation of magnetic exchange in molecular helices"
M. Fittipaldi, A. Cini, G. Annino, A. Vindigni, A. Caneschi and R. Sessoli, in publication on *Nature Materials*
DOI: 10.1038/s41563-019-0288-5

5.1 Introduction

An open problem for the use of magnetic materials for quantum information processing is the possibility to drive them by means of an electric field rather than a magnetic one. Quantum manipulation in fact requires temporal and spatial scales that are hard to be achieved for a magnetic field. Manipulation on the time scale of 1 ns would require an oscillating magnetic field of the order of 10^{-2} T, which is difficult to achieve [96]. Moreover, for single-molecule addressing a spatial resolution of 1 nm is required, that is also prohibitively small [96]. On the contrary, an electric field would allow a faster, less energy demanding and more space-confined manipulation of the spins.

Considering that the spin does not couple directly to the electric field, this effect can be investigated only in materials where the presence of a particular symmetry or

interaction allows an indirect coupling between them. A spin-electric coupling has been identified in the single molecule magnet Cu_3, that is an equilateral triangle of three antiferromagnetically coupled $s = 1/2$ spins [96]. In this system the coupling is based on an interplay of spin exchange, spin-orbit interaction and lack of inversion symmetry. In particular, the low-energy states exhibit a chiral spin texture and, due to the absence of inversion symmetry, electric fields couple states of opposite chirality; moreover, spin-orbit interaction couples the chirality to the total spin and thus an effective spin-electric interaction eventually emerges [96]. Analogous symmetry arguments are expected to apply to other molecular magnets that lack inversion symmetry. For example, the role of chirality to allow spin-electric coupling has been investigated in Dy_3 [126].

A widely investigated class of materials, where the effect of electric field on magnetism is studied, are multiferroic materials [127, 128, 129]. Multiferroics are materials that combine two or more ferroic orders, such as ferromagnetism, ferroelectricity and ferroelasticity. A ferromagnet is a material with a spontaneous magnetization that is switchable by an applied magnetic field, a ferroelectric is a material with a spontaneous electric polarization that is switchable by an applied electric field and in a ferroelastic material a spontaneous deformation is switchable by an applied stress. The appealing kind of multiferroics are those that combine ferromagnetism and ferroelectricity, because the coupling between magnetization and electric polarization enables the magnetoelectric effect, that is the possibility to induce or modify the magnetization by varying the electric field or modify the electric polarization by varying the magnetic field.

It is worth noting that multiferroics are not the only class of materials exhibiting the magnetoelectric effect. The magnetoelectric behavior of a material in fact is associated with its magnetic point group symmetry [130]. For example, the presence of a linear magnetoelectric effect is predicted in systems where both time-reversal and space-inversion symmetries are broken [131]. Spin-orbit coupling is generally considered another necessary ingredient to make the spin system sensitive to the charge distribution [128, 132]. On the contrary, a pure spin magnetoelectric effect, i.e. not associated with spin-orbit coupling, would be extremely appealing in the emerging field of quantum materials [131], since orbital degrees of freedom induce coupling to the environment, which results in spin decoherence [132].

Here a pure spin magnetoelectric effect was detected in molecular helices by means of EPR spectroscopy with an electric field modulation. This effect is shown to be dependent on the modulation of the magnetic exchange interaction.

5.2 MnPhOMe

The magnetoelectric effect was investigated in the molecular helicoidal chain MnPhOMe, that is isostructural to the single chain magnet CoPhOMe introduced in Section 1.1.3.2.

MnPhOMe is a one-dimensional molecular chain containing Mn(II) ions shielded by ancillary ligands ($hfac^-$= hexafluoroacetylacetonato) and bridged by stable nitronyl-nitroxide organic radicals (NITPhOMe = 2-(4-methoxyphenyl)- 4,4,5,5-tetramethylimi

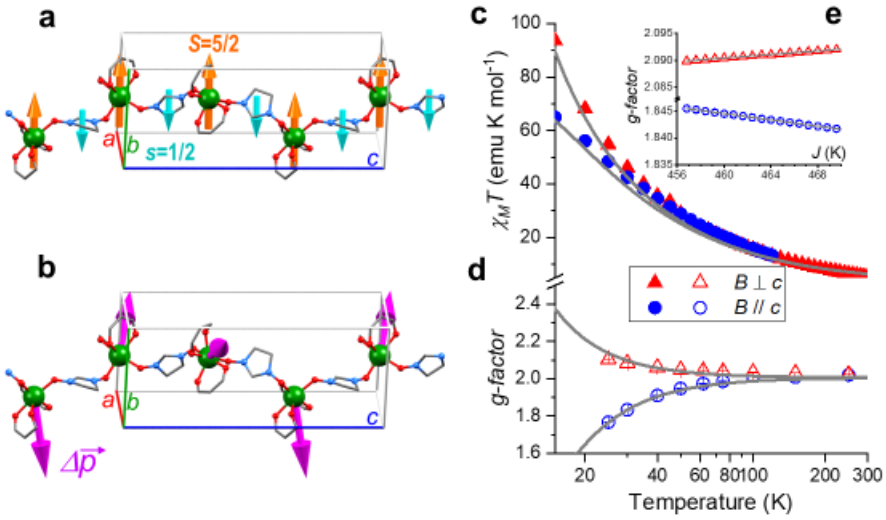

Figure 5.1: Structure and magnetic properties of the MnPhOMe molecular helices. a) Crystal structure of MnPhOMe (colour code: Mn atoms in green, O in red, N in blue, C in gray, H atoms, CF_3, CH_3, $C_6H_5OCH_3$ groups omitted for clarity). Orange and cyan arrows represent the ferrimagnetic arrangement of Mn and radical spins. b) On the same structure of (a) the vectors representing the change in electric dipole moments when neighbouring spins are brought from antiparallel to parallel alignment are reported, as calculated in [45]. c) The product of temperature and magnetic susceptibility (χT) of oriented MnPhOMe crystals measured parallel (circles) and perpendicular (triangles) to the crystallographic axis **c**; continuous lines are the simulations. d) Effective g values extracted from single crystal EPR spectra as a function of the temperature with the magnetic field applied parallel and perpendicular to the chain axis (empty symbols with same colour code as in panel (c)). The solid lines are the simulations with Eq. 5.4. e) Calculated dependence of the effective g values on the exchange coupling constant at 30 K.

dazoline-l-oxyl,3-oxide), which crystallizes either in the chiral $P3_1$ or $P3_2$ space groups, forming a helical structure [133].

The chain is characterized by a strong intrachain antiferromagnetic exchange interaction between the spin $S_{Mn} = 5/2$ of the Mn(II) ion and the spin $S_{rad} = 1/2$ of the organic radical (see Fig. 5.1a). Interchain interactions are minimized by the bulky organic ligands and onset of 3D magnetic order only occurs at very low temperature ($<$ 10 K) [133].

Due to its helical structure and its crystallization in an acentric space group, there are no symmetry constraints forbidding the development of an electric polarization or the observation of magnetochiral effects in MnPhOMe [45, 46]. Recent *ab initio* calculations suggested a novel type of magnetoelectric effect in this compound [45]. Modification from antiparallel to parallel alignment of neighbouring spins in fact induces

a change in the net electric dipole moment along the axis of the helix (see Fig. 5.1b), which is not related to structural changes and is independent on spin-orbit coupling. From density functional theory (DFT) calculations the change in polarization along the chain axis **c** is estimated in the range (600 - 800) μC/m^2; the value depends on the specific parameters used to describe the on-site Coulomb repulsion and on-site exchange correction [45]. Moreover, the change in polarization $\mathbf{\Delta P}$ has been found to vary as the cosine of the angle formed by the Mn and radical spins

$$\mathbf{\Delta P} = k_{ME} \left(\mathbf{S}_{Mn} \cdot \mathbf{S}_{rad} \right) \frac{\mathbf{c}}{c} \tag{5.1}$$

where k_{ME} is the magnetoelectric coupling, the sign of which depends on the chirality of the crystal ($P3_1$ or $P3_2$).

In Fig. 5.1c, the product of temperature and magnetic susceptibility (χT) of Mn-PhOMe crystals, measured parallel and perpendicular to chain axis **c**, are reported. On decreasing the temperature, the observed divergence is indicative of the onset of intrachain short-range magnetic correlation. The magnetic susceptibility data were calculated using the transfer-matrix approach [134] and assuming a Heisenberg intrachain exchange interaction acting between neighboring Mn and radical spins

$$H_{exc} = J \sum \mathbf{S}_{Mn} \cdot \mathbf{S}_{rad} \tag{5.2}$$

where J is the exchange coupling constant and the summation is extended over all nearest neighboring spins in the chain. An additional anisotropic component was added to the exchange Mn-radical coupling to account for their reciprocal dipolar interaction

$$H_{dip} = J_d \sum \left(\mathbf{S}_{Mn,x} \cdot \mathbf{S}_{rad,x} + \mathbf{S}_{Mn,y} \cdot \mathbf{S}_{rad,y} - 2\mathbf{S}_{Mn,z} \cdot \mathbf{S}_{rad,z} \right) \tag{5.3}$$

An analogue term was also considered in order to account for dipole-dipole interaction between neighbouring Mn-Mn pairs belonging to the same spin chain. The spin $S_{rad} = 1/2$ of each radical unit was treated quantum-mechanically, while the spin $S_{Mn} = 5/2$ of each Mn was treated as a classical spin. The only adjustable parameter of the model was, thus, J in Eq. 5.2. As shown in Fig. 5.1c, the experimental susceptibility is well reproduced by choosing $J = 460$ K. This value compares well with DFT estimates [45] and with the values previously reported for this class of spin chains [133].

In spin chains, which behave in agreement with the model described above, the combination of exchange-induced spin correlation and the anisotropy of dipolar interaction (see Eq. 5.3) gives rise to a shift of the EPR absorption as the temperature is lowered, according to a well-known phenomenon called g-shift [135]. This phenomenon is described quantitatively by the simple relation [136]

$$g^{\alpha}_{eff} = g_0 \frac{\chi^{\alpha}}{\sqrt{\chi^{\beta}\chi^{\gamma}}} \tag{5.4}$$

where the apexes indicate permutation of the crystallographic directions ($\alpha = \beta = \perp$ and $\gamma = \parallel$ in the trigonal system). The use of Eq. 5.4, employing the calculated susceptibilities without any adjustable parameter, well reproduces the effective g values

extracted from single crystal X-band EPR spectra acquired with the external magnetic field parallel and perpendicular to the **c** axis of the crystal (see Fig. 5.1d).

A question of high relevance is whether the theoretically predicted interplay between spin orientation, chirality and electric polarization may lead to the control of the magnetic properties of the system by applying an external electric field. Combining Eq. 5.2 with Eq. 5.1, one immediately sees that an applied electric field **E** modifies the exchange contribution to the spin Hamiltonian as follows

$$H_{exc}^{eff} = J\sum \mathbf{S}_{Mn}\cdot\mathbf{S}_{rad} - \sum \mathbf{E}\cdot < \Delta\mathbf{p} >= \left(J - k'_{ME}E_c\right)\sum \mathbf{S}_{Mn}\cdot\mathbf{S}_{rad} \qquad (5.5)$$

where $< \Delta\mathbf{p} >$ is the change of the electric dipole moment of a Mn-radical pair averaged over the three sites of the unit cell and $k'_{ME} = k_{ME}V$, where V is the volume of a Mn-radical pair. Only the component of **E** along **c** (E_c) enters in Eq. 5.5 because $< \Delta\mathbf{p} >$ is parallel to **c** for the symmetry of the system. In other words, this magnetoelectric coupling can be taken into account as a modification of the effective exchange interaction that depends linearly on E_c. The sign of this magnetoelectric contribution depends on the direction of **E** with respect to **c** and on the chirality of the helices [45]. By virtue of Eq. 5.4, the g values are expected to reflect the variation of the exchange interaction J on the spin correlation, indeed with a linear dependence on J, as numerically evaluated and reported in Fig. 5.1e. This makes EPR spectroscopy a suitable tool to detect the proposed magnetoelectric effect.

5.3 Electric field modulated EPR

In order to study the magnetoelectric effect in a single crystal of MnPhOMe, EPR spectra were acquired during the application of an electric field on the sample. As noticed in Section 2.2.5, the investigation of electric field effects by means of EPR spectroscopy has been widely used to study the symmetry of crystal field of metal ions [87] and, more recently, to assess the possibility to use the electric field to manipulate the spin states towards quantum information processing [94, 95]. All these experiments were realized by taking advantage of a method based on the observation of electron spin echoes in pulsed EPR [93, 91].

We used instead a seldom employed method based on continuous wave EPR spectroscopy with electric field modulation [97, 98]. The experiment is similar to a normal EPR experiment, where, instead of modulating the static magnetic field, the position of the resonance line is modulated by the electric field. Thanks to the phase-sensitive detection of this electric field modulated (EFM) EPR, a derivative signal becomes visible if the electric field affects the magnetic field at which resonance occurs, i.e. a magnetoelectric coupling is active.

Continuous EFM-EPR spectra were acquired at X-band on a single homochiral crystal of MnPhOMe subject to an oscillating electric field ($\mathbf{E}_m$). The long wavelength $\mathbf{E}_m$ was introduced in the comparatively small X-band cavity by means of a cutoff-less propagating structure given by two thin parallel conducting wires distant $\sim$ 1

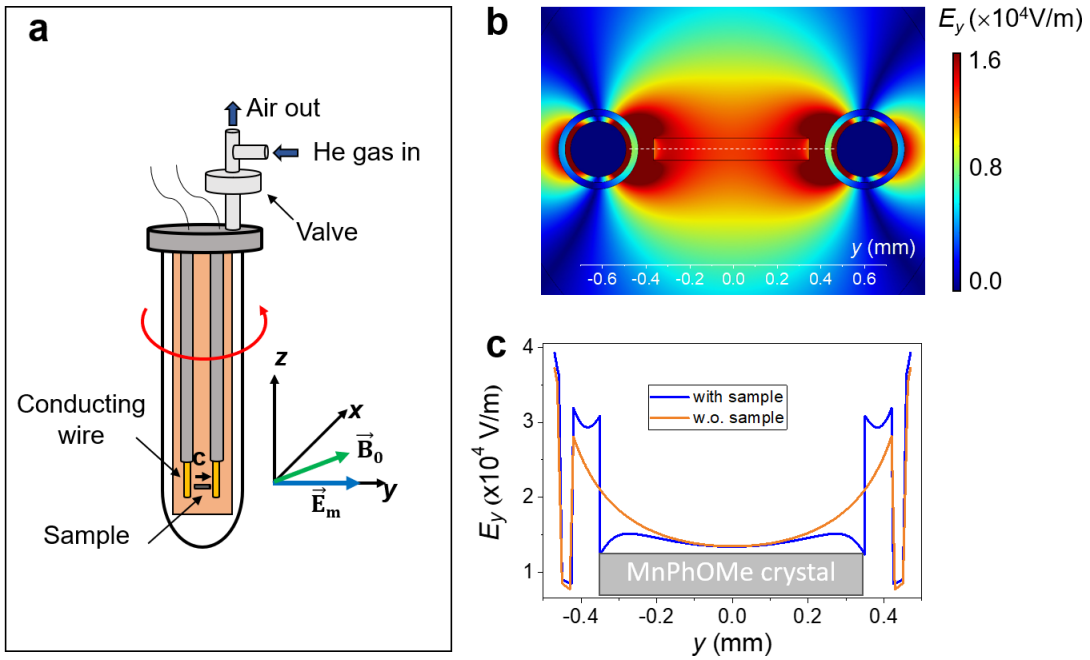

Figure 5.2: Experimental setup for electric field modulated (EFM) EPR. a) Schematic view of the modified version of the sample holder used for the EFM-EPR and EPR measurements. The orientations of the crystal axis **c**, the static magnetic field $\mathbf{B}_0$ and the applied electric field $\mathbf{E}_m$ are shown. b) Numerical simulation of the electric field component along the direction connecting the wires in the sample plane. c) Rigorous numerical simulation along the dashed white line of panel (b) in the absence of the sample (orange line) compared to the case with the sample (blue line).

mm, following a concept successfully demonstrated in high-frequency dynamic nuclear polarization [137, 138].

In particular, the measurements were realized by taking advantage of a modified version of the standard sample holder used in EPR (see Fig. 5.2a). Inside the standard pirex tube (external diameter 4 mm and internal diameter 3 mm), two kapton insulated manganin wires with a diameter of 250 μm were introduced to act as electrodes. The wires were arranged on a kapton foil, parallel to each other at a relative distance of about 1 mm. The sample was mounted between the wires, which were insulated by means of quartz capillaries. After mounting the sample, the tube was filled with He gas and sealed. The electrodes were connected to an alternating voltage $V = V_0 \cos(\omega t)$, with $V_0 = 16.5$ V and $\omega = 30$ kHz directly coming from the cw EPR instrument, which normally is fed into the modulation coils. An acceptable $\mathbf{E}_m$ homogeneity over the crystal volume was expected (see Fig. 5.2b), also thanks to the polarization charge induced on the sample. A comparison between the simulations of the $\mathbf{E}_m$ component

along the direction connecting the wires in the sample plane realized with and without the sample placed between the wires (see Fig. 5.1c) shows that the crystal reduces the electric field in proximity of the surfaces with a substantial reduction of the electric field inhomogeneity over the sample.

The EPR and EFM-EPR measurements were realized with a standard cw EPR spectrometer. A phase-sensitive detection of both signals was realized. The EFM-EPR spectra were acquired with 1000 times higher microwave power with respect to the EPR spectra. The cw EPR spectra of MnPhOMe were acquired by switching from the electric field modulation to the conventional magnetic one.

Both standard EPR spectra and EFM-EPR spectra were recorded at different temperatures and different mutual orientations of the crystal axis **c**, the slowly scanned magnetic field $\mathbf{B}_0$ and, when applied, the $\mathbf{E}_m$ field, as schematized in Fig. 5.2a.

5.4 Experimental results

In the top panels of Fig. 5.3a and b, the EPR spectra measured at 30 K on a single crystal of MnPhOMe are shown. The spectrum measured with $\mathbf{B}_0 \parallel \mathbf{c}$ shows a resonance field (B_{res}) around 3700 G and a linewidth of about 500 G. In the spectrum measured with $\mathbf{B}_0 \perp \mathbf{c}$, a lower B_{res} occurs (3200 G) and the linewidth is narrower (200 G). In both cases, the narrow signal visible at about 3360 G is associated with minimal free radical impurities, always present in these compounds.

In the bottom panels of Fig. 5.3a and b, the EFM-EPR spectra are reported as acquired at 30 K and at the same two orientations of the EPR spectra and applying $\mathbf{E}_m$ parallel to **c**. Interestingly, the center of both spectra results to be shifted with respect to the center of the corresponding EPR signals. Moreover, the direction of this shift depends on the relative orientation between $\mathbf{B}_0$ and **c**: for $\mathbf{B}_0 \parallel \mathbf{c}$ the spectrum is shifted towards a higher field, while for $\mathbf{B}_0 \perp \mathbf{c}$ the spectrum is shifted towards a lower value of the magnetic field with respect to the corresponding EPR spectrum. Also the phase of the EFM-EPR derivative spectra depends on the relative orientation between $\mathbf{B}_0$ and **c**. Moreover, both EFM-EPR spectra show a marked asymmetry with respect to the EPR spectra, while the linewidth of the EFM-EPR spectrum is broader when $\mathbf{B}_0$ is along **c**, as for the corresponding EPR spectrum. Finally, no trace of the narrow signal due to the radical impurity is detected in the EFM-EPR spectra: this is a first proof that the signal is due to the modulation of the electric field and not to any induced small alternated magnetic field. The shape of the EFM-EPR spectra was unmodified and the radical impurity seen in the EPR spectra remained undetected by acquiring the spectra with reduced microwave power (see Appendix B).

In Fig. 5.3c, the spectra acquired at 30 K with $\mathbf{B}_0 \perp \mathbf{c}$ after a 180° rotation of the crystal axis, so that **c** and $\mathbf{E}_m$ had opposite directions are shown. While the EPR spectrum is unchanged, the EFM-EPR spectrum inverted its phase. The same result is obtained by inverting the polarity of the electrodes (see Fig. 5.4). The phase reversal of the EFM-EPR signal after changing the relative sign between **c** and $\mathbf{E}_m$ was verified

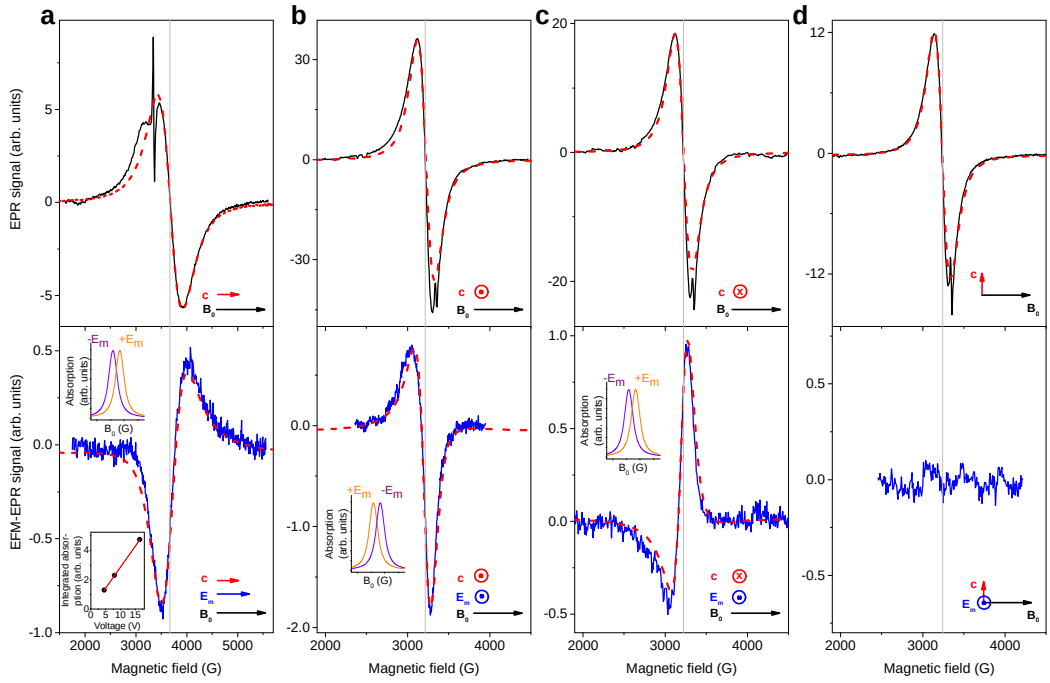

Figure 5.3: EPR spectra (top panel, black lines) and EFM-EPR spectra (bottom panel, blue lines) acquired at 30 K: $\mathbf{B}_0 \parallel \mathbf{c}$ (a) and $\mathbf{B}_0 \perp \mathbf{c}$ (b) with $\mathbf{E}_m$ and $\mathbf{c}$ pointing towards the same direction; $\mathbf{B}_0 \perp \mathbf{c}$ after reversing the crystal direction so that $\mathbf{E}_m$ and $\mathbf{c}$ point towards opposite directions (c); $\mathbf{B}_0 \perp \mathbf{c}$ and $\mathbf{E}_m \perp \mathbf{c}$ (d). The EFM-EPR spectra were acquired with 1000 times higher microwave power with respect to the EPR spectra. The phase of the signal correlates to the shift of the resonance lines for positive and negative values of $\mathbf{E}_m$, as schematized by orange and purple lines, respectively. Dash red lines represent the simulations of the spectra realized with the model given by Eq. 5.7. In the inset, the intensity of the EFM-EPR spectra (evaluated as the integral of the EFM-EPR absorption) is reported as a function of the applied voltage.

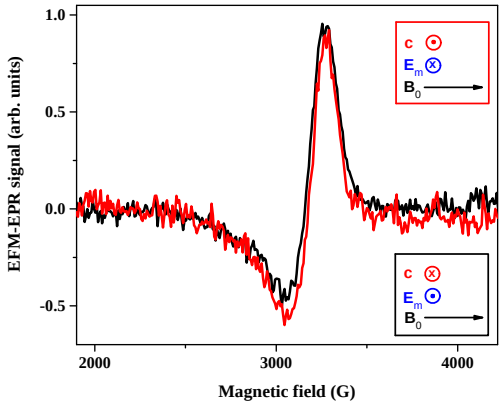

Figure 5.4: Comparison between the EFM-EPR spectra acquired at 30 K with $\mathbf{B}_0 \perp \mathbf{c}$ after reversing the crystal direction, so that $\mathbf{E}_m$ and $\mathbf{c}$ point towards opposite directions, (black line) and after inverting the polarity of the electrodes (red line) with respect to the conditions of the spectrum of Fig. 5.3b.

also in the $\mathbf{B}_0 \parallel \mathbf{c}$ configuration (see Appendix B).

The final proof that the observed signals are a genuine electric field effect and not induced by a spurious modulated magnetic field is reported in Fig. 5.3d, where the spectra were acquired at 30 K with $\mathbf{B}_0 \perp \mathbf{c}$ and $\mathbf{E}_m \perp \mathbf{c}$. In this case any spurious magnetic field induced by $\mathbf{E}_m$ would remain parallel to $\mathbf{B}_0$, thus a comparable signal should be observed. However, no EFM-EPR signal is detected when $\mathbf{E}_m$ is applied perpendicular to $\mathbf{c}$, in agreement with the predicted absence of spin-induced electric polarization in the **ab** plane of the MnPhOMe crystal.

Our observations are well rationalized considering the effect that an oscillating electric field has on the effective exchange constant of Eq. 5.2. The phase-sensitive detection results in fact in a signal that can be seen as the difference in the absorption corresponding to $+\mathbf{E}_m$ and that corresponding to $-\mathbf{E}_m$, as indicated in the insets in the bottom parts of Fig. 5.3. The sign of the first derivative signal thus depends on how the g value (or the resonance field) varies with J.

According to this hypothesis, a similar effect should be observed also in presence of a static electric field. The difference on the standard EPR spectrum induced applying an electric field of 10^6 V/m with respect to that acquired with the electric field off is reported in Appendix B. The signal is very noisy, but a weak feature compatible with the magnetoelectric effect is visible after a temperature drift correction. The superior sensitivity of the approach based on the electric field modulation is thus clear.

In order to characterize further this magnetoelectric coupling, the EFM-EPR measurements were realized by applying different values of the amplitude of the electric field (the spectra are reported in Appendix B). In the inset of the bottom panel of Fig. 5.3a,

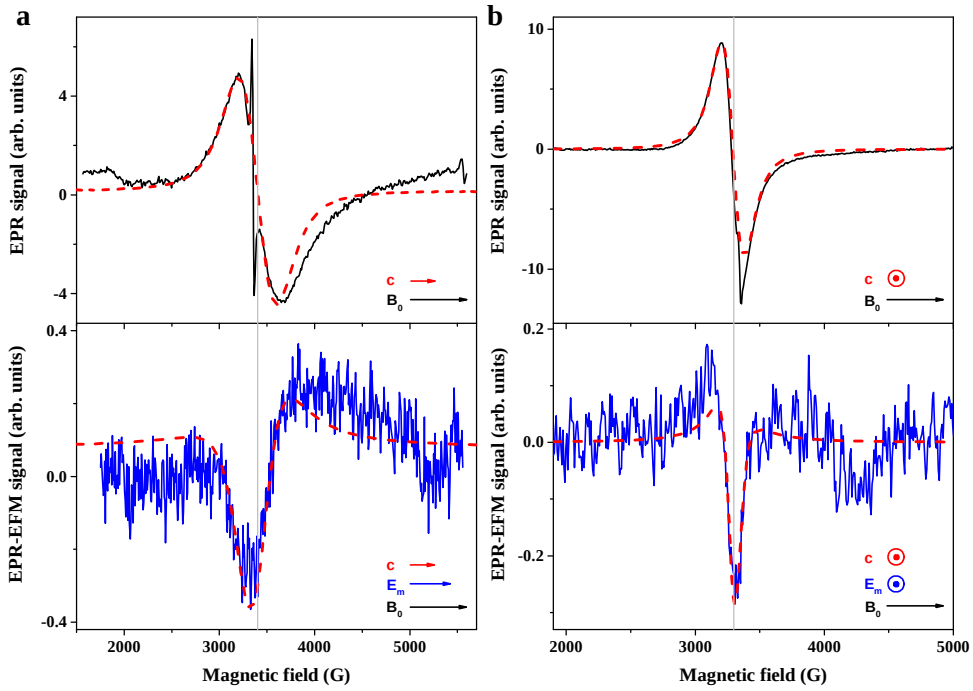

Figure 5.5: EPR spectra (top panel, black lines) and EFM-EPR spectra (bottom panel, blue lines) acquired at 50 K: $\mathbf{B}_0 \parallel \mathbf{c}$ (a) and $\mathbf{B}_0 \perp \mathbf{c}$ (b) with $\mathbf{E}_m$ and $\mathbf{c}$ pointing towards the same direction. The EFM-EPR spectra were acquired with 1000 times higher microwave power with respect to the EPR spectra. Dash red lines represent the simulations of the spectra realized with the model given by Eq. 5.7.

the intensity of the EFM-EPR spectra (evaluated as the integral of the EFM-EPR absorption) is reported as a function of the applied voltage: the intensity of the EFM-EPR spectra has a linear dependence on the applied electric field.

In Fig. 5.5, the EPR and EFM-EPR spectra acquired at 50 K in the $\mathbf{B}_0 \parallel \mathbf{c}$ and $\mathbf{B}_0 \perp \mathbf{c}$ configurations are reported. The center of the EPR spectra is shifted with respect to the spectra acquired at 30 K, as expected because of the g-shift induced by the temperature in the MnPhOMe crystal. Consequently, the EFM-EPR spectra are shifted with respect to the spectra registered at 30 K. However, the same features (direction of the shift, asymmetry and phase) as a function of the relative orientation between $\mathbf{B}_0$ and $\mathbf{c}$ are encountered. Furthermore, the increase of the temperature strongly reduces the intensity of the signal. At 100 K, the EFM effect becomes undetectable.

$\mathbf{B}_0$,**c**	SIGNAL	g	Γ (G)	B_m^{eq} (G) ($\times 10^{-3}$)	Δg_E ($\times 10^{-6}$)	$\Delta\Gamma$ (G)	α ($\times 10^{-6}$)
$\parallel$	EPR	1.818(7)	494(4)				
	EFM-EPR		494(4)	5.1(9)	−2.5(4)	80	4(1)
$\perp$	EPR	2.103(12)	224(13)				
	EFM-EPR		179(9)	1.7(4)	1.1(3)	26	5(2)

Table 5.1: Averaged values of the parameters used to simulate the EPR and EFM-EPR spectra at 30 K obtained from the simulations of spectra taken on three different crystals. In the EFM-EPR spectra $\mathbf{E}_m$ and **c** are pointing to the same direction.

5.5 Simulations of the spectra

Simulations of the EFM-EPR spectra would require taking into account in the resonance phenomenon the time-dependence of the spin Hamiltonian parameters induced by the ac electric field. This is not possible for such a complex extended system, but an immediate insight into the physics of the system can be gained by simulating the spectra as an $S = 2$ spin (originating from the strong antiferromagnetic interaction between neighbouring Mn(II) and radical spins) with an axial g tensor. Moreover, at each orientation, the linewidth (Γ) of the EPR spectrum resulted to be a combination of a Gaussian and a Lorentzian broadening. Therefore, the EPR spectrum is characterized by an inhomogeneous broadening, whose extent depends on the relative orientation between $\mathbf{B}_0$ and **c**. In other words the EPR signal can be considered as the superposition of homogeneous signals originated from different spin packets, resonating at different magnetic field values within the inhomogeneous broadened line. For the modulation of the magnetic field (B_m) the value used in the acquisition of the EPR spectra (2 G) was used. The simulations of the spectra were realized with Easyspin [139].

The simulations of the EPR spectra realized at 30 K and 50 K are reported in Fig. 5.3 and 5.5, respectively, while the averaged values of the parameters g and Γ obtained from the simulations of spectra taken at 30 K on three different crystals are listed in Table 5.1 (individual sets are listed in Appendix B). Considering the EPR spectra realized at 30 K, the agreement between the simulation and the spectrum is quite good, except in proximity of the signal associated with the radical, which however was not simulated. At 50 K, both the values of g and Γ are reduced with respect to the values used at 30 K.

Passing to the EFM-EPR spectra, the first simulations were realized considering the same values of the parameters found for the EPR spectra and a different value of the modulation field. In particular, the parameter B_m^{eq} was defined as the equivalent ac magnetic field that would be required to reproduce the EFM-EPR intensity as if both spectra (EFM-EPR and EPR) were magnetic-field-modulated. Therefore, the EFM-EPR spectra (y'_{EFM}) were simulated by

$$y^{'}_{EFM} = \pm \frac{B^{eq}_{m}}{B_m} y^{'}_{EPR} \tag{5.6}$$

where $y^{'}_{EPR}$ is the simulation of the EPR spectrum, since the EPR signal is linear with the modulating magnetic field [140]. The value of B^{eq}_{m} was chosen such as that reproducing the intensity of the experimental spectrum. The sign in Eq. 5.6 was chosen in order to give the proper phase of the EFM-EPR spectrum.

The simulations realized with this model qualitatively reproduced the experimental spectra (see Appendix B). However they failed to represent the correct shift of the center of the spectrum, as well as the spectrum asymmetry, observed in the EFM-EPR spectra with respect to the EPR signals.

Very good simulations of the EFM-EPR spectra were achieved by taking into account that also the electric field modulation of the linewidth is possible, as in the low temperature regime ($T \ll J$) the EPR linewidth Γ is expected to increase with J [141], independently of the orientation of $\mathbf{B}_0$. This modulation of the linewidth is not a common feature in EPR, therefore it is not included in the simulation procedure. In order to account for it a second derivative spectrum contribution ($y^{''}_{EPR}$) was added to the principal one as

$$y^{'}_{EFM} = \alpha y^{''}_{EPR} \pm \frac{B^{eq}_{m}}{B_m} y^{'}_{EPR} \tag{5.7}$$

where α is an adjustable proportionality constant. $y^{''}_{EPR}$ was simulated as the difference between two absorption lines having the same center (equal to the center of $y^{'}_{EPR}$) and different linewidth. In particular a line had a width Γ, while the second line was $\Delta\Gamma$ broader. A schematic representation of the simulation procedure described by Eq. 5.7 is reported in Appendix B. The value of α was chosen in order to represent the correct center and asymmetry of the EFM-EPR spectra. It is worth noting that the value of α depends on the value of $\Delta\Gamma$ used (see Appendix B); moreover, $\Delta\Gamma$ is roughly linearly dependent on the amplitude of the electric field (see Appendix B).

The simulations of the EFM-EPR spectra realized at 30 K are reported in the bottom panels of Fig. 5.3, while the averaged parameters obtained from the simulations of spectra taken on three different crystals are listed in Table 5.1 (individual sets are listed in Appendix B). For both configurations ($\mathbf{B}_0 \parallel \mathbf{c}$ and $\mathbf{B}_0 \perp \mathbf{c}$) the model given by Eq. 5.7 gives a good representation of the features of the EFM-EPR spectra, as far as their intensity, shift with respect to the corresponding EPR spectra and asymmetry are conserved. Similar results hold for the EFM-EPR spectra acquired at 50 K (bottom panels of Fig. 5.5). Finally, the simulations confirm that reversing the relative orientation of $\mathbf{c}$ and $\mathbf{E}_m$ only changes the phase of the spectrum (that is simulated with a negative value of α and a negative sign of the second term in Eq. 5.7), but does not shift its center.

5.6 Discussion

The parameters extracted from the simulations of the EFM-EPR spectra allow to quantify the relative shift of the g value of each spin packet induced by $\mathbf{E}_m$ pointing towards $\mathbf{c}$. In particular, it can be estimated by comparing the intensities of the EFM-EPR and EPR signals according to the relation

$$\mid \Delta g_E \mid = \frac{B_m^{eq}}{B_{res}} g \tag{5.8}$$

The $\mid \Delta g_E \mid$ calculated for each EFM-EPR spectrum are reported in Table 5.1. The value of $\mid \Delta g_E \mid$ is of the order of 10^{-6} and it is larger for $\mathbf{B}_0 \parallel \mathbf{c}$ than for $\mathbf{B}_0 \perp \mathbf{c}$. The sign of Δg_E is obtained from the phase of the EFM-EPR spectrum.

Given the over-simplification of the model, the electric field dependent parameters reported in Table 5.1 must be considered as an estimate. However they can be used to roughly quantify the observed magnetoelectric coupling and compare it with the effect predicted by DFT calculations.

Taking into account the linear dependence of g_{eff}^{α} on J given by Eq. 5.4 (the values of the slopes in Fig. 5.1e are $\frac{\Delta g_{eff}^{\parallel}}{\Delta J} = -2.92 \times 10^{-4}$ K^{-1} and $\frac{\Delta g_{eff}^{\perp}}{\Delta J} = 1.66 \times 10^{-4}$ K^{-1} for $\mathbf{B}_0 \parallel \mathbf{c}$ and $\mathbf{B}_0 \perp \mathbf{c}$, respectively) and the $\mid \Delta g_E \mid$ values calculated from Eq. 5.8, the variation ΔJ induced by the application of an electric field of 15 kV/m results to be in the range (0.7 - 0.9)$\times 10^{-2}$ K. Therefore, the magnetic energy cost to rearrange neighbouring spins from antiparallel to parallel $\Delta E_M = -2 S_{Mn} S_{rad} \Delta J$ is of the order of 10^{-2} K. This value can be interpreted as an evaluation of the observed magnetoelectric effect.

In order to compare this experimentally detected magnetoelectric effect with the effect predicted by *ab initio* calculations, we can consider that the same spin reversal originates a change in the electric polarization that in an external electric field introduces an energy contribution (see Eq. 5.5) $\Delta E_E = -\mathbf{E} \cdot < \Delta \mathbf{p} >$. With the same electric field of 15 kV/m and the change in polarization predicted by DFT calculations, an energy value of 10^{-3} K can be evaluated. Considering the simplicity of the model used to simulate the EFM-EPR spectra and the accuracy of DFT calculations, the agreement between the two evaluated energies may be considered acceptable.

5.7 Conclusions

Our detailed analysis of the EFM-EPR of a molecular helix has unambiguously revealed a novel magnetoelectric coupling fully compatible with an electric field modulation of magnetic exchange. The phenomenon has a pure spin origin, thus compatible with the long quantum coherence required for spin-based quantum technologies. Despite the current interest in spin chains [142, 143], the present material does not allow easy processing and isolation of individual chains on surface. The latter are highly desirable, because the application of a much stronger electric field, e.g. that generated by the tip

of a scanning tunnel microscope, than that employed in our investigations could allow an active control of the exchange interaction. Chiral 1D nanostructures are however achievable exploiting biomimetic approaches, such as DNA origami [144], and indeed peptide-based spin platforms have recently been proposed for quantum computation [145].

The EFM cw EPR implemented in our commercial spectrometer results to be a readily accessible and sensitive technique, also able to investigate concentrated systems for which echo-detected EPR is not viable, yet. Its wide diffusion is expected to provide a significant amount of experimental data to be compared with theoretical predictions allowing the understanding of the ingredients that govern magnetoelectric coupling. This should lead, in a close future, to an efficient engineering of novel magnetoelectric molecular materials of high relevance for quantum information technologies.

Author contributions: M.F. and R.S. conceived the research. A.Ca. synthesized the materials and grew the crystals. M.F. and G.A. designed the EFM-EPR setup with assistance of A.V. G.A. simulated the electric field distribution. A.Ci. and M.F. recorded and simulated the EPR spectra, R.S. collected and analysed the magnetic data with assistance of A.V. A.V. realized the magnetic susceptibility calculations. M.F., R.S. and A.Ci. wrote the manuscript with contributions from all authors.

Chapter 6

EPR study of small magnetic nanoparticles

Magnetic nanoparticles (MNPs) of spinel type iron oxide (of approximately 4 nm) mineralized inside the internal cavity of a mini ferritin-type protein were investigated by means of electron paramagnetic resonance (EPR) spectroscopy. EPR measurements were recorded at different temperatures in the perpendicular and parallel configurations. The spectra were interpreted using an approach based on the giant spin model. The quantum behavior of the MNPs is confirmed; moreover, the thermal evolution of the spin system in terms of the population of excited spin states is shown.

This study has been published:
"An EPR Study of Small Magnetic Nanoparticles"
A. Cini, P. Ceci, E. Falvo, D. Gatteschi and M. Fittipaldi, *Z. Phys. Chem.* **231**(4), 745-757 (2017)
DOI: 10.1515/zpch-2016-0846

6.1 Introduction

As already noted in Section 1.4, magnetic nanoparticles (MNPs) and molecular nanomagnets (MNMs) are approaching similar size, with a comparable number of metal ions contained inside them of the order of 10^2 [16]. However, while MNMs are obtained by a bottom-up approach and described by means of quantum mechanics (in particular their features are described by the spin Hamiltonian of the system), MNPs are obtained by a top-down approach and theoretically described using classical mechanics, with the parameters derived from bulk materials. Moreover, for small MNPs (dimensions less than 5 nm) the emergence of new properties associated with the coexistence of classical and quantum behaviors are expected [26]. Consequently, a unified description of the two magnetic nanomaterials is strongly recommended [16]. Evidence in this direction has been provided by EPR studies [17, 18, 19, 20]. In particular, signatures of the discrete

Parameter	Value
Average diameter	3.4 nm
Number of Fe ions	~ 400
Density (ρ)	~ 5 g/cm^3
Saturation magnetization (M_s)	59.7 emu/g
Anisotropy field (B_a)	0.3 T

Table 6.1: Values of the parameters characterizing the MNPs mineralized in the Dps protein. For ρ the value relative to maghemite/magnetite is assumed. M_S and B_a were extracted from magnetic measurements [17].

nature of the energy levels in the MNPs have emerged, displaying the quantum nature of the system.

In order to study the quantum nature of the MNPs, small MNPs were investigated by means of EPR spectroscopy. The EPR measurements were realized both in the standard perpendicular configuration and in the parallel one in order to probe different selection rules, as discussed in the introduction on the principles of EPR spectroscopy (see Section 2.2.1). Finally, the spectra were interpreted using an approach based on the giant spin model.

6.2 Magnetic nanoparticles

Small MNPs of spinel type iron oxide mineralized in the internal cavity of the Dps protein (a protein belonging to the ferritin family) were investigated.

The Dps protein from *Listeria innocua* (LiDps) was used as a protein cage system that differs from ferritins in its smaller size (9 nm outer and 4.5 nm inner diameter as compared to 12 and 8 nm, respectively). The size and the iron oxide phase of the MNPs thus formed inside the Dps protein was controlled using a previously exploited approach [17]. The MNPs have an average diameter of 3.4 nm; a standard deviation of 1.0 nm around this value is reported for the size distribution of the MNPs. Moreover, each MNP contains approximately 400 Fe ions, in the form of maghemite/magnetite. Recalling the core-shell model of the MNPs (Section 1.1.2), Monte Carlo simulations indicate that in maghemite nanoparticles having a diameter of approximately 3 nm the majority of the Fe ions belongs to the external disordered shell, while only about one hundred Fe ions to the core [27]. The values of the parameters characterizing the studied MNPs are reported in Table 6.1. The saturation magnetization (M_s) and the anisotropy field (B_a) were extracted from magnetic measurements [17].

The narrow size distribution of the MNPs allows us to consider the system as constituted by an ensemble of approximately identical objects. Finally, considering that the dimensions of the MNPs formed inside LiDps are smaller than the size of the Bloch walls in iron, these MNPs can be considered as single-domain particles, meaning that all the spins inside them (the spin associated to each Fe(III) ion is $s = 5/2$) are coupled,

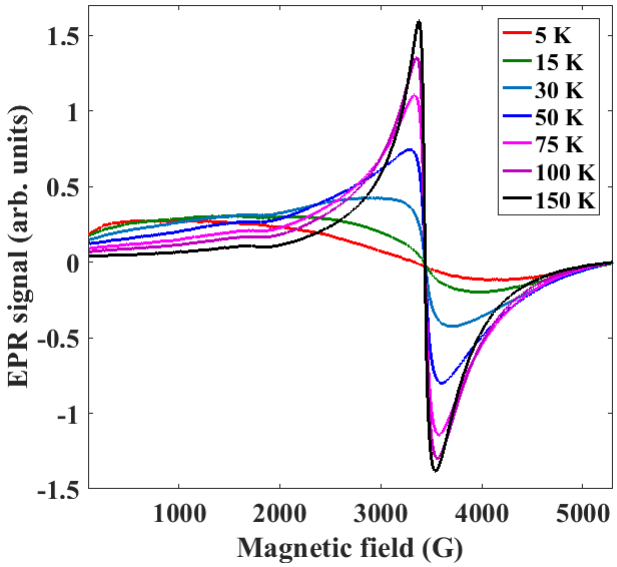

Figure 6.1: EPR spectra of MNPs mineralized in the LiDps protein acquired at X-band in the perpendicular configuration at various temperatures.

giving rise to a giant spin S.

6.3 EPR measurements

EPR measurements were realized at X-band with a standard EPR spectrometer.

The EPR spectra were acquired at different temperatures comprised between 150 K and 5 K in two different configurations, perpendicular and parallel, i.e. with the microwave field ($\mathbf{B}_1$) perpendicular and parallel to the external magnetic field ($\mathbf{B_0}$), respectively. The allowed transitions have different selection rules in the two configurations (see Section 2.2.1). Therefore, these alternative measurements are a way to sense and address the quantum nature of the system.

The measurements realized in the perpendicular configuration are reported in Fig. 6.1. The spectrum measured at 150 K shows a resonance at a field B_0 of about 3400 G; this resonance becomes broader and shifts towards a lower value upon decreasing the temperature. This can be qualitatively explained by considering that, upon decreasing the temperature, the MNP changes gradually from a system displaying superparamagnetic behavior to one in which the magnetic fluctuations are blocked, with the anisotropy field of the MNP becoming more effective in influencing the resonance position. As a result, the spectra become broader and the resonance position shifts towards lower field values [20]. Moreover, at the highest temperatures the presence of a band with a minor intensity at a field around half B_0 can be observed. This band may be ascribed to

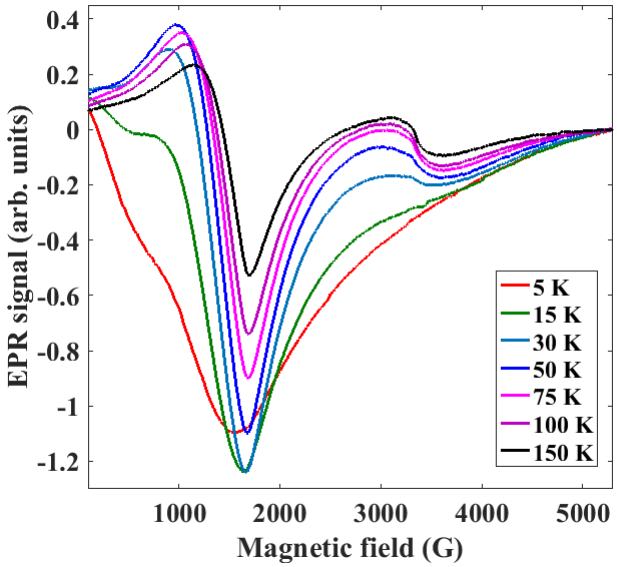

Figure 6.2: EPR spectra of MNPs mineralized in the LiDps protein acquired at X-band in the parallel configuration at various temperatures.

'partially' forbidden transitions between spin states with $\Delta M_S = \pm 2$ (M_S is the spin projection along z).

This interpretation is confirmed by the measurements realized in the parallel configuration (see Fig. 6.2): the spectra show a principal resonance at a field $B_0/2$. Moreover, as in the perpendicular case, the spectra become broader and shift to a minor field value upon lowering the temperature.

The observation in the perpendicular configuration of a signal occurring at $B_0/2$ arising from otherwise forbidden transitions $\Delta M_S = \pm 2$ shows the discrete character of the energy levels and therefore the quantum nature of these MNPs. The appearance of these transitions is in fact attributed to the non-coincidence between the external magnetic field and the easy-axis direction of the MNP, that is, the quantization axis being at an intermediate orientation between the two [26]. Describing the MNPs EPR spectra by means of a spin Hamiltonian (relative to the giant spin of the MNPs) that contains both Zeeman and zero field splitting interactions, an admixing of adjacent $M_S \pm 1$ states due to the nondiagonal matrix elements of the operators $\hat{S}_z\hat{S}_\pm$ is encountered, which is responsible for the signal occurring at $B_0/2$ [19, 17].

6.4 Theoretical model

In order to interpret the EPR spectra and characterize the quantum nature of the MNPs, simulations were performed for both configurations at every temperature. These

simulations were based on the giant spin model. This approach has been extensively used for MNMs in order to describe the interaction of their spin ground state with the external magnetic field [146, 147, 148, 149, 150]. In analogy with molecular clusters, a giant spin **S** was associated to each MNP and its behavior was described by a spin Hamiltonian

$$H = \mu_B \mathbf{B} \cdot \mathbf{g} \cdot \mathbf{S} + \mathbf{S} \cdot \mathbf{D} \cdot \mathbf{S} \tag{6.1}$$

where the first term is the electronic Zeeman term and the second one is the zero field splitting term. In the giant spin approximation the excited spin states are neglected.

As a first step the values of the ground state spin S and D parameter of the MNPs were calculated from the magnetic data. By reversing the relation defining the electronic magnetic moment (Eq. 2.10), the total spin of the MNPs was evaluated as

$$S = \frac{\mu}{g\mu_B} \tag{6.2}$$

Considering that the magnetic moment of each MNP can be estimated from the relation $\mu = M_{sv}V_p$, where $M_{sv} = M_s\rho$ is the volume magnetization and V_p is the volume of the MNP, with the values reported in Table 6.1 Eq. 6.2 gives $S \simeq 300$. Moreover, using the relation [16]

$$D = -\frac{g\mu_B B_a}{2S}$$

the value of the D parameter was estimated to be about -13 MHz (corresponding to -4.3×10^{-4} cm^{-1}).

Given the estimated value of S, a full matrix diagonalization of the spin Hamiltonian is difficult, because of the huge dimension of the Hilbert space associated with the system. For this reason we used a simplified simulation approach, employing an effective smaller spin value and, accordingly, effective spin Hamiltonian and experimental parameters, as successfully done in a preceding work on MNPs mineralized in the internal cavity of the ferritin protein [20]. In particular, this model is based on the possibility to simulate the EPR spectrum of MNPs of spin S by means of an effective lower spin $S_{eff} = \frac{S}{n}$ (with n integer and positive). Considering that the value of the product DS must be kept constant, such that also B_a remains constant, an effective D value was defined as $D_{eff} = nD$. Finally, in order to simulate an experimental temperature T, an effective temperature $T_{eff} = \frac{T}{n}$ was considered. This definition guarantees that the correct relation between the thermal energy k_BT and the energy barrier of the system, that is proportional to DS^2 (see Section 1.1.3.1), is maintained. As a result, the simulations of the EPR spectra were realized considering the spin Hamiltonian

$$H = \mu_B \mathbf{B} \cdot \mathbf{g} \cdot \mathbf{S}_{\text{eff}} + \mathbf{S}_{\text{eff}} \cdot \mathbf{D}_{\text{eff}} \cdot \mathbf{S}_{\text{eff}} \tag{6.3}$$

As a test of the capacities of the proposed model, a comparison between full simulations of the EPR spectra by means of Eq. 6.1 for a test case $S = 100$ and the simulations

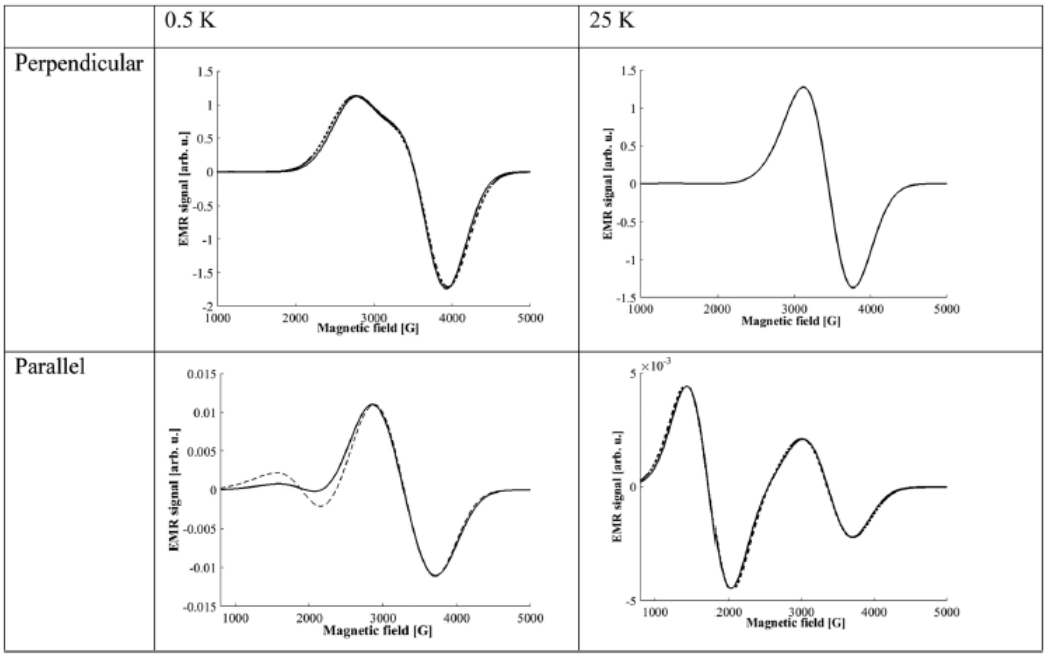

Figure 6.3: Full simulations of the EPR spectra acquired in the perpendicular and parallel configurations realized for a test case $S = 100$, $D = -10$ MHz, $T = 0.5$ K and 25 K (continuous lines) and simulations of the corresponding effective system with $S_{eff} = 10$, $D_{eff} = -100$ MHz, $T_{eff} = 0.05$ K and 2.5 K (dashed lines). Image taken from [20].

of the corresponding effective system with $S_{eff} = 10$ (i.e. $n = 10$), realized using Eq. 6.3, is reported in Fig. 6.3 [20]. The agreement between the two sets of simulations is rather good, except in the low field region of the spectrum relative to the parallel configuration at low temperature. While taking into account its limitations, the success of the simulation procedure based on the simplified effective model lead us to apply it to the study of the investigated MNPs.

The first simulations were realized choosing $S_{eff} = 10$ (i.e. $n = 30$) and correspondingly $D_{eff} = -400$ MHz. However, these values did not allow to obtain good simulations of the experimental spectra along all the temperature range and for both configurations. Moreover, an attempt to interpret the spectra by means of a distribution of the parameters, reflecting a possible heterogeneity of the sample, did not give appreciable results. Finally, the simulations were optimized by considering two different effective spins (S_1 and S_2) and correspondingly two distinct effective D parameters (D_1 and D_2). At each temperature, the spectra originating from the two sets of parameters ($Spec1\,(S_1, D_1, T)$ and $Spec2\,(S_2, D_2, T)$) were combined by means of two temperature dependent parameters ($\alpha\,(T)$ and $\beta\,(T)$) in order to simulate the experimental spectrum ($Spec\,(T)$)

$$Spec\,(T) = \alpha\,(T)\,Spec1\,(S_1, D_1, T) + \beta\,(T)\,Spec2\,(S_2, D_2, T) \tag{6.4}$$

The best simulations were achieved, for each configuration at each temperature, by considering two spin states having the same value of S_{eff} ($S_1 = S_2 = 10$) and different D_{eff} ($D_1 = -500$ MHz and $D_2 = -200$ MHz). Moreover, two different strains on the D_{eff} values (i.e. two different widths for the distributions of D_{eff}) were used: $Dstrain_1 = 50$ MHz and $Dstrain_2 = 200$ MHz; these values were the same for every temperature and configuration (only in the perpendicular configuration at 5 K it was necessary to use $Dstrain_1 = 500$ MHz and to introduce also a strain on E of 100 MHz). Finally, for each temperature and configuration the linewidths associated with the resonance of the two states were varied. A random orientation of the easy axes of the MNPs in the frozen suspension was assumed. The spectra were simulated with Easyspin [139].

The comparison between the experimental and simulated spectra at each temperature for the perpendicular and parallel configurations is reported in Fig. 6.4 and 6.5. Looking at the perpendicular case, at 150 K the agreement between the EPR spectrum and the simulation is very good: the simulation shows the resonance at B_0 and also a resonance with lesser intensity at about $B_0/2$. This trend is well represented until 30 K, although there is an increasing discrepancy between the data and the simulations in the low field region. The agreement is poorer at 15 K and 5 K: however, the simulations still give the correct trend at high field. Passing to the parallel configuration, similar observations can be done: at 150 K the agreement is good, although the presence of a slight shift between the experimental spectrum and the simulation. Between 75 K and 15 K there is an increasing lack of intensity in the simulated data at low field, but the agreement remains acceptable. The measured spectrum is instead well reproduced at 5 K.

In Fig. 6.6, the temperature dependence of the $\alpha\,(T)$ and $\beta\,(T)$ parameters is reported. The first thing to note is that at each temperature the same values are encountered for both the experimental configurations. Moreover, while $\alpha\,(T)$ remains practically constant with the temperature, $\beta\,(T)$ decreases with the temperature. In particular, its behavior can be fitted with an exponential function of the form

$$\beta\,(T) = a + b \exp\left(-\frac{T_0}{T}\right) \tag{6.5}$$

with $a = 0.3 \pm 0.2$, $b = 6.2 \pm 1.3$ and $T_0 = (115 \pm 26)$ K. The fit is reported in Fig. 6.6.

In Fig. 6.7, the temperature dependence of the linewidths used to simulate the spectra associated with the states S_1 and S_2 for both configurations is reported. These values differ between the two states and the two configurations, but have the same trend with the temperature: they increase upon lowering the temperature. Furthermore, while the linewidths corresponding to S_1 change little, the linewidths corresponding to S_2 show a great increase below 50 K.

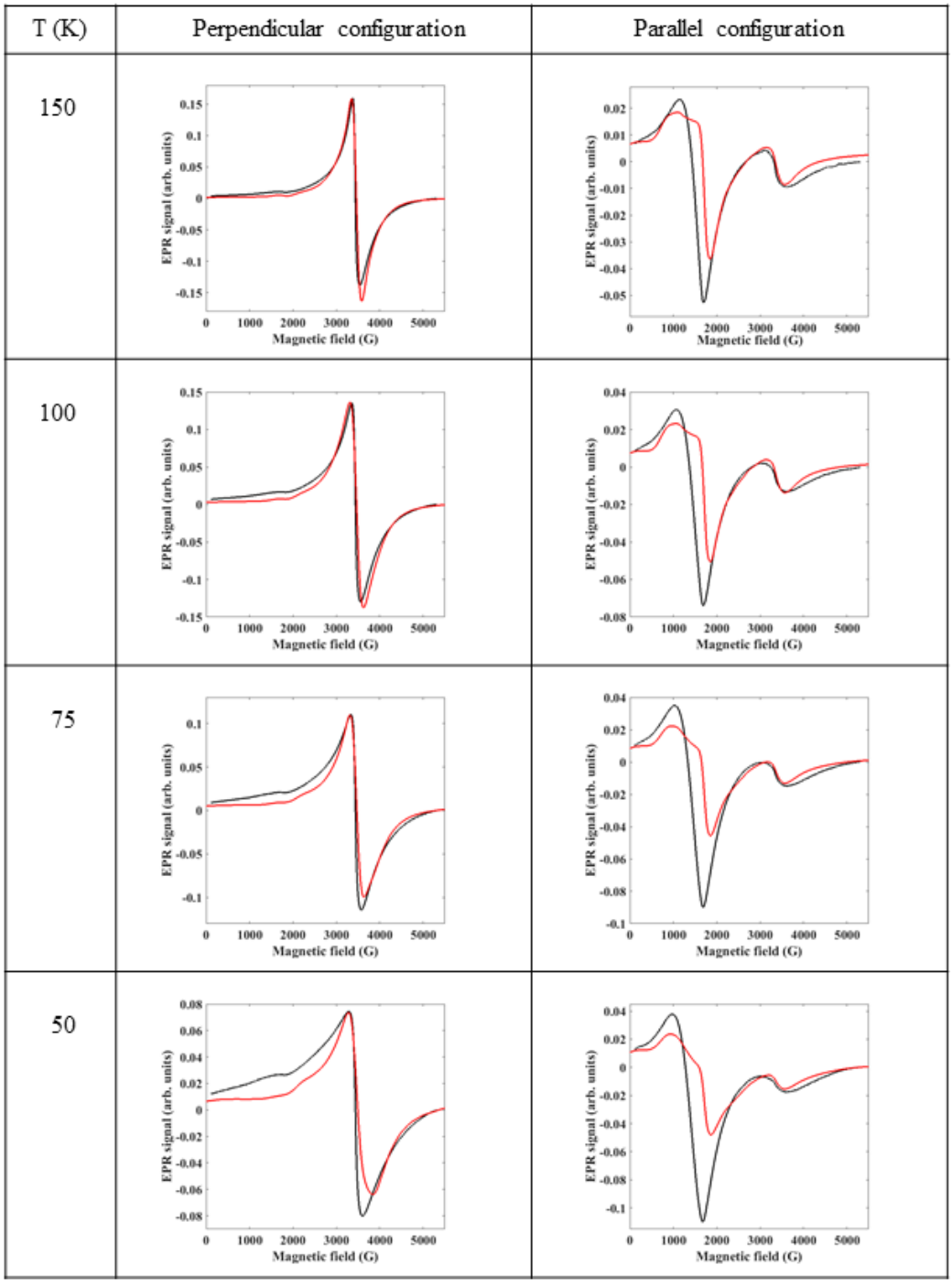

Figure 6.4: Experimental EPR spectra (black line) acquired in the parallel and perpendicular configurations at 150 K, 100 K, 75 K and 50 K and corresponding simulations (red line).

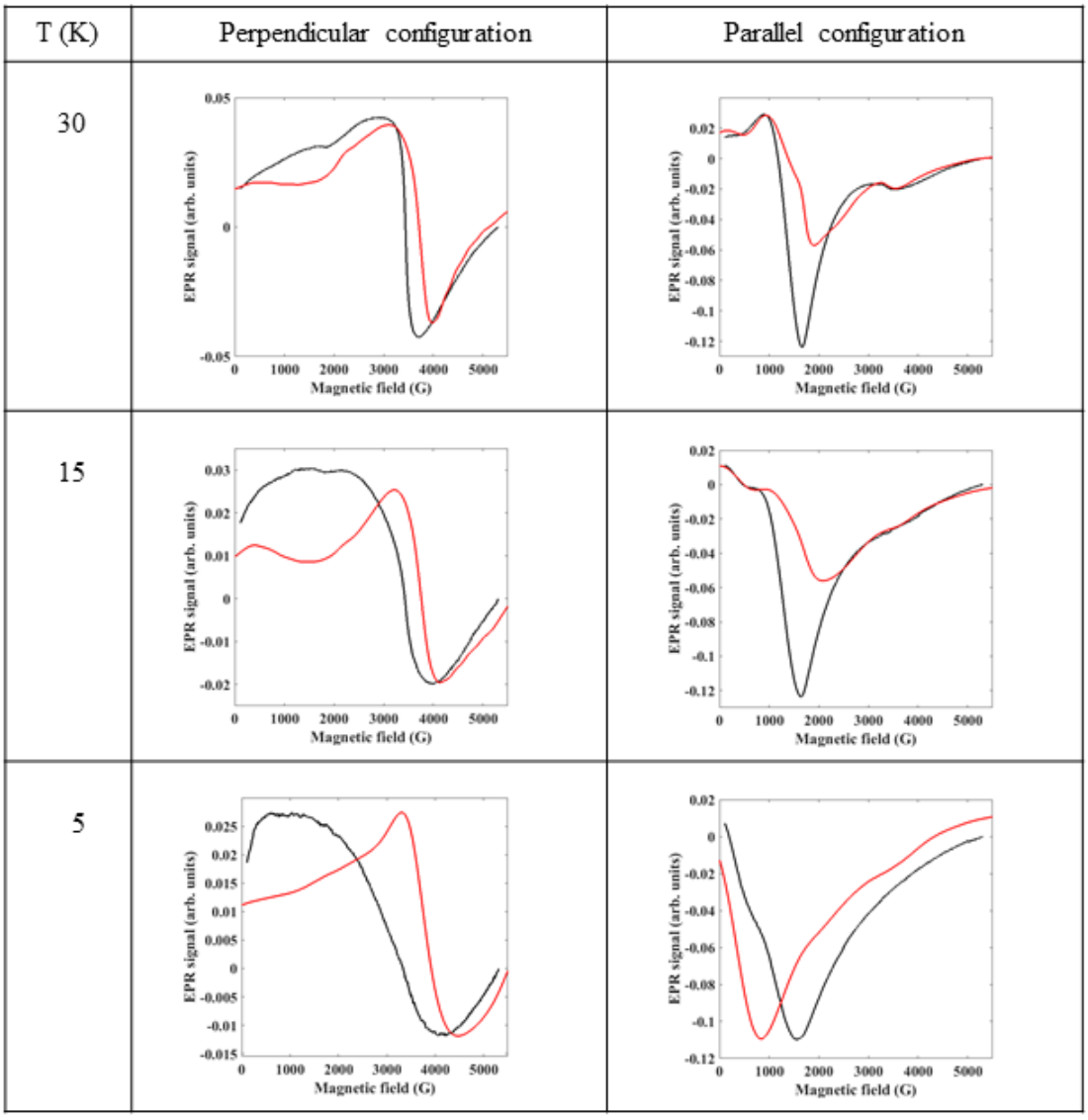

Figure 6.5: Experimental EPR spectra (black line) acquired in the parallel and perpendicular configurations at 30 K, 15 K and 5 K and corresponding simulations (red line).

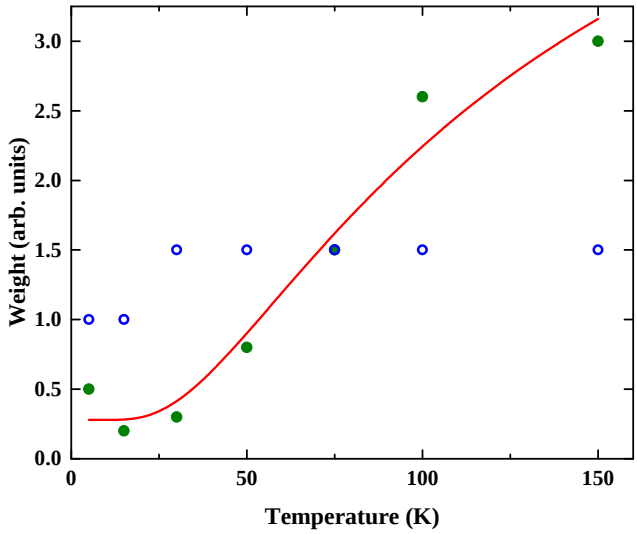

Figure 6.6: Values of the $\alpha\,(T)$ (blue circles) and $\beta\,(T)$ (green dots) parameters of Eq. 6.4 as a function of temperature. The red line is a fit of the $\beta\,(T)$ parameter by means of the exponential function reported in Eq. 6.5.

Finally, as a test of the model used for the simulations, the double integral of the EPR spectra was calculated and compared with the double integral of the corresponding simulated spectra for both configurations (see Fig. 6.8). Although the trend is roughly reproduced for both configurations, the agreement is better at the highest temperatures. The very broad character of the spectra, especially at low temperatures, renders the evaluation of the double integral more problematic. Moreover, the discrepancy between the experimental and the simulated spectra is higher at the lowest temperatures. The maximum observed in the experimental data of Fig. 6.8a, can be attributed to the blocking temperature relative to the experimental technique [151].

6.5 Discussion

EPR spectra of small MNPs mineralized inside the LiDps protein were simulated by means of a simplified version of the giant spin model. Together with the advantage to avoid the difficulties due to a full matrix diagonalization of the spin Hamiltonian (depending on the huge dimensions of the Hilbert space associated with these MNPs), an effective approach was suggested by the overall behavior of the EPR spectra. The interpretation of the resonance fields by means of Eq. 2.27, which is valid for $\theta = 0$ also when the strong field limit is not respected, is in fact not possible, since the induced transitions are packed together, therefore producing a loss of resolution in the spectra.

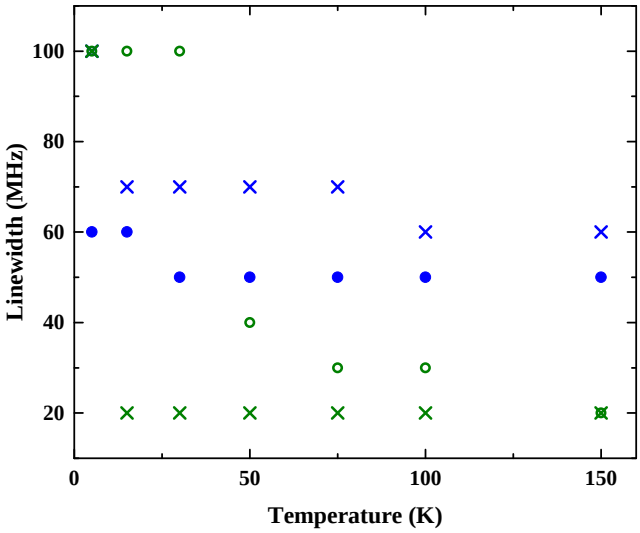

Figure 6.7: Values of the linewidths used for $Spec1\,(S_1, D_1, T)$ (in blue) and $Spec2\,(S_2, D_2, T)$ (in green) in the perpendicular and parallel configurations (dots and crosses, respectively) as a function of temperature.

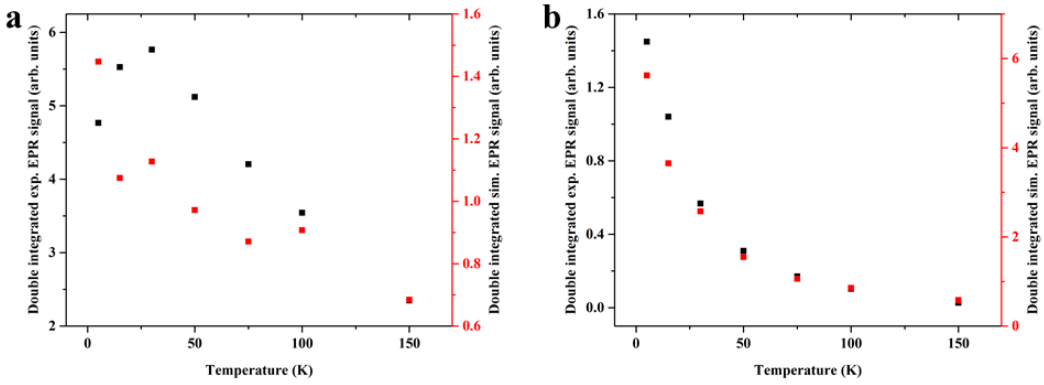

Figure 6.8: Double integral of the experimental EPR spectra (in black) acquired in the perpendicular (a) and parallel (b) configurations and of the simulated EPR spectra (in red) as a function of temperature.

This feature is expected considering that the system includes a high number of ions (see Fig. 2.9); moreover, a second reason is that the acquired EPR spectra are powder spectra.

The key property of the proposed model is the substitution of the huge spin value of the MNPs with a lower effective one. Moreover, we encountered the necessity to simulate the system of the MNPs as the combination of two subsystems having the same effective spin, but different D values (and different corresponding strain over them). The combination of the two spin states resulted to be temperature dependent and the same combination of the two subsystems allowed to simulate both the experimental configurations of the EPR measurements. This last feature is a test for the confidence of the parameters found, keeping in mind that the system is far more complicated and the approach followed gives a simplified and fair description of its behavior.

Different hypotheses can be suggested on the necessity to consider two different spin states in order to simulate the EPR spectra. The fact that the combination of the two subsystems varies with the temperature excludes the possibility that it may describe a possible heterogeneity of the sample. It can be interpreted rather as a way to take into account the effect of excited spin states in the EPR spectra, the contribution of which is not considered in the spin Hamiltonian. This interpretation is confirmed by the analogy with MNMs, where it is known that, by increasing the number of magnetic centers, the excited spin states become closer in energy to the fundamental spin state, for example the separation between the first excited spin state and the ground spin one is 24 K in Fe_8, while it decreases to 8 K in Fe_{19} [28]. Therefore, the excited spin states have to be considered in the thermal evolution of the EPR spectra. The inclusion of other terms in the spin Hamiltonian, although possible, is in our opinion of secondary importance with respect to the inclusion of excited spin states for two reasons. One reason is that, in analogy with MNMs, these states are expected to be lying very close to the ground spin state. The second reason is that from the angular dependence of EPR spectra acquired in the perpendicular configuration for a solution of MNPs frozen in an external magnetic field [17, 151] an axial anisotropy is derived for the resonance position of the main resonance, giving no indication of higher order contributions to the spin Hamiltonian.

The temperature T_0, obtained from the fit of the values of the $\beta(T)$ parameter, can be interpreted as an indication of the energy separation between the energy levels of the spin states considered. However, the value found from the fit is rather above the expected one [26, 17]. We consider this value affected by a decreasing quality of our simulations at low temperature: the discrepancy between measured and simulated spectra in this thermal range may determine its overestimation. In other words this feature may be relied with the simplicity of our model and the necessity to include other details for a correct estimation of T_0.

An alternative interpretation of T_0 relies on the core-shell model of MNPs: T_0 may indicate a characteristic temperature for the interaction between the core ions and the superficial ones.

In conclusion, our model for the simulation of the EPR measurements of MNPs

confirmed their quantum behavior. Our EPR measurements were acquired in X-band. In this band the Zeeman interaction is of the same order of magnitude of the zero field splitting interaction. The ratio between the transitions at $B_0/2$ and B_0 is expected to strongly decrease by increasing the external field value and this has been already reported by comparing X-band and W-band measurements [17]. This feature is a further evidence of the quantum nature of the system.

6.6 Conclusions

The possibility to efficiently simulate EPR spectra of MNPs with a modified version of the giant spin model was demonstrated. With the proposed approximation we simulated EPR spectra of huge spin values, describing the system with same spin Hamiltonian parameters in both experimental configurations for a wide range of temperatures. Finally, this description enabled to evidence the quantum behavior of the MNPs, suggesting also the necessity to take into account the population of the excited spin states.

Author contributions: M.F. planned the research. P.C. and E.F. synthesized the material. M.F. performed the experiments. EPR data were analysed by A.Ci. and M.F. A.Ci. and M.F. wrote the manuscript with the support of D.G.

Chapter 7

Conclusions

The aim of this thesis has been the spectroscopic characterization of different kinds of nanomaterials. The interest in these materials is driven by the fact that approaching nanometer dimensions peculiar and different electrical, optical and magnetic properties with respect to those observed in the bulk phase can be observed, as the emergence of quantum effects. Therefore nanomaterials represent promising objects both for the study of fundamental science and for new interesting applications in many technological fields.

Three different magnetic nanomaterials and a spin crossover complex have been studied. The study of these materials allowed to characterize different behaviors associated with their different dimensions and structure, starting from the single iron ion, passing to a cluster of interacting ions, that is the base of a single molecule magnet, to end with an ensemble of hundreds of ions, that constitutes a magnetic nanoparticle. In this size range the molecular approach allows to understand the properties of systems starting from the single molecule and therefore to follow the evolution of the properties of the system towards macroscopic dimensions. In order to characterize the studied nanomaterials and face some of the open problems regarding them and their use in the proposed applications, state-of-the-art configurations of Mössbauer spectroscopy or electron paramagnetic resonance (EPR) spectroscopy were used.

The first magnetic nanomaterial studied and reported in this thesis was the Fe_4 single molecule magnet (SMM) deposited on a gold surface. The Fe_4 molecule is constituted by four Fe(III) ions that occupy the center and the vertexes of an approximately equilateral triangle. Thanks to an antiferromagnetic coupling between the spin of the central ion and the spins of the peripheral ones, the ground state of the molecule has a total spin $S = 5$. Moreover, the molecule shows a moderate easy-axis magnetic anisotropy, directed perpendicular to the plane of the four Fe(III) ions, that is responsible for the double well energy potential characterizing the SMMs. SMMs are a very appealing class of nanomagnetic objects with potential application in spintronics and quantum computing. However, the use of these molecules for the proposed applications relies on the persistence of their properties once they are deposited on a solid surface. For this reason a monolayer of Fe_4 chemically grafted on gold was investigated by means of synchrotron

Mössbauer spectroscopy, taking advantage of the Synchrotron Mössbauer Source (SMS) available at ID18, the nuclear resonance beamline of the "European Synchrotron Radiation Facility" (ESRF). By means of an appropriate filtering of synchrotron light, the SMS produces a ^{57}Fe-resonant narrow single line with high intensity and spatial resolution. These features of the synchrotron radiation together with the possibility to realize measurements in the grazing incidence geometry allowed to enhance by two orders of magnitude the sensitivity of Mössbauer spectroscopy with respect to a standard setup based on a radioactive source and this has enabled to collect energy-domain Mössbauer spectra of a monolayer of molecular material for the first time. Significant deformations of the magnetic core of the molecules induced by the interaction with the substrate were detected. Although clearly shown by state-of-the-art *ab initio* molecular dynamics, these deformations were undetectable by conventional synchrotron-based magneto-optical techniques, such as X-ray magnetic circular dichroism. However, Mössbauer spectroscopy revealed that these modifications do not alter the overall magnetic structure of the system. Therefore, the spin state and the anisotropy of the system, and consequently the SMM behavior, are retained after deposition. This makes the Fe_4 class of molecules particularly well suited for organization on surface and insertion in single molecule devices. This work evidences also that synchrotron Mössbauer spectroscopy based on SMS is a powerful technique for the study on thin films of molecules deposited on a surface.

A second application of synchrotron Mössbauer spectroscopy based on SMS was the study of the spin crossover (SCO) complex $[Fe(H_2B(pz)_2)_2(phen)]$ deposited on a gold substrate. SCO molecules are bistable systems, that can reversibly switch between two distinct spin states, a low spin and a high spin state, by means of a variety of external stimuli, such as temperature, pressure and irradiation with electromagnetic radiation of appropriate wavelength at low temperature (LIESST effect). The possibility to change the spin state of the SCO molecules via an external input makes them promising building blocks for spintronic and high-density memory devices, as well as potential elements for displays and sensors. However, the SCO transition is a cooperative phenomenon and its features depend on the environment surrounding the molecule. Therefore, in view of the proposed applications, the SCO efficiency of the molecules has to be verified once they are deposited on a surface. The SCO transition properties of samples having different thickness (ranging from about one hundred nm to few nm) of molecules deposited on gold were investigated. The SCO transition was induced both thermally and via LIESST effect. The analysis of the Mössbauer spectra allowed to characterize and evaluate the contributions of the low spin and high spin states present in each measurement. A reduction of the SCO efficiency of the deposited molecules was encountered with respect to molecules in the bulk phase. Moreover, values of the SCO efficiency comparable to the thermally induced ones were achieved after about 3 hours of irradiation. This study confirms the effects of the interaction with the substrate on the conversion efficiency of SCO molecules.

By means of EPR spectroscopy with electric field modulation a pure spin magnetoelectric effect was detected in a single crystal of the molecular helicoidal chain

MnPhOMe. For this purpose a standard EPR spectrometer was implemented with the possibility to apply an electric field on the sample while revealing the EPR absorption. The electric field modulation was used in combination with a phase-sensitive detection. Thanks to this setup signals associated with a magnetoelectric coupling between the single crystal and the electric field were detected. When the electric field is applied parallel to the crystal c axis the electric field modulated (EFM) EPR signal shows different features depending on the relative orientation between the external magnetic field and the chain-axis of the crystal. In particular, the electric field modulation is responsible of a modulation of the magnetic exchange interaction. The effect detected in the EFM-EPR spectra is comparable with that expected from *ab initio* calculations. Finally, this magnetoelectric effect is particularly interesting for single molecule addressing and operation, since, in view of quantum information applications of magnetic nanomaterials, a faster, less energy demanding and more space-confined inspection can be realized with an electric field rather than with a magnetic one

Finally, EPR spectroscopy was used to characterize small magnetic nanoparticles of spinel type iron oxide mineralized in the internal cavity of a mini ferritin-type protein. The MNPs thus formed have an average diameter of about 3 nm and contain approximately 400 Fe ions, in the form of maghemite/magnetite. MNPs are approaching the size of molecular nanomagnets, the properties of which are described by means of quantum mechanics. A unified (quantum) view of the two objects is therefore recommended. In order to probe different selection rules, X-band EPR measurements of the MNPs were realized both in the standard perpendicular configuration (with the external magnetic field perpendicular to the magnetic field of the microwave radiation) and in the parallel one, where the external magnetic field is parallel to that of the microwave. These alternative measurements allowed to ascribe the resonance with minor intensity detected in the perpendicular configuration to 'partially' forbidden transitions between spin states, therefore showing the discrete character of the energy levels and thus the quantum nature of these MNPs. This observation was confirmed by the interpretation of the spectra using an approach based on the giant spin model. Given the huge value of the spin associated to the MNPs, a simplified simulation approach, employing an effective smaller spin value and, accordingly, effective spin Hamiltonian and experimental parameters was used. A rather good agreement between the experimental and simulated data was found in both experimental configurations for a wide range of temperatures. Finally, beyond enabling to evidence the quantum behavior of the MNPs, this description suggested also the necessity to take into account the population of the excited spin states.

In conclusion, different kinds of nanomaterials have been characterized in this thesis, clarifying useful aspects for their use in the proposed applications. The work has also revealed that synchrotron Mössbauer spectroscopy based on SMS is an efficient spectroscopic technique to investigate the properties of thin films of molecules deposited on a surface. Finally, the EPR spectrometer implemented with electric field modulation resulted to be a readily accessible and sensitive technique for the study of magnetoelectric molecular materials.

Appendix A

In this appendix supplementary materials to "Mössbauer spectroscopy of a spin crossover complex deposited on gold" discussed in Chapter 4 are reported.

In supplementary note, a list of publications on Fe(II)-based spin crossover molecules deposited on surfaces is reported.

In Fig. A.1, all the Mössbauer spectra of the 50 nm thick sublimated sample realized at 6.0 K at different irradiation times are reported.

In Fig. A.2 and A.3, the isomer shift of the HS state extracted from the fit of the Mössbauer spectra of the 50 nm and 5 nm thick samples as a function of the logarithm of the effective thickness of the sample is reported.

In Fig. A.4 and A.5, the total effective thickness extracted from the fit of the Mössbauer spectra of the 50 nm and 5 nm thick samples as a function of the temperature is reported.

Supplementary note

Concerning the Fe(II)-based SCO complexes, many studies by means of different techniques are reported in literature regarding different thicknesses (from hundreds of nm to single molecule layers) of different molecules deposited on surfaces.

A study of the thermal SCO and LIESST effect of $[Fe(H_2B(pz)_2)_2(2,2'-bipy)]$ molecules on Au(111) [124] revealed that, while for a 300 nm thick sample the conversion was complete, as for the bulk sample, for a sub-monolayer coverage the efficiency decreased to 20 %, with the majority of the molecules trapped in a definite spin state ($\sim$ 50 % in HS and $\sim$ 30 % in LS). In bilayer films of the same compound on Au(111) a spin state coexistence independent of temperature between 131 K and 300 K was reported [152].

In a 1.6 monolayer thick sample of $[Fe(H_2B(pz)_2)_2(phen)]$ adsorbed on Au(111) [153] only the second layer of molecules exhibited a thermal SCO, while no SCO was found for the monolayer, because of a dissociation of the SCO compound into $[Fe(H_2B(pz)_2)_2]$ and phen moieties when in direct contact with Au(111).

In sub-monolayers of $[Fe^{II}((3,5-(CH_3)_2Pz)_3)BH)_2]$ grown on Au(111) the formation of a long-range ordered mixed spin state phase was reported together with the possibility to induce LS to HS switching of the molecules via LIESST effect [154]. Moreover, an X-ray absorption spectroscopy study of a sub-monolayer of the same molecule in direct

contact with a metallic Au(111) substrate confirmed the presence of the mixed phase of HS and LS below 100 K with one-third of the molecules in the HS state [155].

On the other side, a thermally induced nearly complete and reversible SCO transition was demonstrated for a sub-monolayer of $[Fe^{II}(NCS)_2L]$ (L: 1-{6-[1,1-di(pyridin-2-yl)ethyl]-pyridin-2-yl}-*N*,*N*-dimethylmethanamine) obtained by vacuum deposition on a highly oriented pyrolytic graphite (HOPG) surface [156]. Moreover, for a sub-monolayer deposition of $[Fe(H_2B(pz)_2)_2(phen)]$ on HOPG [56] the analysis of X-ray absorption spectra revealed a complete spin conversion from LS to HS via LIESST effect at 6 K and a 90 % efficiency for the thermal SCO, indicating that the interaction of the molecule with HOPG is weaker with respect to Au(111) and the integrity of the molecule is retained.

Also the substitution of an Au(111) substrate with a Bi(111) one prevents the fragmentation of $[Fe(H_2B(pz)_2)_2(phen)]$ and $[Fe(H_2B(pz)_2)_2(phenme_4)]$ molecules, sub-monolayers of which can be spin state switched both thermally and via LIESST effect, although with a large temperature independent HS fraction ($\sim$ 50 %) [157].

Thin films of $Fe\{[(Me_2Pyrz]_3BH\}_2$ deposited onto Si(100)/SiO2 substrates qualitatively retain the SCO features encountered in the bulk phase, but the transition temperature decreases while decreasing the thickness, affecting the hysteresis too; moreover, in the 100 nm thick sample the SCO transition is not complete at low temperature, with $\sim$ 20 % of the molecules still in the HS state [158].

Finally, $[Fe(phen)_2(NCS)_2]$ molecules on Cu(100) show a coexistence of the HS and LS states, but the SCO behavior can be restored upon reducing the interaction with the substrate by inserting a thin insulating layer of CuN [159, 160].

The trend shown by these examples indicates that a reduction of efficiency in the SCO transition is encountered when the molecules are deposited on a surface with respect to molecules in the bulk phase. However, the amount of this reduction depends on the kind of SCO molecules. Moreover, for a given molecule the SCO efficiency changes for different kinds of substrate. Finally, for a given molecule the interaction with the same substrate can be altered by attaching different substituents to the ligands [161].

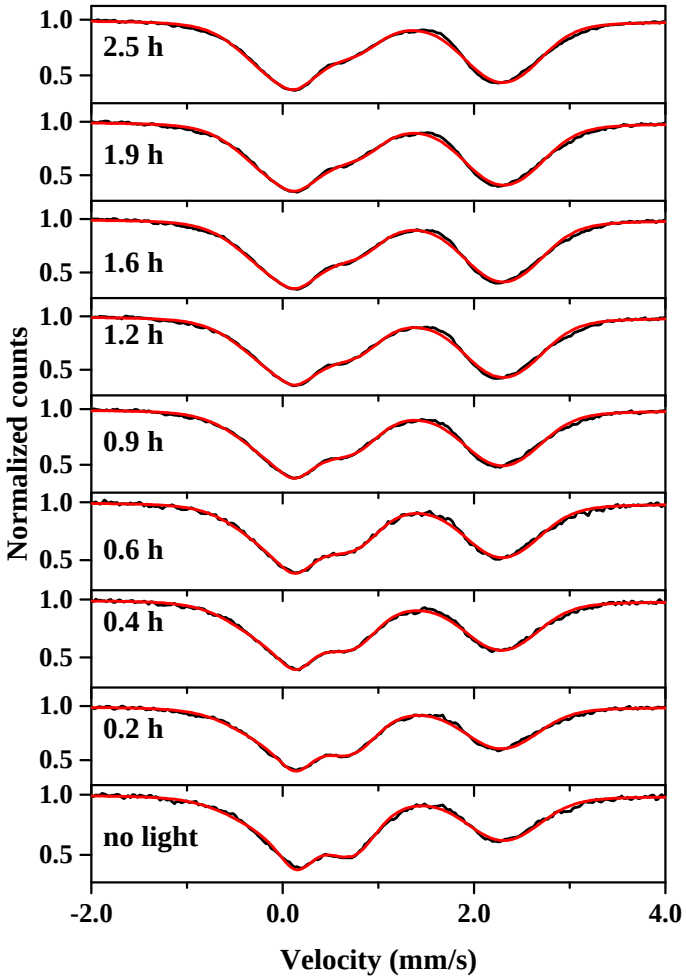

Figure A.1: Mössbauer spectra (in black) and corresponding best fit curves (in red) of the 50 nm thick sublimated sample at 6.0 K as a function of the irradiation length. The velocity axis values are relative to the α-Fe standard.

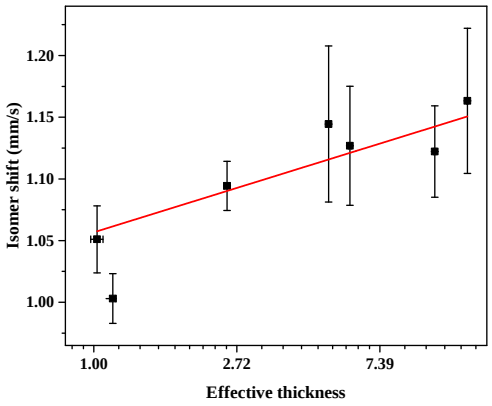

Figure A.2: Isomer shift of the HS state of the 50 nm thick sublimated sample extracted from the fit of the Mössbauer spectra as a function of the logarithm of the effective thickness of the sample. The red line is the linear fit.

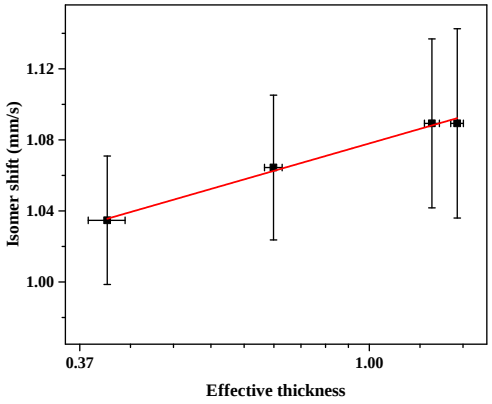

Figure A.3: Isomer shift of the HS state of the 5 nm thick sublimated sample extracted from the fit of the Mössbauer spectra as a function of the logarithm of the effective thickness of the sample. The red line is the linear fit.

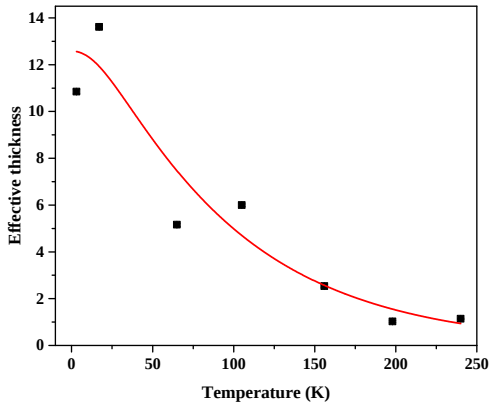

Figure A.4: Total effective thickness of the 50 nm thick sublimated sample extracted from the fit of the Mössbauer spectra as a function of the temperature. The red line is the fit with Eq. 2.5.

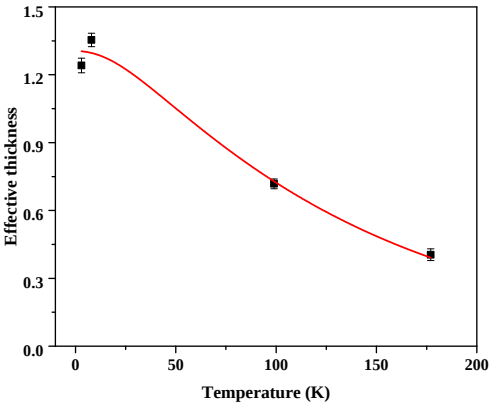

Figure A.5: Total effective thickness of the 5 nm thick sublimated sample extracted from the fit of the Mössbauer spectra as a function of the temperature. The red line is the fit with Eq. 2.5.

Appendix B

In this appendix supplementary materials to "Electric field modulation of magnetic exchange in molecular helices" discussed in Chapter 5 are reported.

In Fig. B.1, electric field modulated (EFM) EPR spectra acquired at 30 K with $\mathbf{B}_0 \perp \mathbf{c}$ for three different values of the applied microwave power are reported.

In Fig. B.2, the EFM-EPR spectra acquired at 30 K with $\mathbf{B}_0 \parallel \mathbf{c}$ and $\mathbf{B}_0 \perp \mathbf{c}$ and the EFM-EPR spectra acquired in the same conditions inverting the polarity of the electrodes are reported.

In Fig. B.3, the effect induced on the standard EPR spectra by applying a continuous electric field is shown.

In Fig. B.4, the EFM-EPR spectra acquired at 30 K with $\mathbf{B}_0 \parallel \mathbf{c}$ for three different values of the applied voltage are reported.

In Fig. B.5, the comparison between the simulations of the EFM-EPR spectra realized with the different models reported in Chapter 5 is reported.

In Fig. B.6, a schematic representation of the simulation procedure used to simulate the EFM-EPR spectra is reported.

In Fig. B.7 and B.8, the behavior of α as a function of $\Delta\Gamma$ and the behavior of $\Delta\Gamma$ as a function of the applied voltage are reported.

In Table B.1, the values of the parameters used to simulate the EPR and EFM-EPR spectra are reported.

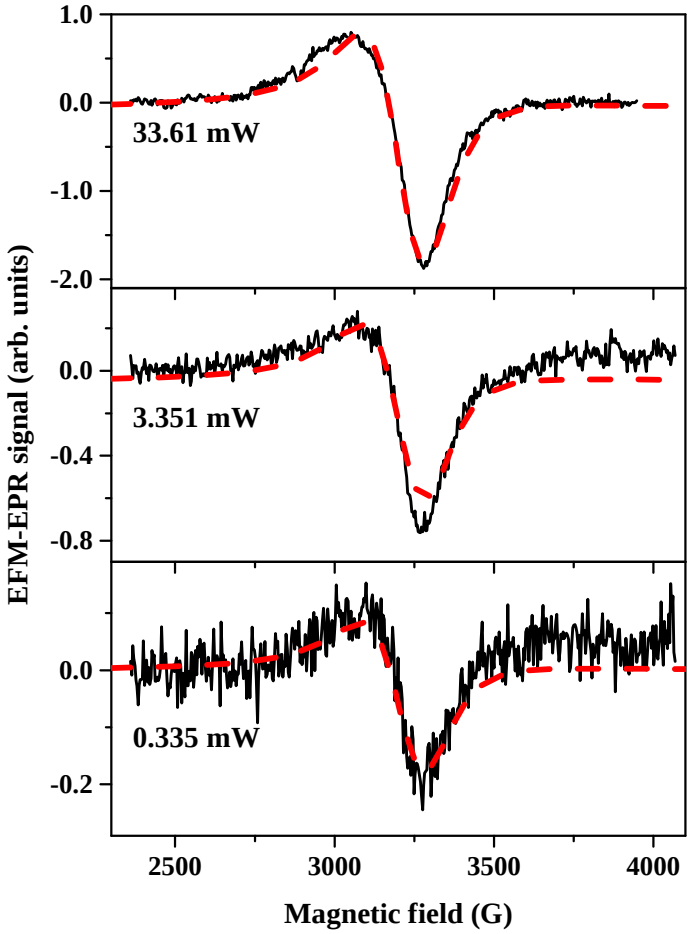

Figure B.1: EFM-EPR spectra (black lines) acquired at 30 K with $\mathbf{B}_0 \perp \mathbf{c}$ for three different values of the applied microwave power. Dash lines represent the corresponding simulations. The simulations of the spectra acquired with 3.351 mW and 0.335 mW were realized keeping the parameters fixed at the value found in the simulation of the spectrum acquired with 33.61 mW and rescaling opportunely the intensity according to the ratio between the corresponding microwave powers.

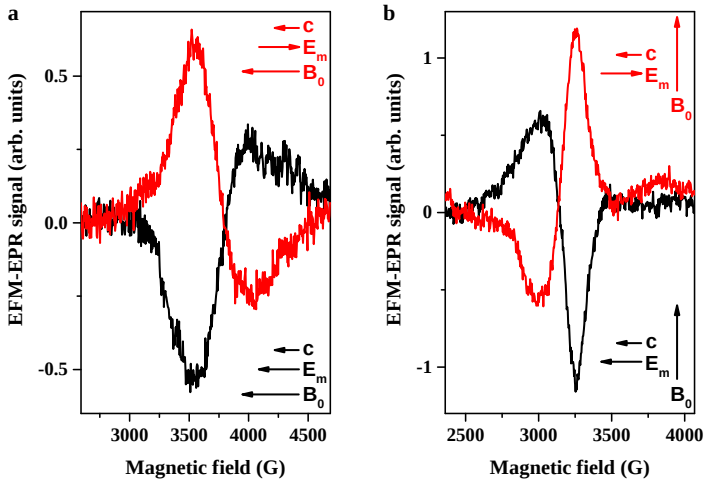

Figure B.2: EFM-EPR spectra (black lines) acquired at 30 K with $\mathbf{B}_0 \parallel \mathbf{c}$ (a) and $\mathbf{B}_0 \perp \mathbf{c}$ (b) and EFM-EPR spectra (red lines) acquired in the same conditions inverting the polarity of the electrodes. These spectra were recorded on a different crystal with respect to that reported in Chapter 5.

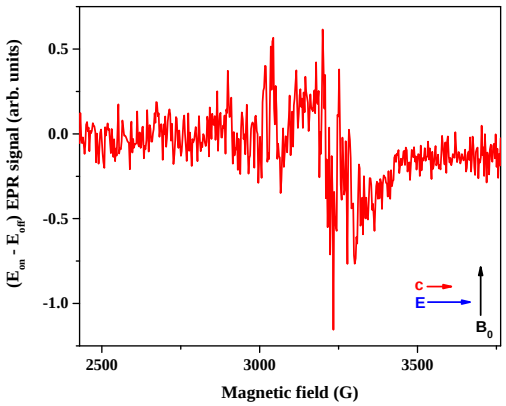

Figure B.3: Effect induced on the standard EPR spectra (acquired at 30 K) by applying a continuous electric field of 10^6 V/m parallel to $\mathbf{c}$ and perpendicular to $\mathbf{B}_0$. The spectrum is the difference between three EPR spectra acquired with the electric field on and three EPR spectra acquired with the electric field off, to which a temperature drift correction was subtracted. This last one was evaluated as the average signal obtained considering also the difference spectra recorded with the opposite polarity of the electric field. Therefore, in order to obtain this signal a time approximately 12 fold higher than that required for a single EFM-EPR spectrum is needed.

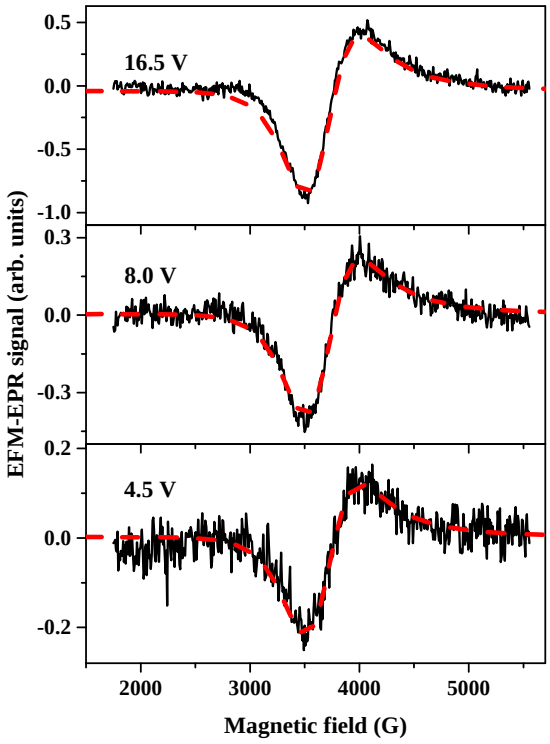

Figure B.4: EFM-EPR spectra (black lines) acquired at 30 K with $\mathbf{B}_0 \parallel \mathbf{c}$ for three different values of the applied voltage (16.5 V, 8.0 V and 4.5 V). Dash lines represent the corresponding simulations.

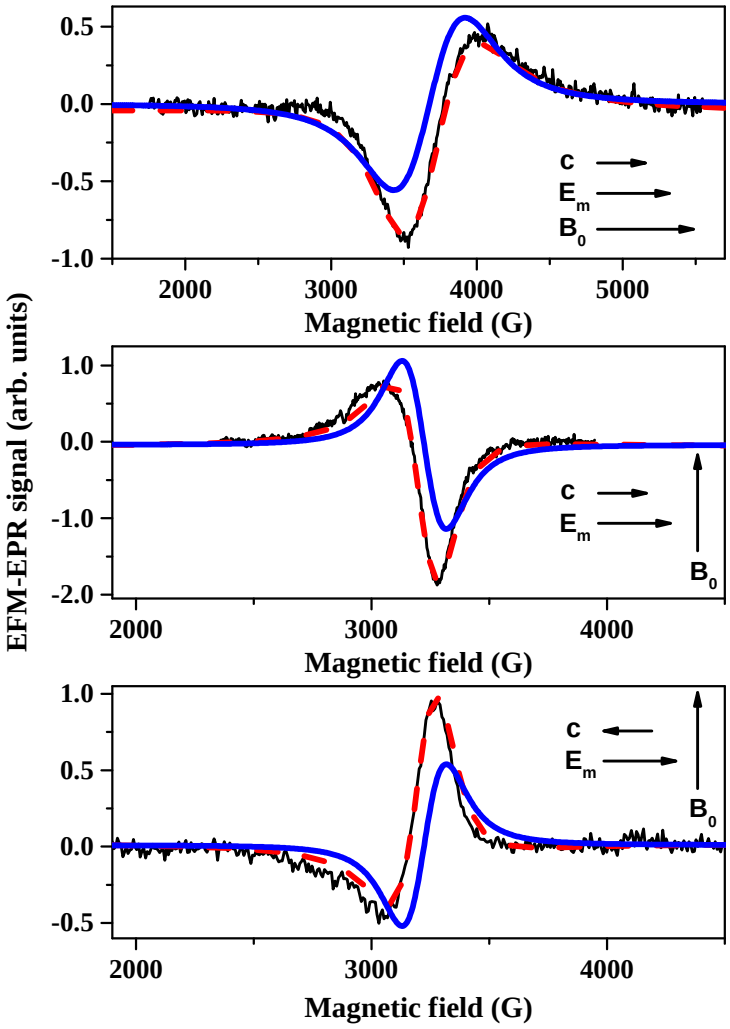

Figure B.5: Different simulations of the EFM-EPR spectra (black lines) acquired at 30 K. The blue lines represent the simulations realized considering Eq. 5.6. The dash lines represent the simulations realized considering Eq. 5.7.

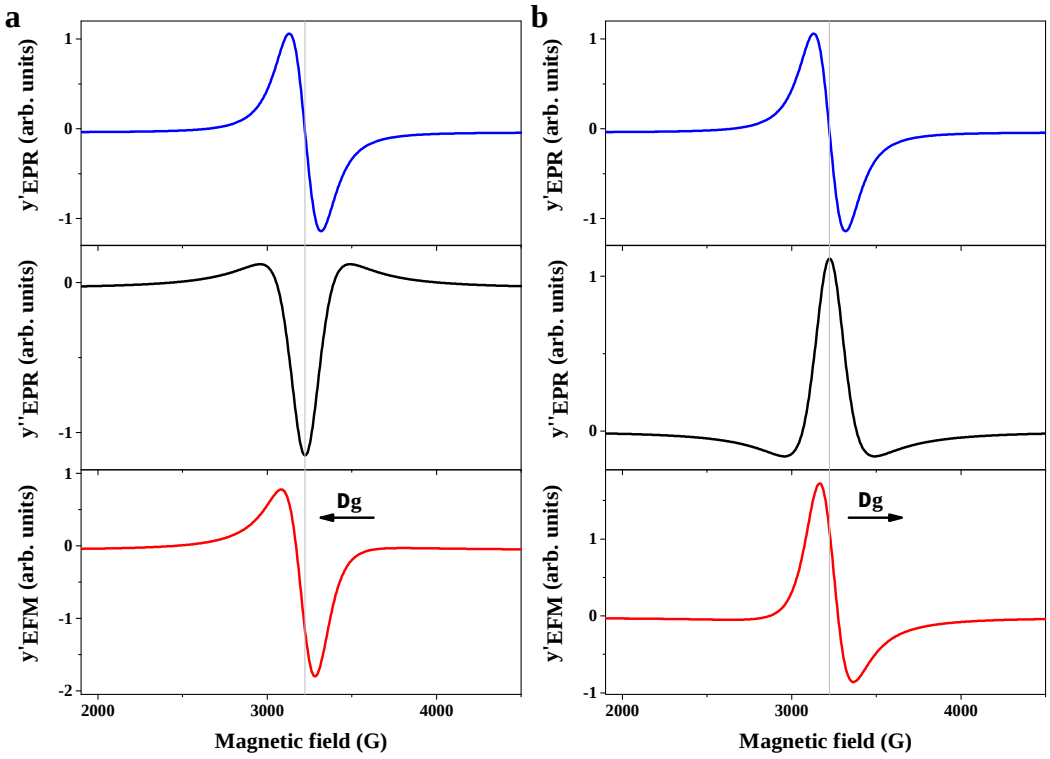

Figure B.6: Schematic representation of the simulation procedure described by Eq. 5.7. a) The combination of $\frac{B_m^{eq}}{B_m} y'_{EPR}$ (blue line) and a positive second derivative ($\alpha y''_{EPR}$ with $\alpha > 0$) (black line) enables to simulate a positive shift of the center of the spectrum and an asymmetry of the lineshape (red line), as observed for $\mathbf{B}_0 \perp \mathbf{c}$. b) The combination of $\frac{B_m^{eq}}{B_m} y'_{EPR}$ (blue line) and an inverted second derivative ($\alpha y''_{EPR}$ with $\alpha < 0$) (black line) enables to simulate a negative shift of the center of the spectrum and a reversed asymmetry of the lineshape (red line).

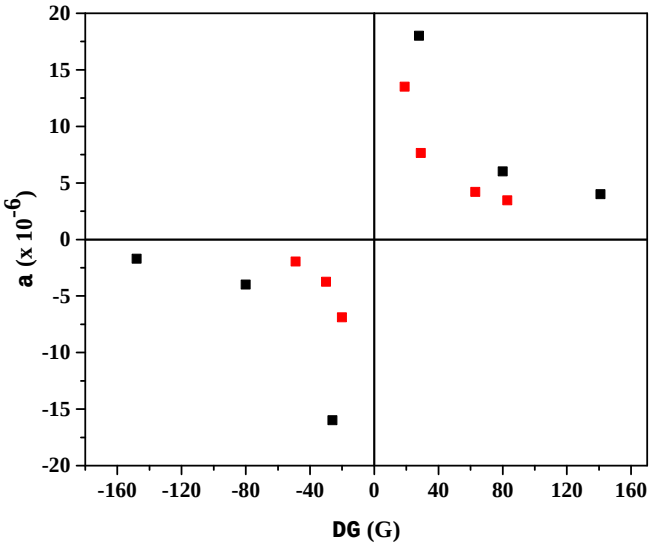

Figure B.7: Behavior of α as a function of $\Delta\Gamma$ in the $\mathbf{B}_0 \parallel \mathbf{c}$ (black dots) and $\mathbf{B}_0 \perp \mathbf{c}$ (red dots) configurations. The simulations were realized keeping the other parameters fixed at the value found with $\Delta\Gamma = 80$ G and $\Delta\Gamma = 29$ G, respectively.

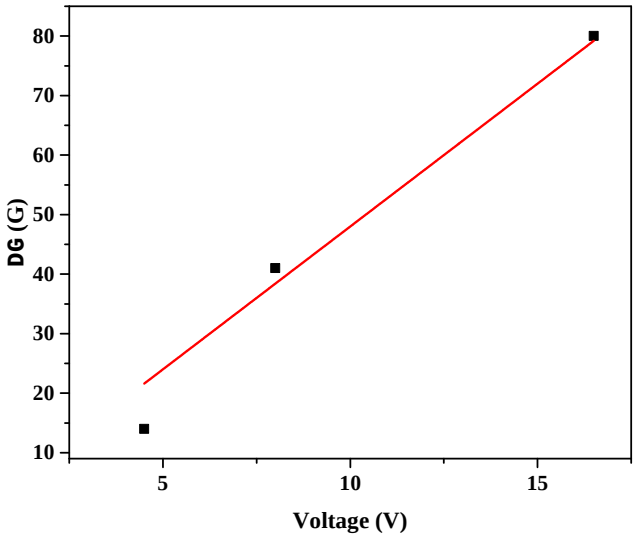

Figure B.8: Behavior of $\Delta\Gamma$ as a function of the applied voltage (16.5 V, 8.0 V and 4.5 V). The red line represents a linear fit.

CRY-STAL	T(K)	$\mathbf{B}_0$,$\mathbf{c}$	SIGNAL	g	Γ (G)	B_m^{eq} (G) ($\times 10^{-3}$)	Δg_E ($\times 10^{-6}$)	$\Delta\Gamma$ (G)	α ($\times 10^{-6}$)
1*	30	$\parallel$	EPR	1.828	494				
			EFM-EPR		494	6.4	-3.16	80	6.0
		$\perp$	EPR	2.085	205				
			EFM-EPR		186	2.3	1.50	29	7.7
2*	30	$\parallel$	EPR	1.815	494				
			EFM-EPR		494	4.3	-2.11	80	3.0
		$\perp$	EPR	2.118	234				
			EFM-EPR		186	1.5	0.99	29	4.3
3*	30	$\parallel$	EPR	1.811	494				
			EFM-EPR		494	4.6	-2.25	80	4.3
		$\perp$	EPR	2.105	234				
			EFM-EPR		166	1.2	0.79	20	3.3
1**	30	$\perp$	EPR	2.085	205				
			EFM-EPR		186	1.5	-0.98	29	-6.3
1*	50	$\parallel$	EPR	1.975	406				
			EFM-EPR		361	2.1	-1.22	80	6.5
		$\perp$	EPR	2.040	176				
			EFM-EPR		107	0.2	0.12	29	2.5

Table B.1: Parameters used to simulate the EPR and EFM-EPR spectra.
* Measurements realized with $\mathbf{c}$ and $\mathbf{E}_m$ pointing to the same direction.
** Measurements realized with $\mathbf{c}$ and $\mathbf{E}_m$ pointing to opposite directions.

Bibliography

[1] Robert Vajtai, editor. *Springer Handbook of Nanomaterials*. Springer-Verlag Berlin Heidelberg, 2013.

[2] Wolfgang Wernsdorfer. Classical and quantum magnetization reversal studied in nanometer-sized particles and clusters. *Advances in Chemical Physics*, 118:99–190, 2001.

[3] Dante Gatteschi, Roberta Sessoli, and Jacques Villain. *Molecular nanomagnets*. Oxford University Press, 2006.

[4] Taeghwan Hyeon. Chemical synthesis of magnetic nanoparticles. *Chemical Communications*, 271(8):927–934, 2003.

[5] Teruya Shinjo, editor. *Nanomagnetism and Spintronics*. Elsevier, Amsterdam, The Netherlands, 2009.

[6] An-Hui Lu, E. L. Salabas, and Ferdi Schüth. Magnetic Nanoparticles: Synthesis, Protection, Functionalization, and Application. *Angewandte Chemie International Edition*, 46(8):1222–1244, 2007.

[7] Stefano Sanvito. Molecular spintronics. *Chemical Society Reviews*, 40(6):3336–3355, 2011.

[8] Lapo Bogani and Wolfgang Wernsdorfer. Molecular spintronics using single-molecule magnets. *Nature materials*, 7(3):179–186, 2008.

[9] M. Urdampilleta, S. Klyatskaya, J-P. Cleuziou, M. Ruben, and W. Wernsdorfer. Supramolecular spin valves. *Nature Materials*, 10(7):502–506, 2011.

[10] Michael N. Leuenberger and Daniel Loss. Quantum computing in molecular magnets. *Nature*, 410(6830):789–793, 2001.

[11] Stefan Thiele, Franck Balestro, Rafik Ballou, Svetlana Klyatskaya, Mario Ruben, and Wolfgang Wernsdorfer. Electrically driven nuclear spin resonance in single-molecule magnets. *Science*, 344(6188):1135–1138, 2014.

[12] Muhandis Shiddiq, Dorsa Komijani, Yan Duan, Alejandro Gaita-Ariño, Eugenio Coronado, and Stephen Hill. Enhancing coherence in molecular spin qubits via atomic clock transitions. *Nature*, 531(7594):348–351, 2016.

[13] O. Kahn and C. Jay Martinez. Spin-Transition Polymers: From Molecular Materials Toward Memory Devices. *Science*, 279(5347):44–48, 1998.

[14] Jean-François Létard, Philippe Guionneau, and Laurence Goux-Capes. Towards Spin Crossover Applications. In *Spin Crossover in Transition Metal Compounds III*, pages 221–249. Springer, Berlin, Heidelberg, 2004.

[15] N. Baadji and S. Sanvito. Giant resistance change across the phase transition in spin-crossover molecules. *Physical Review Letters*, 108(21):217201, 2012.

[16] M. Fittipaldi, L. Sorace, A.-L. Barra, C. Sangregorio, R. Sessoli, and D. Gatteschi. Molecular nanomagnets and magnetic nanoparticles: the EMR contribution to a common approach. *Physical Chemistry Chemical Physics*, 11:6555–6568, 2009.

[17] M. Fittipaldi, C. Innocenti, P. Ceci, C. Sangregorio, L. Castelli, L. Sorace, and D. Gatteschi. Looking for quantum effects in magnetic nanoparticles using the molecular nanomagnet approach. *Physical Review B*, 83(10):104409, 2011.

[18] Pierpaolo Ceci, Emilia Chiancone, Oksana Kasyutich, Giuliano Bellapadrona, Lisa Castelli, Maria Fittipaldi, Dante Gatteschi, Claudia Innocenti, and Claudio Sangregorio. Synthesis of iron oxide nanoparticles in listeria innocua Dps (DNA-binding protein from starved cells): A study with the wild-type protein and a catalytic centre mutant. *Chemistry - A European Journal*, 16(2):709–717, 2010.

[19] N. Noginova, T. Weaver, E. P. Giannelis, A. B. Bourlinos, V. A. Atsarkin, and V. V. Demidov. Observation of multiple quantum transitions in magnetic nanoparticles. *Physical Review B*, 77:014403, 2008.

[20] M. Fittipaldi, R. Mercatelli, S. Sottini, P. Ceci, E. Falvo, and D. Gatteschi. Sensing the quantum behaviour of magnetic nanoparticles by electron magnetic resonance. *Physical Chemistry Chemical Physics*, 18(5):3591–3597, 2016.

[21] O. Waldmann, R. Bircher, G. Carver, A. Sieber, H. U. Güdel, and H. Mutka. Exchange-coupling constants, spin density map, and Q dependence of the inelastic neutron scattering intensity in single-molecule magnets. *Physical Review B*, 75(1):012415, 2007.

[22] J. Schnack, M. Luban, and R. Modler. Related content Quantum rotational band model for the Heisenberg molecular magnet {Mo72Fe30}. *EPL (Europhysics Letters)*, 56(6):863, 2001.

[23] Maria Axenovich and Marshall Luban. Exact ground state properties of the classical Heisenberg model for giant magnetic molecules. *Physical Review B*, 63(10):100407, 2001.

[24] J. Schnack and M. Luban. Rotational modes in molecular magnets with antiferromagnetic Heisenberg exchange. *Physical Review B*, 63(1):014418, 2000.

[25] Allan H. Morrish. *The physical principles of magnetism*. Wiley-IEEE Press, 2001.

[26] Dante Gatteschi, Maria Fittipaldi, Claudio Sangregorio, and Lorenzo Sorace. Exploring the No-Man's Land between Molecular Nanomagnets and Magnetic Nanoparticles. *Angewandte Chemie International Edition*, 51(20):4792–4800, 2012.

[27] Òscar Iglesias and Amílcar Labarta. Finite-size and surface effects in maghemite nanoparticles: Monte Carlo simulations. *Physical Review B*, 63(18):184416, 2001.

[28] L. Castelli, M. Fittipaldi, A. K. Powell, D. Gatteschi, and L. Sorace. Single crystal EPR study at 95 GHz of a large Fe based molecular nanomagnet: toward the structuring of magnetic nanoparticle properties. *Dalton transactions*, 40(32):8145–8155, 2011.

[29] An-Hui Lu, Wolfgang Schmidt, Nina Matoussevitch, Helmut Bönnemann, Bernd Spliethoff, Bernd Tesche, Eckhard Bill, Wolfgang Kiefer, and Ferai Schüth. Nanoengineering of a magnetically separable hydrogenation catalyst. *Angewandte Chemie - International Edition*, 43(33):4303–4306, 2004.

[30] Sophie Laurent, Delphine Forge, Marc Port, Alain Roch, Caroline Robic, Luce Vander Elst, and Robert N. Muller. Magnetic iron oxide nanoparticles: Synthesis, stabilization, vectorization, physicochemical characterizations and biological applications. *Chemical Reviews*, 108(6):2064–2110, 2008.

[31] Wilfried Andrä and Hannes Nowak, editors. *Magnetism in Medicine: A Handbook*. Wiley - VCH, Weinheim, Germany, 2007.

[32] S. Chikazumi, S. Taketomi, M. Ukita, M. Mizukami, H. Miyajima, M. Setogawa, and Y. Kurihara. Physics of magnetic fluids. *Journal of Magnetism and Magnetic Materials*, 65(2-3):245–251, 1987.

[33] Ajay Kumar Gupta and Mona Gupta. Synthesis and surface engineering of iron oxide nanoparticles for biomedical applications. *Biomaterials*, 26(18):3995–4021, 2005.

[34] Q. A. Pankhurst, J. Connolly, S. K. Jones, and J. Dobson. Applications of magnetic nanoparticles in biomedicine. *Journal of physics D: Applied Physics*, 36:R167–R181, 2003.

[35] Daniel W. Elliott and Wei-Xian Zhang. Field Assessment of Nanoscale Bimetallic Particles for Groundwater Treatment. *Environmental Science & Technology*, 35(24):4922–4926, 2001.

[36] Makoto Takafuji, Shunichi Ide, Hirotaka Ihara, and Zhenghe Xu. Preparation of Poly(1-vinylimidazole)-Grafted Magnetic Nanoparticles and Their Application for Removal of Metal Ions. *Chemistry of materials*, 16(4):1977–1983, 2004.

[37] R. Sessoli, D. Gatteschi, A. Caneschi, and M. A. Novak. Magnetic bistability in a metal-ion cluster. *Nature*, 365(6442):141–143, 1993.

[38] R. Sessoli, M. Mannini, F. Pineider, A. Cornia, and Ph. Sainctavit. XAS and XMCD of Single Molecule Magnets. In *Magnetism and Synchrotron Radiation*, pages 279–311. Springer, Berlin, Heidelberg, 2010.

[39] W. Wernsdorfer and R. Sessoli. Quantum Phase Interference and Parity Effects in Magnetic Molecular Clusters. *Science*, 284(5411):133–135, 1999.

[40] Arzhang Ardavan, Olivier Rival, John J L Morton, Stephen J. Blundell, Alexei M. Tyryshkin, Grigore A. Timco, and Richard E. P. Winpenny. Will spin-relaxation times in molecular magnets permit quantum information processing? *Physical Review Letters*, 98(5):057201, 2007.

[41] Lapo Bogani, Alessandro Vindigni, Roberta Sessoli, and Dante Gatteschi. Single chain magnets: where to from here? *Journal of Materials Chemistry*, 18(40):4750–4758, 2008.

[42] Dante Gatteschi and Alessandro Vindigni. Single-Chain Magnets. In *Molecular Magnets*, pages 191–220. Springer, Berlin, Heidelberg, 2014.

[43] Roy J. Glauber. Time-Dependent Statistics of the Ising Model. *Journal of Mathematical Physics*, 4(2):294–307, 1963.

[44] Andrea Caneschi, Dante Gatteschi, Nikolia Lalioti, Claudio Sangregorio, Roberta Sessoli, Giovanni Venturi, Alessandro Vindigni, Angelo Rettori, Maria G. Pini, and Miguel A. Novak. Cobalt (II)-Nitronyl Nitroxide Chains as Molecular Magnetic Nanowires. *Angewandte Chemie International Edition*, 113(9):1810–1813, 2001.

[45] Marco Scarrozza, Paolo Barone, Roberta Sessoli, and Silvia Picozzi. Magnetoelectric coupling and spin-induced electrical polarization in metal-organic magnetic chains. *Journal of Materials Chemistry C*, 4(19):4176–4185, 2016.

[46] Dávid Szaller, Sándor Bordács, and István Kézsmárki. Symmetry conditions for nonreciprocal light propagation in magnetic crystals. *Physical Review B*, 87(1):014421, 2013.

[47] Philipp Gütlich, Andreas Hauser, and Hartmut Spiering. Thermal and Optical Switching of Iron Complexes. *Angewandte Chemie International Edition*, 33:2024–2054, 1994.

[48] Philipp Gütlich, Yann Garcia, and Harold A. Goodwin. Spin crossover phenomena in Fe(II) complexes. *Chemical Society Reviews*, 29(6):419–427, 2000.

[49] Philipp Gütlich, Yann Garcia, and Theo Woike. Photoswitchable coordination compounds. *Coordination Chemistry Reviews*, 219-221:839–879, 2001.

[50] Andreas Hauser. Light-Induced Spin Crossover and the High-Spin Low-Spin Relaxation. In *Spin Crossover in Transition Metal Compounds II*, pages 155–198. Springer, Berlin, Heidelberg, 2004.

[51] Andreas Hauser, Cristian Enachescu, Max Lawson Daku, Alfredo Vargas, and Nahid Amstutz. Low-temperature lifetimes of metastable high-spin states in spin-crossover and in low-spin iron(II) compounds: The rule and exceptions to the rule. *Coordination Chemistry Reviews*, 250(13-14):1642–1652, 2006.

[52] Vadim Ksenofontov, Ana B. Gaspar, and Philipp Gütlich. Pressure Effect Studies on Spin Crossover and Valence Tautomeric Systems. In *Spin crossover in transition metal compounds III*, pages 23–64. Springer, Berlin, Heidelberg, 2004.

[53] A. Bousseksou, F. Varret, M. Goiran, K. Boukheddaden, and J. P. Tuchagues. The Spin Crossover Phenomenon Under High Magnetic Field. In *Spin Crossover in Transition Metal Compounds III*, pages 65–84. Springer, Berlin, Heidelberg, 2004.

[54] Philipp Gütlich and Harold A. Goodwin. Spin Crossover-An Overall Perspective. In *Spin Crossover in Transition Metal Compounds I*, pages 1–47. Springer, Berlin, Heidelberg, 2004.

[55] Andreas Hauser. Ligand Field Theoretical Considerations. In *Spin Crossover in Transition Metal Compounds I*, pages 49–58. Springer, Berlin, Heidelberg, 2004.

[56] Matthias Bernien, Holger Naggert, Lucas M Arruda, Lalminthang Kipgen, Fabian Nickel, Jorge Miguel, Christian F Hermanns, Alex Kru, Dennis Kru, Felix Tuczek, and Wolfgang Kuch. Highly Efficient Thermal and of an Fe (II) Complex in Direct Contact with a Solid Surface. *ACS Nano*, 9(9):8960–8966, 2015.

[57] José Antonio Real, Ana Belén Gaspar, and M. Carmen Muñoz. Thermal, pressure and light switchable spin-crossover materials. *Dalton Transactions*, 12:2062–2079, 2005.

[58] Sylvain Rat, Mirko Mikolasek, José Sánchez Costá, Aleksandr I. Chumakov, William Nicolazzi, Gábor Molnár, Lionel Salmon, and Azzedine Bousseksou. Raman and nuclear inelastic scattering study of the lattice dynamics of the [Fe(H2B(pz)2)2(phen)] spin crossover complex. *Chemical Physics Letters*, 653:131–136, 2016.

[59] S. Decurtins, P. Gütlich, C.P. Köhler, H. Spiering, and A. Hauser. Light-induced excited spin state trapping in a transition-metal complex: The hexa-1-propyltetrazole-iron (II) tetrafluoroborate spin-crossover system. *Chemical Physics Letters*, 105(1):1–4, 1984.

[60] S. Decurtins, P. Gutlich, K. M. Hasselbach, A. Hauser, and H. Spiering. Light-Induced Excited-Spin-State Trapping in Iron(II) Spin-Crossover Systems. Optical Spectroscopic and Magnetic Susceptibility Study. *Inorganic Chemistry*, 24(14):2174–2178, 1985.

[61] Philipp Gütlich, Ana B. Gaspar, and Yann Garcia. Spin state switching in iron coordination compounds. *Beilstein Journal of Organic Chemistry*, 9:342–391, 2013.

[62] Rudolf L. Mössbauer. Kernresonanzfluoreszenz von Gammastrahlung in Ir191. *Zeitschrift fur Physik*, 151(2):124–143, 1958.

[63] Rudolf L. Mössbauer. Kernresonanzabsorption von Gammastrahlung in Ir191. *Die Naturwissenschaften*, 45(22):538–539, 1958.

[64] Li-yong Chen and Yang De-ping. *Mössbauer Effect in Lattice Dynamics: Experimental Techniques and Applications*. Wiley-VCH Verlag, Weinheim, Germany, 2007.

[65] P.B. Moon and A. Storruste. Resonant nuclear scattering of 198Hg gamma-rays. *Proceedings of the Physical Society. Section A*, 66(7):585, 1953.

[66] Philipp Gutlich, Bill Eckhard, and Alfred X Trautwein. *Mössbauer Spectroscopy and Transition Metal Chemistry*. Springer-Verlag Berlin Heidelberg, 2011.

[67] Philipp Gütlich. Fifty Years of Mössbauer Spectroscopy in Solid State Research - Remarkable Achievements, Future Perspectives. *Zeitschrift für anorganische und allgemeine Chemie*, 638(1):15–43, 2012.

[68] R. Dean Taylor and Paul P. Craig. Correlation between Mössbauer Resonance Strength and Second-Order Doppler Shift: Estimate of Zero-Point Velocity. *Physical Review*, 175(3):782–787, 1968.

[69] Rudolf Rüffer and Aleksandr I. Chumakov. Nuclear Resonance Beamline at ESRF. *Hyperfine Interactions*, 97(1):589–604, 1996.

[70] Vasily Potapkin, Aleksandr I. Chumakov, Gennadii V. Smirnov, Jean Philippe Celse, Rudolf Rüffer, Catherine McCammon, and Leonid Dubrovinsky. The 57Fe Synchrotron Mössbauer Source at the ESRF. *Journal of Synchrotron Radiation*, 19(4):559–569, 2012.

[71] G. V. Smirnov, U. van Bürck, A. I. Chumakov, A. Q. R. Baron, and R. Rüffer. Synchrotron Mössbauer source. *Physical Review B*, 55(9):5811–5815, 1997.

[72] John A. Weil and James R. Bolton. *Electron paramagnetic resonance: elementary theory and practical applications.* John Wiley & Sons, 2007.

[73] Carlo Corvaja. Introduction to Electron Paramagnetic Resonance. In *Electron Paramagnetic Resonance: A Practitioners Toolkit*, pages 1–36. John Wiley & Sons, 2009.

[74] A. Bencini and D. Gatteschi. Electron Paramagnetic Resonance Spectroscopy. In *Inorganic Electronic Structure and Spectroscopy, Volume I: Methodology*, page 93. John Wiley & Sons, 1999.

[75] Alessandro Bencini and Dante Gatteschi. *Electron Paramagnetic Resonance of Exchange Coupled Systems.* Springer-Verlag Berlin Heidelberg, 1990.

[76] Oliver Waldmann. A criterion for the anisotropy barrier in single-molecule magnets. *Inorganic Chemistry*, 46(24):10035–10037, 2007.

[77] Maria Fittipaldi, Dante Gatteschi, and Paolo Fornasiero. The power of EPR techniques in revealing active sites in heterogeneous photocatalysis: The case of anion doped TiO2. *Catalysis Today*, 206:2–11, 2013.

[78] G. R. Eaton and S. S. Eaton. High-field and high-frequency EPR. *Applied Magnetic Resonance*, 16(2):161–166, 1999.

[79] A. L. Barra, L. C. Brunel, D Gatteschi, L. Pardi, and R. Sessoli. High-Frequency EPR Spectroscopy of Large Metal Ion Clusters: From Zero Field Splitting to Quantum Tunneling of the Magnetization. *Accounts of chemical research*, 31(8):460–466, 1998.

[80] A. L. Barra. High-frequency EPR spectroscopy of single-molecule magnets: a case study. *Applied Magnetic Resonance*, 21(3-4):619–628, 2001.

[81] A.L. Barra, L.C. Brunel, and J.B. Robert. EPR spectroscopy at very high field. *Chemical Physics Letters*, 165(1):107–109, 1990.

[82] Andrea Caneschi, Dante Gatteschi, Roberta Sessoli, Anne Laure Barra, Louis Claude Brunei, and Maurice Guillot. Alternating Current Susceptibility, High Field Magnetization, and Millimeter Band EPR Evidence for a Ground S=10 State in [Mn12O12(CH3COO)16(H2O)4].2CH3COOH.4H2O. *Journal of the American Chemical Society*, 113(15):5873–5874, 1991.

[83] Anne Laure Barra, Dante Gatteschi, and Roberta Sessoli. High-frequency EPR spectra of a molecular nanomagnet: Understanding quantum tunneling of the magnetization. *Physical Review B*, 56(13):8192–8198, 1997.

[84] A. Schweiger and G. Jeschke. *Principles of pulse electron paramagnetic resonance.* Oxford University Press, 2001.

[85] C. Schlegel, J. Van Slageren, M. Manoli, E. K. Brechin, and M. Dressel. Direct observation of quantum coherence in single-molecule magnets. *Physical Review Letters*, 101(14):147203, 2008.

[86] Susumu Takahashi, Johan van Tol, Christopher C. Beedle, David N. Hendrickson, Louis-Claude Brunel, and Mark S. Sherwin. Coherent Manipulation and Decoherence of S = 10 Single-Molecule Magnets. *Physical Review Letters*, 102(8):087603, 2009.

[87] W. B. Mims. *The linear electric field effect in paramagnetic resonance*. Clarendon Press, 1976.

[88] N. Bloembergen. Linear Stark Effect in Magnetic Resonance Spectra. *Science*, 133:1363, 1961.

[89] E. B. Royce and N. Bloembergen. Linear Electric Shifts in the Paramagnetic Resonance of Al2O3: Cr and MgO: Cr. *Physical Review*, 131(5):1912–1923, 1963.

[90] G W Ludwig and H H Woodbury. Splitting of electron spin resonance lines by an applied electric field. *Physical Review Letters*, 7(6):240, 1961.

[91] W. B. Mims. Measurement of the linear electric field effect in EPR using the spin echo method. *Review of Scientific Instruments*, 45(12):1583–1591, 1974.

[92] R. P. J. Merks, P. van der Heide, and R. de Beer. Linear electric field effect on the EPR spectrum of single crystals and powdered single crystals of Cs2ZnCl4:Cu2+. *Journal of Physics C: Solid State Physics*, 12(15):3097–3104, 1979.

[93] W. B. Mims. Electric Field Effects in Spin Echoes. *Physical Review*, 133(3A):A835, 1964.

[94] Richard E. George, James P. Edwards, and Arzhang Ardavan. Coherent spin control by electrical manipulation of the magnetic anisotropy. *Physical Review Letters*, 110(2):027601, 2013.

[95] Junjie Liu, Jakub Mrozek, William K. Myers, Grigore A. Timco, Richard E. P. Winpenny, Benjamin Kintzel, Winfried Plass, and Arzhang Ardavan. Electric field control of spins in molecular magnets (2018). Preprint available at arXiv:1805.05256.

[96] Mircea Trif, Filippo Troiani, Dimitrije Stepanenko, and Daniel Loss. Spin-electric coupling in molecular magnets. *Physical Review Letters*, 101(21):217201, 2008.

[97] P. Wysling and K. A. Muller. Electric-field-modulated resonance lines of non-Kramers ions. *Journal of Physics C: Solid State Physics*, 9(4):635–645, 1975.

[98] A. Maisuradze, A. Shengelaya, H. Berger, D. M. Djoki, and H. Keller. Magnetoelectric coupling in single crystal Cu2OSeO3 studied by a novel electron spin resonance technique. *Physical Review Letters*, 108(24):247211, 2012.

[99] Andrea Cornia and Matteo Mannini. Single-Molecule Magnets on Surfaces. In *Molecular Nanomagnets and Related Phenomena*, pages 293–330. Springer, Berlin, Heidelberg, 2014.

[100] J. Dreiser. Molecular lanthanide single-ion magnets: from bulk to submonolayers. *Journal of Physics: Condensed matter*, 27(18):183203, 2015.

[101] Rebecca J. Holmberg and Muralee Murugesu. Adhering magnetic molecules to surfaces. *Journal of Materials Chemistry C*, 3:11986–11998, 2015.

[102] Matteo Mannini, Francesco Pineider, Philippe Sainctavit, Chiara Danieli, Edwige Otero, Corrado Sciancalepore, Anna Maria Talarico, Marie-anne Arrio, Andrea Cornia, Dante Gatteschi, and Roberta Sessoli. Magnetic memory of a single-molecule quantum magnet wired to a gold surface. *Nature Materials*, 8(3):194–197, 2009.

[103] Matteo Mannini, Federico Bertani, Cristina Tudisco, Luigi Malavolti, Lorenzo Poggini, Kasjan Misztal, Daniela Menozzi, Alessandro Motta, Edwige Otero, Philippe Ohresser, Philippe Sainctavit, Guglielmo G. Condorelli, Enrico Dalcanale, and Roberta Sessoli. Magnetic behaviour of TbPc2 single-molecule magnets chemically grafted on silicon surface. *Nature Communications*, 5(1):4582, 2014.

[104] Christian Wäckerlin, Fabio Donati, Aparajita Singha, Romana Baltic, Stefano Rusponi, Katharina Diller, François Patthey, Marina Pivetta, Yanhua Lan, Svetlana Klyatskaya, Mario Ruben, Harald Brune, and Jan Dreiser. Giant Hysteresis of Single-Molecule Magnets Adsorbed on a Nonmagnetic Insulator. *Advanced Materials*, 28(26):5195–5199, 2016.

[105] Fabian D. Natterer, Kai Yang, William Paul, Philip Willke, Taeyoung Choi, Thomas Greber, Andreas J Heinrich, and Christopher P Lutz. Reading and writing single-atom magnets. *Nature*, 543(7644):226–228, 2017.

[106] Gerrit van der Laan and Adriana I. Figueroa. X-ray magnetic circular dichroism-A versatile tool to study magnetism. *Coordination Chemistry Reviews*, 277:95–129, 2014.

[107] Andrea Caneschi, Dante Gatteschi, and Federico Totti. Molecular magnets and surfaces: A promising marriage. A DFT insight. *Coordination Chemistry Reviews*, 289:357–378, 2015.

[108] A. Caneschi, L. Cianchi, F. Del Giallo, D. Gatteschi, P. Moretti, F. Pieralli, and G. Spina. Study of the spin dynamics in an iron cluster nanomagnet by means

of Mossbauer spectroscopy. *Journal of Physics: Condensed Matter*, 11(16):3395–3403, 1999.

[109] L. Cianchi, F. Del Giallo, G. Spina, W. Reiff, and A. Caneschi. Spin dynamics study of magnetic molecular clusters by means of Mossbauer spectroscopy. *Physical Review B*, 65(6):064415, 2002.

[110] R. Röhlsberger, J. Bansmann, V. Senz, K. L. Jonas, A. Bettac, K. H. Meiwes-Broer, and O. Leupold. Nanoscale magnetism probed by nuclear resonant scattering of synchrotron radiation. *Physical Review B*, 67(24):245412, 2003.

[111] R. Röhlsberger, T. Klein, K. Schlage, O. Leupold, and R. Rüffer. Coherent x-ray scattering from ultrathin probe layers. *Physical Review B*, 69(23):235412, 2004.

[112] M. Slezak, T. Slezak, K. Freindl, W. Karas, N. Spiridis, M. Zajaac, A. I. Chumakov, S. Stankov, R. Rüffer, and J. Korecki. Perpendicular magnetic anisotropy and noncollinear magnetic structure in ultrathin Fe films on W(110). *Physical Review B*, 87(13):134411, 2013.

[113] Alessandro Lunghi, Marcella Iannuzzi, Roberta Sessoli, and Federico Totti. Single molecule magnets grafted on gold: magnetic properties from ab initio molecular dynamics. *Journal of Materials Chemistry C*, 3(28):7294–7304, 2015.

[114] Luigi Malavolti, Valeria Lanzilotto, Silviya Ninova, Lorenzo Poggini, Irene Cimatti, Brunetto Cortigiani, Ludovica Margheriti, Daniele Chiappe, Edwige Otero, Philippe Sainctavit, Federico Totti, Andrea Cornia, Matteo Mannini, and Roberta Sessoli. Magnetic Bistability in a Submonolayer of Sublimated Fe 4 Single-Molecule Magnets. *Nano Letters*, 15(1):535–541, 2015.

[115] Alexander S. Zyazin, Johan W. G. Van Den Berg, Edgar A. Osorio, Herre S. J. Van Der Zant, Nikolaos P. Konstantinidis, Martin Leijnse, Maarten R. Wegewijs, Falk May, Walter Hofstetter, Chiara Danieli, and Andrea Cornia. Electric field controlled magnetic anisotropy in a single molecule. *Nano Letters*, 10(9):3307–3311, 2010.

[116] M. Mannini, F. Pineider, C. Danieli, F. Totti, L. Sorace, Ph. Sainctavit, M.-A. Arrio, E. Otero, L. Joly, J. C. Cezar, A. Cornia, and R. Sessoli. Quantum tunnelling of the magnetization in a monolayer of oriented single-molecule magnets. *Nature*, 468(7322):417–421, 2010.

[117] Pasquale Totaro, Lorenzo Poggini, Annaick Favre, Matteo Mannini, Philippe Sainctavit, Andrea Cornia, Agnese Magnani, and Roberta Sessoli. Tetrairon(III) single-molecule magnet monolayers on gold: Insights from ToF-SIMS and isotopic labeling. *Langmuir*, 30(29):8645–8649, 2014.

[118] A. L. Barra, A. Caneschi, A. Cornia, F. De Fabrizi Biani, D. Gatteschi, C. Sangregorio, R. Sessoli, and L. Sorace. Single-molecule magnet behavior of a tetranuclear

iron(III) complex. The origin of slow magnetic relaxation in iron(III) clusters. *Journal of the American Chemical Society*, 121(22):5302–5310, 1999.

[119] N. N. Greenwood and T. C. Gibb. *Mössbauer Spectroscopy*. Springer, 1971.

[120] L. Cianchi, P. Moretti, M. Mancini, and G. Spina. Mossbauer spectra in paramagnetic relaxing systems. *Reports on Progress in Physics*, 49(11):1243–1291, 1986.

[121] Jacob A.J. Burgess, Luigi Malavolti, Valeria Lanzilotto, Matteo Mannini, Shichao Yan, Silviya Ninova, Federico Totti, Steffen Rolf-Pissarczyk, Andrea Cornia, Roberta Sessoli, and Sebastian Loth. Magnetic fingerprint of individual Fe4 molecular magnets under compression by a scanning tunnelling microscope. *Nature Communications*, 6(1):8216, 2015.

[122] Mirko Cinchetti, V. Alek Dediu, and Luis E. Hueso. Activating the molecular spinterface. *Nature Materials*, 16(5):507–515, 2017.

[123] Nicolás Moliner, Lionel Salmon, Laurence Capes, M. Carmen Muñoz, Jean-François Létard, Azzedine Bousseksou, Jean-pierre Tuchagues, John J. McGarvey, Andrew C. Dennis, Miguel Castro, Ramón Burriel, and José Antonio Real. Thermal and Optical Switching of Molecular Spin States in the {[FeL[H2B(pz)2]2} Spin-Crossover System (L = bpy, phen). *The Journal of Physical Chemistry B*, 106(16):4276–4283, 2002.

[124] Ben Warner, Jenny C. Oberg, Tobias G. Gill, Fadi El Hallak, Cyrus F. Hirjibehedin, Michele Serri, Sandrine Heutz, Marie Anne Arrio, Philippe Sainctavit, Matteo Mannini, Giordano Poneti, Roberta Sessoli, and Patrick Rosa. Temperature- and light-induced spin crossover observed by X-ray spectroscopy on isolated Fe(II) complexes on gold. *Journal of Physical Chemistry Letters*, 4(9):1546–1552, 2013.

[125] Amber L. Thompson, Andrés E. Goeta, José A. Real, Ana Galet, and M. Carmen Muñoz. Thermal and light induced polymorphism in iron(II) spin crossover compounds. *Chemical Communications*, 12:1390–1391, 2004.

[126] A. I. Popov, D. I. Plokhov, and A. K. Zvezdin. Anapole moment and spin-electric interactions in rare-earth nanoclusters. *EPL (Europhysics Letters)*, 87(6):67004, 2009.

[127] Nicola A. Spaldin and Manfred Fiebig. Materials science. The renaissance of magnetoelectric multiferroics. *Science*, 309(5733):391–392, 2005.

[128] Daniel Khomskii. Classifying multiferroics: Mechanisms and effects. *Physics*, 2:20, 2009.

[129] Manfred Fiebig, Thomas Lottermoser, Dennis Meier, and Morgan Trassin. The evolution of multiferroics. *Nature Reviews Materials*, 1(8):16046, 2016.

[130] W. Eerenstein, N. D. Mathur, and J. F. Scott. Multiferroic and magnetoelectric materials. *Nature*, 442(7104):759–765, 2006.

[131] Yoshinori Tokura, Masashi Kawasaki, and Naoto Nagaosa. Emergent functions of quantum materials. *Nature Physics*, 13(11):1056–1068, 2017.

[132] Michael A. Nielsen and Isaac L. Chuang. *Quantum computation and quantum information*. Cambridge University Press, 2000.

[133] Andrea Caneschi, Dante Gatteschi, Paul Rey, and R. Sessoli. Structure and magnetic ordering of a ferrimagnetic helix formed by manganese(II) and a nitronyl nitroxide radical. *Inorganic chemistry*, 30(20):3936–3941, 1991.

[134] M. Drillon, E. Coronado, D. Beltran, and R. Georges. Classical treatment of a heisenberg linear chain with spin alternation; application to the MnNi(EDTA)-6H2O complex. *Chemical Physics*, 79(3):449–453, 1983.

[135] Kazukiyo Nagata and Tazuke Yuichi. Short Range Order Effects on EPR Frequencies in Heisenberg Linear Chain Antiferromagnets. *Journal of the Physical Society of Japan*, 32(2):337–345, 1972.

[136] Takashi Karasudani and Hisao Okamoto. Temperature Dependence of EPR Frequencies in Pure-and Pseudo-One Dimensional Heisenberg Magnets. *Journal of the Physical Society of Japan*, 43(4):1131–1136, 1977.

[137] G. Annino, J. A. Villanueva-Garibay, P. J.M. van Bentum, A. A.K. Klaassen, and A. P.M. Kentgens. A high-conversion-factor, double-resonance structure for high-field dynamic nuclear polarization. *Applied Magnetic Resonance*, 37(1):851–864, 2010.

[138] J. A. Villanueva-Garibay, G. Annino, P. J. M. van Bentum, and A. P. M. Kentgens. Pushing the limit of liquid-state dynamic nuclear polarization at high field. *Physical Chemistry Chemical Physics*, 12(22):5846–5849, 2010.

[139] Stefan Stoll and Arthur Schweiger. EasySpin, a comprehensive software package for spectral simulation and analysis in EPR. *Journal of Magnetic Resonance*, 178(1):42–55, 2006.

[140] Charles P. Poole. *Electron spin resonance: a comprehensive treatise on experimental techniques*. John Wiley & Sons, 1983.

[141] Yûichi Tazuke and Kazukiyo Nagata. EPR Line-Widths of a One-Dimensional Heisenberg Antiferromagnet CsMnCl32H2O. *Journal of the Physical Society of Japan*, 38(4):1003–1010, 1975.

[142] K. F. Thompson, C. Gokler, S. Lloyd, and P. W. Shor. Time independent universal computing with spin chains: quantum plinko machine. *New Journal of Physics*, 18(7):073044, 2016.

[143] Dmitry I. Bazhanov, Ilia N. Sivkov, and Valeri S. Stepanyuk. Engineering of entanglement and spin state transfer via quantum chains of atomic spins at large separations. *Scientific Reports*, 8(1):14118, 2018.

[144] Anqin Xu, John N. Harb, Mauri A. Kostiainen, William L. Hughes, Adam T. Woolley, Haitao Liu, and Ashwin Gopinath. DNA origami: The bridge from bottom to top. *MRS Bulletin*, 42(12):943–950, 2017.

[145] Lorena E. Rosaleny, Salvador Cardona-Serra, Luis Escalera-Moreno, José J. Baldoví, Violetta Golebiewska, Karolina Wlazło, Patricia Casino, Helena Prima-García, Alejandro Gaita-Ariño, and Eugenio Coronado. Peptides as Versatile Platforms for Quantum Computing. *The Journal of Physical Chemistry Letters*, 9(16):4522–4526, 2018.

[146] Anna-Laure Barra, Louis-Claude Brunel, Dante Gatteschi, Luca Pardi, and Roberta Sessoli. High-Frequency EPR Spectroscopy of Large Metal Ion Clusters: From Zero Field Splitting to Quantum Tunneling of the Magnetization. *Accounts of chemical research*, 31(8):460–466, 1998.

[147] Dante Gatteschi, Anne Laure Barra, Andrea Caneschi, Andrea Cornia, Roberta Sessoli, and Lorenzo Sorace. EPR of molecular nanomagnets. *Coordination Chemistry Reviews*, 250(11):1514–1529, 2006.

[148] Eric J. L. McInnes. Spectroscopy of Single-molecule Magnets. In *Single-Molecule Magnets and Related Phenomena*, pages 69–102. Springer, Berlin, Heidelberg, 2006.

[149] R. S. Edwards, S. Maccagnano, E. C. Yang, S. Hill, W. Wernsdorfer, D. Hendrickson, and G. Christou. High-frequency electron paramagnetic resonance investigations of tetranuclear nickel-based single-molecule magnets. *Journal of Applied Physics*, 93(10):7807–7809, 2003.

[150] S. Hill, S. Maccagnano, K. Park, R. M. Achey, J. M. North, and N. S. Dalal. Detailed single-crystal EPR line shape measurements for the single-molecule magnets Fe8Br and Mn-12-acetate. *Physical Review B*, 65(22):224410, 2002.

[151] F. Moro, R. De Miguel, M. Jenkins, C. Gomez-Moreno, D. Sells, F. Tuna, E. J. L. McInnes, A. Lostao, F. Luis, and J. Van Slageren. Magnetic anisotropy of polycrystalline magnetoferritin investigated by SQUID and electron magnetic resonance. *Journal of Magnetism and Magnetic Materials*, 361:188–196, 2014.

[152] Alex Pronschinske, Yifeng Chen, Geoffrey F. Lewis, David A. Shultz, Arrigo Calzolari, Marco Buongiorno Nardelli, and Daniel B. Dougherty. Modification of molecular spin crossover in ultrathin films. *Nano Letters*, 13(4):1429–1434, 2013.

[153] Thiruvancheril G. Gopakumar, Matthias Bernien, Holger Naggert, Francesca Matino, Christian F. Hermanns, Alexander Bannwarth, Svenja Mühlenberend, Alex Krüger, Dennis Krüger, Fabian Nickel, Waldemar Walter, Richard Berndt, Wolfgang Kuch, and Felix Tuczek. Spin-crossover complex on Au(111): Structural and electronic differences between mono- and multilayers. *Chemistry - A European Journal*, 19(46):15702–15709, 2013.

[154] Kaushik Bairagi, Olga Iasco, Amandine Bellec, Alexey Kartsev, Dongzhe Li, Jerome Lagoute, Cyril Chacon, Yann Girard, Sylvie Rousset, Frederic Miserque, Yannick J. Dappe, Alexander Smogunov, Cyrille Barreteau, Marie Laure Boillot, Talal Mallah, and Vincent Repain. Molecular-scale dynamics of light-induced spin cross-over in a two-dimensional layer. *Nature Communications*, 7:12212, 2016.

[155] Kaushik Bairagi, Amandine Bellec, Cynthia Fourmental, Olga Iasco, Jérôme Lagoute, Cyril Chacon, Yann Girard, Sylvie Rousset, Fadi Choueikani, Edwige Otero, Philippe Ohresser, Philippe Sainctavit, Marie-Laure Boillot, Talal Mallah, and Vincent Repain. Temperature-, Light-, and Soft X-ray-Induced Spin Crossover in a Single Layer of FeII-Pyrazolylborate Molecules in Direct Contact with Gold. *The Journal of Physical Chemistry C*, 122(1):727–731, 2018.

[156] Matthias Bernien, Dennis Wiedemann, Christian F. Hermanns, Alex Krüger, Daniela Rolf, Wolfgang Kroener, Paul Müller, Andreas Grohmann, and Wolfgang Kuch. Spin crossover in a vacuum-deposited submonolayer of a molecular iron(II) complex. *Journal of Physical Chemistry Letters*, 3(23):3431–3434, 2012.

[157] Sascha Ossinger, Holger Naggert, Lalminthang Kipgen, Torben Jasper-Toennies, Abhishek Rai, Julian Rudnik, Fabian Nickel, Lucas M. Arruda, Matthias Bernien, Wolfgang Kuch, Richard Berndt, and Felix Tuczek. Vacuum-Evaporable Spin-Crossover Complexes in Direct Contact with a Solid Surface: Bismuth versus Gold. *Journal of Physical Chemistry C*, 121(2):1210–1219, 2017.

[158] V. Davesne, M. Gruber, M. Studniarek, W. H. Doh, S. Zafeiratos, L. Joly, F. Sirotti, M. G. Silly, A. B. Gaspar, J. A. Real, G. Schmerber, M. Bowen, W. Weber, S. Boukari, V. Da Costa, J. Arabski, W. Wulfhekel, and E. Beaurepaire. Hysteresis and change of transition temperature in thin films of Fe{[Me2Pyrz]3BH}2, a new sublimable spin-crossover molecule. *Journal of Chemical Physics*, 142(19):194702, 2015.

[159] Toshio Miyamachi, Manuel Gruber, Vincent Davesne, Martin Bowen, Samy Boukari, Loic Joly, Fabrice Scheurer, Guillaume Rogez, Toyo Kazu Yamada, Philippe Ohresser, Eric Beaurepaire, and Wulf Wulfhekel. Robust spin crossover and memristance across a single molecule. *Nature Communications*, 3:938, 2012.

[160] Manuel Gruber, Toshio Miyamachi, Vincent Davesne, Martin Bowen, Samy Boukari, Wulf Wulfhekel, Mebarek Alouani, and Eric Beaurepaire. Spin crossover in Fe(phen)2(NCS)2 complexes on metallic surfaces. *The Journal of Chemical Physics*, 146(9):092312, 2017.

[161] H. Naggert, J. Rudnik, L. Kipgen, M. Bernien, F. Nickel, L. M. Arruda, W. Kuch, C. Näther, and F. Tuczek. Vacuum-evaporable spin-crossover complexes: physicochemical properties in the crystalline bulk and in thin films deposited from the gas phase. *Journal of Materials Chemistry C*, 3(30):7870–7877, 2015.

Acknowledgements

This PhD thesis is the result of a three year course, during which I met different techniques and various nanomaterials. Each reported study has been a team work, where every person participated with its knowledge.

First, I would like to thank Dr. Maria Fittipaldi and Prof. Gabriele Spina, who introduced me to EPR and Mössbauer spectroscopy. They have always shown accuracy in their teachings and great availability and comprehension to my questions.

I thank people of LaMM (Laboratory of Molecular Magnetism), who collaborated to many realized studies: everytime I found a professional and friendly atmosphere.

I thank Annamaria, Stefano and Davide, colleagues in the office at the Department of Physics, who were present to share words and advices.

I thank Demetrio for the interesting conversations that we had everyday.

I thank Barbara for her support and being next to me.